UNIVERSITY OF SOUTHAMPTON

FACULTY OF NATURAL AND ENVIRONMENTAL SCIENCES

OCEAN AND EARTH SCIENCE

Impact of Seabed Properties on the Ampacity and Reliability of Submarine HV Cables

By

Chinedu John Emeana

A thesis submitted for the degree of

Doctor of Philosophy

October 2016

University of Southampton

ABSTRACT

FACULTY OF NATURAL AND ENVIRONMENTAL SCIENCES

OCEAN AND EARTH SCIENCE

Thesis for the degree of Doctor of Philosophy

IMPACT OF SEABED PROPERTIES ON THE AMPACITY AND RELIABILITY OF SUBMARINE HV CABLES

by

Chinedu John Emeana

The expansion of offshore renewable energy infrastructure and the need for trans-continental shelf power transmission require the use of submarine High Voltage (HV) cables. These cables have maximum operating surface temperatures of up to 90^{o}C and are typically buried 1-2 m beneath the seabed, within the wide range of substrates found on the continental shelf. However, the heat flow pattern and potential effects on the sedimentary environments around such anomalously high heat sources in the near surface sediments are poorly understood.

Temperature measurements from a 2D laboratory experiment representing a buried submarine HV cable are presented, and the thermal regimes generated within a range of typical unconsolidated shelf sediments—coarse silt, fine sand and very coarse sand are identified. Several experiments were carried out in a large (2 x 2.5 m) tank filled with water-saturated artificial (ballotini - spherical glass beads) and natural sediments (fine marine sand) with a buried heat source and 120 thermocouples to measure the time-dependent 2D temperature distributions. The observed steady state heat flow regimes and normalised radial temperature distributions were compared with outputs from corresponding Finite Element Method (FEM) simulations. The results show that the mechanisms of heat transfer and thus temperature fields generated from submarine HV cables buried within a range of sediments are highly variable.

Coarse silts with ~10^{-13} m^2 permeability, are shown to be purely conductive with 10 - 60 ^{o}C radial temperature distribution within 40 cm from a 60 °C above ambient source. Fine sands with ~10^{-11} m^2 permeability, demonstrate a transition from conductive to convective heat transfer at c. 20°C above ambient with 10 – 55 ^{o}C asymmetric temperature rise up to 1 m above a 55^{o}C above ambient heat source. Very coarse sands with ~10^{-9} m^2 permeability, exhibit dominantly convective heat transfer even at very low (c. 7^{o}C) operating heat source temperatures and with 10 - 18 ^{o}C significant asymmetric temperature rise of the surrounding sediments over 1 m above an 18 ^{o}C heat source. The computed controlling thermal properties demonstrate a distinct variation of thermal diffusivity and conductivity within different sediment types; sandy (fine sands) sediments are about twice more effective at diffusing heat than muddy (coarse silts) sediments.

The occurrence of convection heat transfer within high permeability sediments is an important insight that are currently neglected in the existing IEC 60287 standard for current ratings estimation. Significant convection supports more efficient heat transfer leading to reduced cable temperature, increased current ratings and ampacity, decreased degradation rates of cable insulation and thus increased life span and decrease manufacturing costs of submarine cables. Also the varying sediment thermal conductivity around submarine HV cables further implies that cables buried around sandy sediments will uptake heat more rapidly than in muddy sediments, which are also not considered in the existing IEC 60287 standards. In addition, these findings are important for the surrounding near surface environments experiencing such high temperatures and may have significant implications for chemical and physical processes operating at the grain and sub-grain scale as well as biological activity at both micro-faunal and macro-faunal levels.

Table of Contents

List of Tables

List of Figures

DECLARATION OF AUTHORSHIP

I, **Chinedu John Emeana**, declare that this thesis and the work presented in it are my own and has been generated by me as the result of my own original research.

Impact of Seabed Properties on the Ampacity and Reliability of Submarine HV Cables

I confirm that:

1. This work was done wholly or mainly while in candidature for a research degree at this University;
2. Where any part of this thesis has previously been submitted for a degree or any other qualification at this University or any other institution, this has been clearly stated;
3. Where I have consulted the published work of others, this is always clearly attributed;
4. Where I have quoted from the work of others, the source is always given. With the exception of such quotations, this thesis is entirely my own work;
5. I have acknowledged all main sources of help;
6. Where the thesis is based on work done by myself jointly with others, I have made clear exactly what was done by others and what I have contributed myself;
7. Either none of this work has been published before submission, or parts of this work have been published as:

   The thermal regime around buried submarine high voltage cables, C.J. Emeana, T.J. Hughes, J.K. Dix, T.M. Gernon, T.J. Henstock, C.E.L.

Thompson, and J.A. Pilgrim, Geophysical Journal International (GJI), 2016, Vol.: 206 (2), Pages: 1051-1064, doi:10.1093/gji/ggw195. Author list are reflective of relative contributions. Particularly, the Finite Element Method (FEM) model figures of the steady state heat flow regimes and corresponding figures presented in the GJI article as well as in chapter 3 were carried out by T.J. Hughes. The FEM figures were added to the GJI article following reviewer's comments requesting the addition of numerical models to support the physical modelling results carried out by C.J. Emeana.

Signed:..

Date: ....

Acknowledgements

I would like to recognize all those who have supported me, in one way or the other throughout the course of my PhD. First and foremost, I would like to acknowledge and say a very BIG THANK YOU to my 5 supervisors: Justin Dix, Tim Henstock, Charlie Thompson, Tom Gernon and James Pilgrim; for your wonderful advice and encouragement at all times, even during the weekends and my customary late-night/very early morning emails. I wish to thank Lisa McNeill, my PhD panel chair for all her support and encouragement. Also thanks to my financial sponsors: National Grid UK Limited, Engineering Physical Sciences Research Council (EPSRC), UK and University of Southampton, UK; for providing me with a full scholarship covering my tuition fees, stipends and other expenses throughout the PhD research.

I wish to appreciate particularly the following mechanical and electrical technicians: Kelvin Aylett, Neil Jenkinson, Graham Blythe, for their assistance in the construction of the pseudo HV cable heat source and HV (small and large) tank electrical wiring and testing. I appreciate the support I received from John Davies and Kate Davies. would also like to thank my fellow PhD students: Tim Hughes, Saikiran Tharimena, Matjet, Jesepe and Michael Faggetter, for all our technical brainstorming and stress bursting chats. Extra thanks must go to Tim Hughes, whose script writing assistance has been helpful.

Finally I wish to heavily thank and acknowledge my exceptional, lovely and understanding wife (Mrs Kelechi Laura Emeana) for her massive and undoubted

support throughout the good times, and the not-so-good times, as well as encouraging me to finally finish writing this thesis and for putting up with me (all my troubles!) over the course of my PhD studies. Also to my lovely ‘little’ boys (Excel Emeana and Wisdom Emeana), that have grown into ‘big’ boys through the course of my PhD studies, thanks for making me feel happy during our plays and running around at home. It was really a source of stress relief and I enjoyed every bit of it. And many thanks to my ever active mother (Mrs Agatha Emeana), your support is truly divine as it has continued strongly throughout my life. I wish to also appreciate my wonderful late father (Innocent Emeana), who gave me the ‘strong building blocks’. Finally and not the least, many thanks to my brothers: Onyii, Williams, Chike and my sisters: Akunna, Ogechi and Kelechi. I love you all.

1

Introduction

1.1 Introduction

Submarine High Voltage (HV) cables form the backbone of offshore renewable power transmission, and are increasingly important in regional energy distribution over distances of up to 580 km across continental shelves, for example the NorNed HV direct current submarine power cable link (Worzyk, 2009). The commercial interest in sub-seafloor HV cables has grown significantly in recent years, particularly as a result of more (and larger) wind farms (Figure 1.1) located ever further offshore (EWEA, 2013) and the simultaneous development of trans-national marine cables links such as the Cross Sound HV direct current submarine cable link (Railing *et al.*, 2004) and proposed European Super Grid (UK House of Commons: Energy and Climate Change Committee, 2011). These multi-million pound submarine HV cable links (Figure 1.2) are typically buried by trenching to depths of 1-2 m (Mole *et al.*, 1997, Worzyk, 2009) beneath the seabed and within the wide range of substrates found on the continental shelf, with little knowledge of the thermal regime they will enter or generate during operation.

Sheringham Shoal Offshore Wind Farm, UK,
http://www.scira.co.uk/

Figure 1.1: Sheringham Shoal Offshore Wind Farm, England. It is one of the UK renewable energy resource initiatives for offshore wind farm electricity generation.

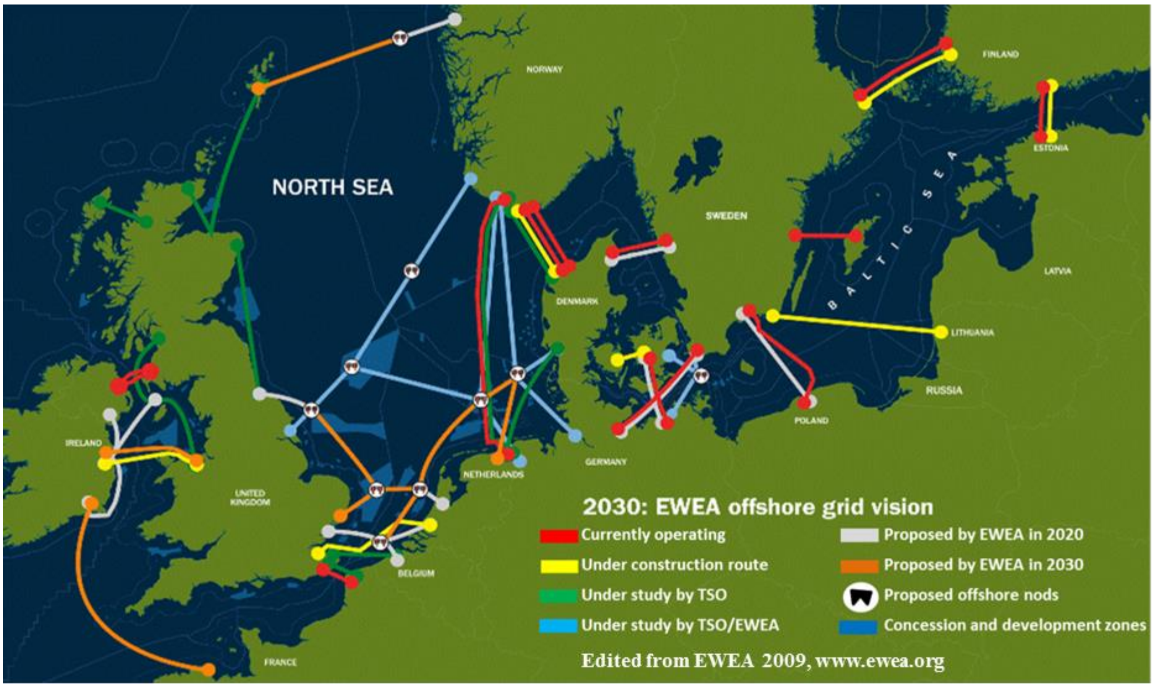

Edited from EWEA 2009, www.ewea.org

Figure 1.2: “European Mega Grid” a 2030 offshore grid vision of the European Wind Energy Association (EWEA, 2013).

1.2 HV Cable Design and Heat Losses

High voltage is defined as any voltage over 1000 volts. However HV cables used for electricity transmission below 3kV are classified as ‘low’ HV cables, 3 to 33kV classified as ‘medium’ HV cables, 33 to 132kV classified as ‘high’ HV cables and above 132kV as ‘extra’ HV cables (Kuffel and Zaengl, 2004). The design of an HV cable is mainly constrained by the technical requirements and planned power of the electricity transmission of the particular cable route. The typical components (Figure 1.3) are: a conductor at the centre, semi-conducting screen, insulation material, insulation screen, outer conductor or metallic sheath, over-sheath, stranded steel armouring and outer serving.

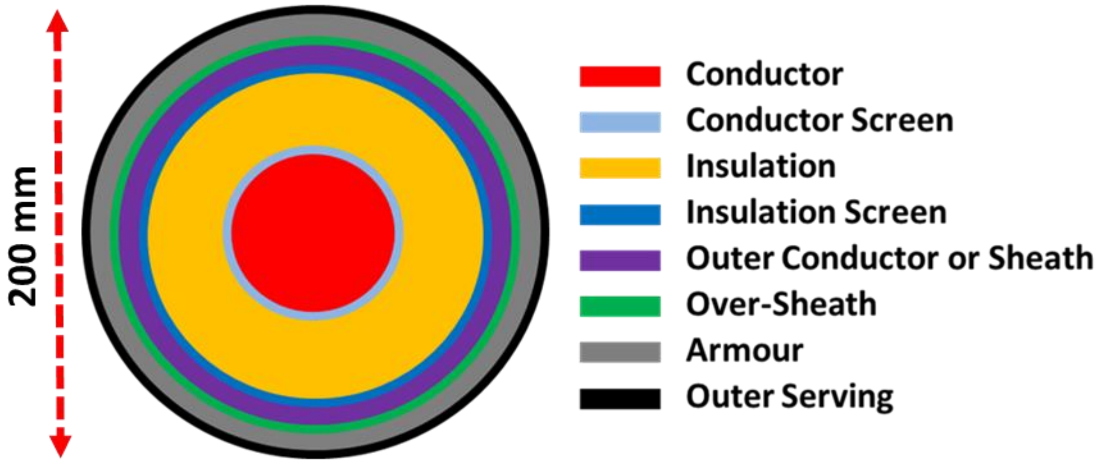

Figure 1.3: Schematic of a typical HV cable design structural components

In order to reduce resistive losses, a copper or aluminium material with high conductivity is normally used as the conductor for the electricity transmission (Simmons, 2001). There are two semi conducting screens: conductor and insulation screen. The semi-conducting conductor screen levels the conductor and insulation material interface because the insulation material can be damaged (Robinson, 1990, Motori *et al.*, 1991, Hosier *et al.*, 2008), by localised electrical stresses resulting from interface unevenness (Thue, 1999). The insulation material helps to maintain current flow along the cable axis and cross-linked polyethylene (XLPE) is the common modern insulation type used (Worzyk, 2009). The insulation screen function is similar to the semi-conducting screen and helps to maintain smooth electrical field profile across the insulation. A metallic sheath is also used to contain the electric field within the cable (Thue, 1999), serves to prevent water ingress in to the encased components and a limited mechanical protection (Nexans, 2004). The metallic sheath is protected from corrosion by the over-sheath. Further cable mechanical damage and water ingress are prevented by the stranded steel armouring and outer serving components (Thue, 1999).

Ohmic heating of the conductor is the largest source of electrical heat losses during the cable operation and electrical power transmission (Pilgrim, 2011) due to joule heating within the conductor. The heat loss is represented in equation (1.1) and the resistance value is dependent on the conductor temperature (equation 1.2 and 1.3) (Sivanagaraju and Satyanarayana, 2009).

$$W_{loss} = I^2R \tag{1.1}$$

$$R(T) = R\,(T_0)\,.\big(1 + \beta(T - T_0)\big) \tag{1.2}$$

$$R(T) = R\,(T_0)\,.\big(1 + \beta(T - T_0)\big) + (1 + ys + yp) \tag{1.3}$$

Where: W_{loss} is power (W), I is current (A), R is electrical resistance (Ω), β is temperature coefficient of resistance, T is temperature (°C) and T_0 is ambient temperature of the overlying environment. ys is a factor to quantify the increase of resistance due to the skin effect and yp is a factor to quantify the increase of resistance due to the proximity effect. Equation 1.2 is only true for direct current (DC) conditions while the addition $(1 + ys + yp)$ in equation 1.3, gives the alternating current (AC) resistance. DC cables have a lower operating temperature than AC cables.

1.3 Research Motivations, Contributions and Aims

The present maximum operating conductor temperature of submarine AC HV cables with XLPE insulation is 90^{o}C which can translate to cable surface temperatures of up to 70^{o}C (Swaffield *et al.*, 2008, Hughes *et al.*, 2015). Also non-XLPE insulations cables may have different thermal limits. This means the surrounding seawater-saturated sediments will experience thermal conditions typically only reached at approximately 2.8 km of burial under normal geothermal gradients (Boehler, 1996, Nagihara and Smith, 2005, Geohil, 2013, Christie and Nagihara, 2016). Despite the potential for such anomalously high temperatures, there has been very limited study on the actual temperatures generated around submarine cables, with only one reported field study (Meissner *et al.*, 2007), and limited numerical modelling work (Worzyk, 2009, Hughes *et al.*, 2015).

There are also only a few papers on the thermal properties of shelf sediments (Lovell, 1985a, Lovell, 1985b, Zimmerman, 1989, Jackson and Richardson, 2001, Kim *et al.*, 2007, Wheatcroft *et al.*, 2007, Goto *et al.*, 2012), and these solely consider conductive heat flow. However, recent numerical modelling by Hughes et al. (2015) suggests that for fully saturated marine sediments, heat transfer can occur by both conduction and convection, depending on cable surface temperature and sediment properties. Hughes et al. (2015) found that permeability is the overarching controlling factor, with the transition from conduction to convection expected as permeability increases to the range $10^{-11}m^2$ - $10^{-10}m^2$. In continental shelf settings, this means that fine-grained substrates would be predicted to have conductive heat transport, with a transition as grain size increases to convective heat transport in sands. If this is correct, there are implications for both the environment surrounding the cables, and the current that can be carried by the cables.

As several marine organisms are sensitive to minor ambient temperature changes, any such temperature increases in the surrounding sediment may cause significant impacts and displacements of living organisms dwelling within the near-surface environments (OSPAR, 2009b). The German Federal Maritime and Hydrographic Agency (BSH) have produced environmental regulations which set an acceptable limit of <2K (2^oC) above ambient temperature rise at 20 cm below the seabed and directly above the cable (OSPAR, 2009b, BSH, 2014), to minimise impacts on shallow-burrowing organisms. However, at the higher operational temperatures, there is also the potential for geochemical changes within the sediments.

In addition to the lack of knowledge of the potential impacts of the heat generated by the cable on the environment, there is also little knowledge of the relationship between the thermal properties of marine sediments and the current that may be reliably carried by submarine HV cables. This is controlled by a balance between resistive heating within the cable and how efficiently heat is lost to the environment, such that the cable remains below its design temperature. In the terrestrial environment the substrate in which they are buried, often involving variability in backfilling during trenching, has a significant effect on cable current ratings (de Leon and Anders, 2008, Swaffield *et al.*, 2008). The IEC 60287 standard (BS-IEC-60287-1-1:2014, 2014) to estimate the current rating of buried cables assumes terrestrial conditions: an isothermal ground temperature, homogeneous burial sediment, conductive heat transfer and a simple model for the thermal resistance of the surrounding sediments. These basic assumptions may not be appropriate in any case for continental shelves given the wide range of substrates and their physical properties (muds, sands, gravels and even bedrock) (van Landeghem *et al.*, 2014), due to natural depositional processes. However, if convective heat transport occurs, then the greater efficiency may allow significantly higher currents to be carried by the cables.

Thus, the specific objectives of the PhD are to:

1) Develop a new, stable and operational experimental HV tank approach to measure and provide a comprehensive understanding of the burial thermal regimes experienced by submarine HV cables.
2) Use artificial ballotini sediments with varying grain sizes, typical to the continental shelf sediments e.g. coarse silt, fine sand and coarse sands, to understand the varying thermal regimes around submarine HV cables as well as the impact of the surrounding sediments properties.
3) Carry out further experiments using natural sediments to understand how applicable the results of (1) and (2) to the natural environments.
4) Evaluate the sediment thermal properties using the acquired temperature time series data.

1.4 Thesis Structure

This chapter (**Chapter 1**) has introduced the importance, typical design and heat losses associated with submarine HV cables; as they are used for electricity transmission by all forms of renewable energy infrastructures. It further provides the research motivations and aims.

Chapter 2 presents background and review of the methodologies and governing equations used to study heat transfer (conduction and convection) within sediments as well as a synthesis of published sediment thermal properties within near surface sediments (less than 1m depth).

Chapter 3 presents the first set of temperature measurements from a 2D laboratory experiment designed as an analogue to a buried submarine HV cable. A range of realistic cable surface temperatures were used to identify how the surrounding burial thermal regimes and heat transport mechanisms change using artificial sediments (glass beads) with varying permeability and grain size ranges of typical shelf sediments (pre-sieved coarse silt, fine sand and very coarse sand). The results were explored to understand the conditions for occurrence of convection and their implications to the surrounding environments and cable performance.

Having developed the laboratory temperature time series measurement method using artificial sediments presented in **Chapter 3**. **Chapter 4** presents the next series of experiments using natural fine sand sediments with varying cable surface temperatures. This is aimed at testing the robustness of the developed conditions of occurrence of both conduction and convection heat transfer using a natural sediment with a mixture of grain shape and composition.

Chapter 5 presents evaluation of the sediment thermal properties (thermal diffusivity, conductivity and volumetric heat capacity) from the observed temperature time series measurements presented in Chapter 3 and 4; using the heat transfer governing equations described in Chapter 2.

The final chapter (**Chapter 6**) summaries the various thermal regimes experienced by submarine HV cable buried with coarse silt, fine sand and very coarse sand sediments. Also presents summaries of the impact of varying sediment physical and thermal properties on the surrounding burial thermal environments of submarine HV cables.

Page intentionally left blank.

2

Sediment Heat Transfer

2.1 Heat Transfer Mechanisms

Heat transfer is the exchange of thermal energy between physical systems, depending on the temperature and pressure difference. The fundamental modes of heat flow are conduction or diffusion, convection and radiation. However, conduction and convection are the two main heat transfer modes through sediments as they require a conduit medium or material for their occurrence.

2.1.1 Conductive and Convective Heat Transfer

Conduction may be viewed as a diffusive process involving the transfer of energy due to random molecular motion from the more energetic to the less energetic particles of a substance. Thus, heat transfers in the direction of decreasing temperature. Convective heat transfer is comprised of two mechanisms. In addition to energy transfer due to random molecular motion (diffusion), there is also energy being transferred by the bulk, or macroscopic, motion of the fluid. This fluid motion is associated with the fact that, at any instant, large numbers of molecules are moving collectively or as aggregates. Such motion, in the presence of a temperature gradient, will give rise to heat transfer. Because the molecules in the aggregate retain their random motion, the total heat transfer is then due to a superposition of energy transport by the random motion of the molecules and by the bulk motion of the fluid. Thus, the term convection is used when referring to this cumulative transport and the term advection when referring to transport due to bulk fluid motion (Carslaw and Jaeger, 1959, Incropera and Dewitt, 1985).

This chapter and other subsequent chapters explores the issue of understanding the heat transfer mechanisms from buried submarine HV cables to the surrounding sediments. The literature review (this chapter) and subsequent chapter of the data analysis are based mainly on conductive heat flow while the transition or occurrence of non-conductive characteristics are referred as the onset/occurrence of convective heat flow.

2.2 Conductive Heat Transfer

2.2.1 Conduction Rate Equation

The key objectives in conductive heat transfer analysis are to determine the temperature distribution and heat transfer rate (Incropera and Dewitt, 1985), considering various common geometries. Thus, consider the heat flow through a cylindrical rod of known material, insulated on its lateral surface and its two end points are maintained at different temperatures where $T1 > T2$ (Figure 2.1). The temperature difference causes conduction heat transfer in the positive x direction. According to Fourier's law, the heat flow rate (Q) through the cylindrical rod is a function of the temperature difference ($T1 - T2,\ \Delta T$) between point x_1 and x_2, the geometry (i.e. the cross-sectional area (A) and rod length (Δx)) and the material property of the rod (Carslaw and Jaeger, 1959, Incropera and Dewitt, 1985). Thus, Fourier's Law can be expressed as Equation (2.1).

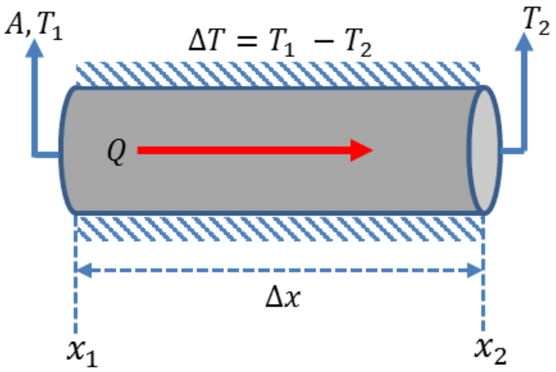

Figure 2.1: Heat transfer along a horizontal rod

$$Q = \lambda A \frac{\Delta T}{\Delta x} \tag{2.1}$$

Evaluating Equation (2.1) in the limit for any temperature difference (ΔT) across a length change (Δx) as both $\Delta x, \Delta T \rightarrow 0$, the heat rate (Q) is given as Equation (2.2). Or in terms of heat flux (q) as Equation (2.3) (Incropera and Dewitt, 1985). The heat flux (q) with units W/m^2, is a more useful quantity defined as the heat transfer per unit area. The minus sign is necessary because heat is always transferred in the direction of decreasing temperature. The proportionality constant λ is a transport property known as the thermal conductivity and it's units are W/mK.

$$Q = -\lambda A \frac{dT}{dx} \tag{2.2}$$

$$q = \frac{Q}{A} = -\lambda \frac{dT}{dx} \tag{2.3}$$

Thus, Equation (2.3) is the one-dimensional (1D) form of Fourier's law of heat conduction. Also recognising that heat flux (q) is a vector quantity, a more general statement of the conduction rate equation (Fourier's Law), can be expressed as Equation (2.4), where $\mathrm{T}(\mathrm{x}, \mathrm{y}, \mathrm{z})$ is the scaler temperature field.

$$q = -\lambda \nabla T = -\lambda \left(i \frac{\partial T}{\partial x} + j \frac{\partial T}{\partial y} + k \frac{\partial T}{\partial z} \right) \tag{2.4}$$

2.2.2 1D Steady State Heat Conduction: Plane Slab

One dimensional (1D) steady state heat transfer conditions refer to situations for which only one coordinate is needed to describe the spatial variation of the dependent variable as well as the temperature at each point is independent of time due to steady flow of enegy (Carslaw and Jaeger, 1959, Incropera and Dewitt, 1985).

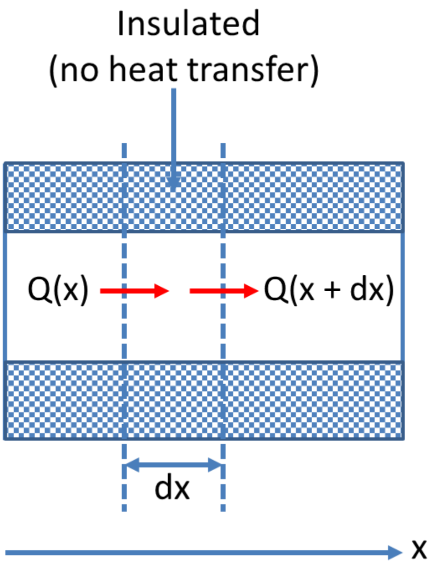

Figure 2.2: One - dimensional heat conduction through a plane slab

Thus, the temperature distribution through a plane slab (Figure 2.2) can be obtained by solving the heat equation with the appropriate boundary conditions (Carslaw and Jaeger, 1959, Incropera and Dewitt, 1985). From Equation (2.2), the heat transfer rate in at left (at x) is

$$Q(x) = -\lambda\left(A\frac{dT}{dx}\right)_x \tag{2.5}$$

On the right, the heat transfer rate is

$$Q(x+dx) = Q(x) + \left.\frac{dQ}{dx}\right|_x dx + \ \ldots\ldots \tag{2.6}$$

From Equations (2.5) and (2.6) as well as using the conditions on the overall heat flow

$$Q(x) - \left(Q(x) + \frac{dQ}{dx}(x)dx + \cdots\right) = 0 \tag{2.7}$$

Thus, Equation (2.8) can be obtained, by taking the limit as dx approaches zero;

$$\frac{dQ(x)}{dx} = 0, \tag{2.8}$$

Or Equation (2.9) after substituting Equation (2.5) in (2.8)

$$\frac{d}{dx}\left(\lambda A\frac{dT}{dx}\right) = 0 \tag{2.9}$$

If λ is constant, where the properties of the slab are independent of temperature, Equation (2.9) reduces to

$$\frac{d}{dx}\left(A\frac{dT}{dx}\right) = 0 \tag{2.10}$$

Or (using the chain rule)

$$\frac{d^2T}{dx^2} + \left(\frac{1}{A}\frac{dA}{dx}\right)\frac{dT}{dx} = 0 \qquad (2.11)$$

Equation (2.10) or (2.11) describes the temperature field for quasi-one-dimensional steady state (i.e. no time dependence) heat transfer. Thus, the heat transfer through a plane slab (e.g. Figure 2.2) with constant area (A), Equation (2.10 or 2.11) becomes

$$\frac{d^2T}{dx^2} = 0 \qquad (2.12)$$

Equation (2.12) can be integrated immediately to

$$\frac{dT}{dx} = C_1 \qquad (2.12)$$

And further integration of Equation (2.12) gives

$$T(x) = C_1x + C_2 \qquad (2.13)$$

Thus, Equation (2.13) describes the temperature field through a plane wall, where C_1 and C_2 are the constants of integration(Carslaw and Jaeger, 1959, Incropera and Dewitt, 1985).

2.2.3 1D Steady State Heat Conduction: Non - Planar Geometry

For non-planar (radial) geometries such as cylindrical (Figure 2.3) and spherical (Figure 2.4) systems where temperature gradient is often experienced in the radial (r) direction only and may therefore be treated as one dimensional. Thus, the temperature distribution through cylindrical and spherical systems under steady-state conditions with no heat generation, can be obtained by solving the appropriate heat equation (Carslaw and Jaeger, 1959, Incropera and Dewitt, 1985).

2.2.3.1 Cylindrical Shell

Considering a hollow cylindrical shell configurations $(A = 2\pi rL)$ where the inner (hot fluid) and outer surfaces (cold fluid) are exposed to fluid at different temperatures (Figure 2.3) (Incropera and Dewitt, 1985) and according to Fourier's Law, the rate at which heat is conducted through the solid cylindrical surface (heat transfer rate per unit length) can be expressed as Equation (2.13). Similarly, for steady state conditions, with no heat generation, the appropriate heat equation involves expressing Equation (2.9) as Equation (2.14).

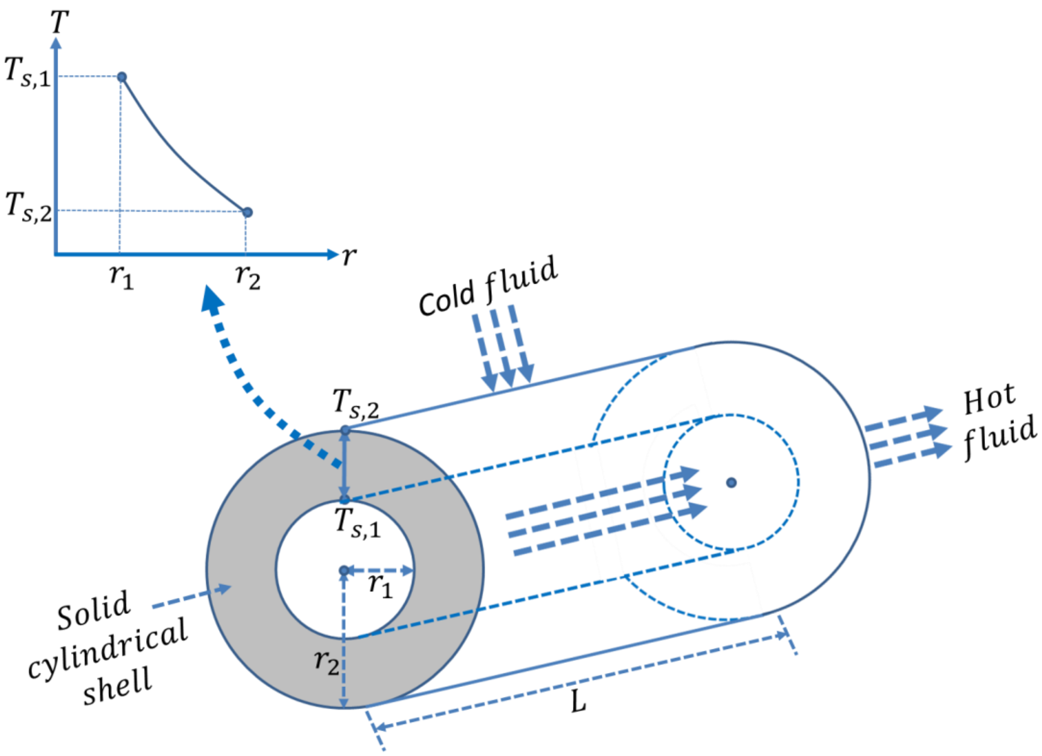

Figure 2.3: Conduction in a cylindrical shell

$$Q = -\lambda(2\pi rL)\frac{dT}{dr} \tag{2.13}$$

$$\frac{1}{r}\frac{d}{dr}\left(\lambda r\frac{dT}{dr}\right) = 0 \tag{2.14}$$

Where λ is constant, the area $(A = 2\pi rL)$ is normal to the heat transfer direction and from Equation (2.13 and 2.14), in the radial direction, the conduction heat transfer rate (Q) is constant. Thus, Equation (2.15) is the second order differential equation for the temperature distribution. With first integration generates Equations (2.16) or (2.17) and a second intergration gives the general solution of the temperature distribution (Equation 2.18) through the cylinder, where C_1 and C_2 are constants of integration (Carslaw and Jaeger, 1959, Incropera and Dewitt, 1985).

$$\frac{d}{dr}\left(r\frac{dT}{dr}\right) = 0 \qquad (2.15)$$

$$r\frac{dT}{dr} = C_1 \qquad (2.16)$$

$$dT = C_1\frac{dr}{r} \qquad (2.17)$$

$$T(r) = C_1 In(r) + C_2 \qquad (2.18)$$

2.2.3.2 Spherical Shell

Considering a hollow spherical configurations ($A = 4\pi r^2$) where the inner (hot fluid) and outer surfaces (cold fluid) are exposed to fluid at different temperatures (Figure 2.4) (Incropera and Dewitt, 1985); and according to Fourier's Law, the rate at which heat is conducted through the solid spherical surface can be expressed as Equation (2.19).

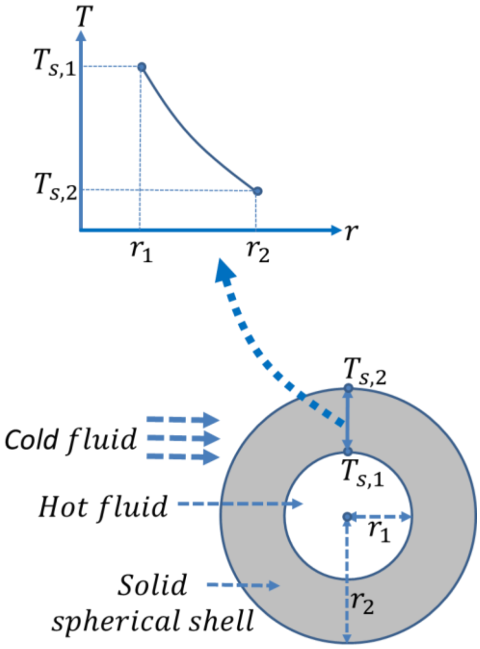

Figure 2.4: Conduction in a spherical shell

$$Q = -\lambda(4\pi r^2)\frac{dT}{dr} \tag{2.19}$$

Where λ is constant, the area $(A = 4\pi r^2)$ is normal to the heat transfer direction and from Equation (2.19), in the radial direction, the conduction heat transfer rate (Q) is constant as its independent of the radial direction (r). Thus, for steady state conditions with no heat generation, Equation (2.20) is the appropriate second order differential equation for the temperature distribution. Its initial integration generates Equations (2.21) and a further integration gives the general solution of the temperature distribution (Equation 2.22) through the sphere, where C_1 and C_2 are constants of integration (Carslaw and Jaeger, 1959, Incropera and Dewitt, 1985).

$$\frac{d}{dr}\left(r^2\frac{dT}{dr}\right) = 0 \tag{2.20}$$

$$\frac{dT}{dr} = \frac{C_1}{r^2} \tag{2.21}$$

$$T(r) = \frac{C_1}{r} + C_2 \tag{2.22}$$

2.2.4 2D Steady State Conduction

It is necessary to account for multi-dimensional effects of heat transfer problems as 1D solutions are grossly oversimplified. Thus, the energy conservation method is applied to determine the manner in which temperature is distributed multi-dimensionally through a medium. This involve defining a differential control volume, relevant energy transfer processes and applying the appropriate rate equations (Carslaw and Jaeger, 1959, Incropera and Dewitt, 1985).

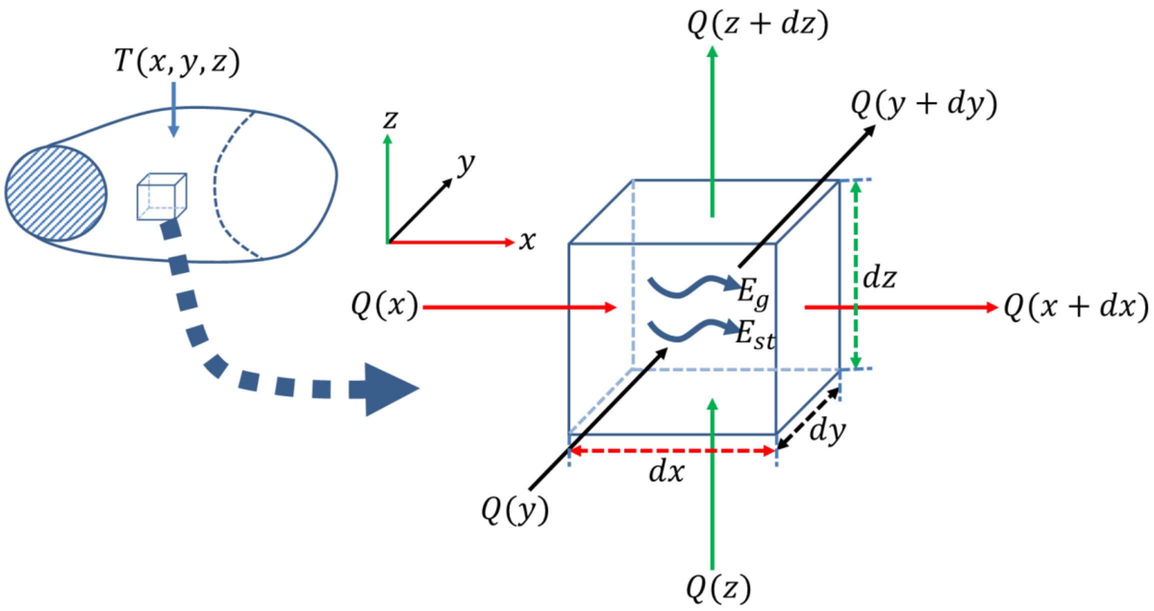

Figure 2.5: Heat conduction analysis 3D Cartesian coordinates using differential control volume, $(dx\ dy\ dz)$.

Firstly, Figure 2.5 (Incropera and Dewitt, 1985), defines a microscopically small (differential) control volume, $(dx\quad dy\ dz)$ for a homogeneous medium in which temperature gradients exist and the temperature distribution is in $T(x,y,z)$. Secondly, neglecting higher order terms, the Taylor series expansion is used to express the conduction heat rates $[Q(x), Q(y)\ and\ Q(z)]$ perpendicular to each opposite control surfaces (Equations 2.23a, 2.23b and 2.23c) at the coordinate locations $(x,\ y\ and\ z)$. This is due to the occurrence of conduction heat transfer through each control surface as a result of the temperature gradients. Also within the medium there may also be an energy source, E_g (Equations 2.24) and storage, E_{st} (Equations 2.25) expressions associated with the thermal energy generation rate and internal thermal energy stored by the material in the control volume. Thirdly, using the rate equations, Equations 2.26 expresses the energy conservation general form.

$$Q(x+dx) = Q(x) + \left.\frac{dQ}{dx}\right|_x dx \qquad (2.23a)$$

$$Q(y+dy) = Q(y) + \left.\frac{dQ}{dy}\right|_y dy \qquad (2.23b)$$

$$Q(z+dz) = Q(z) + \left.\frac{dQ}{dz}\right|_z dz \qquad (2.23c)$$

$$E_g = Q_{vol}\, dx\ dy\ dz \qquad (2.24)$$

$$E_{st} = \rho c_p \frac{dT}{dt}\, dx\ dy\ dz \qquad (2.25)$$

$$E_{in} + E_g - E_{out} = E_{st} \qquad (2.26)$$

Where Q_{vol} is the generated energy generation rate per unit volume in W/m^3, $\rho c_p \frac{dT}{dt}$ is the time rate of the internal energy change per unit volume. As the conduction rates constitute the energy inflow E_{in} and outflow E_{out}, Equation 2.27 is obtained by substituting Equations 2.23, 2.24 and 2.25 into Equation 2.26. Equation 2.27 can be re-writing as Equation 2.28 (Incropera and Dewitt, 1985).

$$\begin{aligned} Q(x) + Q(y) + Q(z) + Q_{vol}\, dx\ dy\ dz - Q(x+dx) - Q(y+dy) - Q(z+dz) \\ = \rho c_p \frac{dT}{dt}\, dx\ dy\ dz \qquad (2.27) \end{aligned}$$

$$-\left.\frac{dQ}{dx}\right|_x dx - \left.\frac{dQ}{dy}\right|_y dy - \left.\frac{dQ}{dz}\right|_z dz + Q_{vol}\, dx\ dy\ dz = \rho c_p \frac{dT}{dt}\, dx\ dy\ dz \qquad (2.28)$$

Also from Fourier's law, the conduction heat transfer rate can be obtained by multiplying each heat flux component by the appropriate control surface (differential) area (Equations 2.29a, 2.29b and 2.29c). Finally, the general form of heat diffusion equation (Equations 2.30) (Carslaw and Jaeger, 1959, Incropera and Dewitt, 1985) can be obtained by substituting Equations 2.29 into Equations 2.28 and dividing out the control volume dimensions $(dx\ dy\ dz)$.

$$Q(x) = -\lambda\,(dy\ \ dz)\ \frac{dT}{dx} \tag{2.29a}$$

$$Q(y) = -\lambda\,(dx\ \ dz)\ \frac{dT}{dy} \tag{2.29b}$$

$$Q(z) = -\lambda\,(dx\ \ dy)\ \frac{dT}{dz} \tag{2.29c}$$

$$\frac{d}{dx}\left(\lambda\frac{dT}{dx}\right) + \frac{d}{dy}\left(\lambda\frac{dT}{dy}\right) + \frac{d}{dz}\left(\lambda\frac{dT}{dz}\right) + Q_{vol} = \rho c_p \frac{dT}{dt} \tag{2.30}$$

It is implicit in Equation 2.30 that the thermal conductivity is independent of the coordinate direction. Thus, Equations 2.30 provides the basic tool for conduction (diffusion) heat transfer analysis and process. Also if the thermal conductivity is constant, the heat diffusion equation can be simplified as Equation 2.31 and Equation 2.32 under steady-state conditions with no change in energy storage amount. Furthermore, where there is no energy generation, the heat diffusion equation further reduces to Equation 2.33 in three dimension (x, y, z) and Equation 2.34 in two dimension (x, y) (Carslaw and Jaeger, 1959, Incropera and Dewitt, 1985).

$$\frac{d^2T}{dx^2} + \frac{d^2T}{dy^2} + \frac{d^2T}{dz^2} + \frac{Q_{vol}}{\lambda} = \frac{1}{\alpha}\frac{dT}{dt} \tag{2.31}$$

$$\frac{d^2T}{dx^2} + \frac{d^2T}{dy^2} + \frac{d^2T}{dz^2} + Q_{vol} = 0 \tag{2.32}$$

$$\frac{d^2T}{dx^2} + \frac{d^2T}{dy^2} + \frac{d^2T}{dz^2} = 0 \tag{2.33}$$

$$\frac{d^2T}{dx^2} + \frac{d^2T}{dy^2} = 0 \tag{2.34}$$

Where $\alpha = \frac{k}{\rho C_p}$ is the thermal diffusivity and it's a key thermophysical property which is the ratio of the thermal conductivity λ of the medium to the thermal capacitance ρC_p.

There are two major objectives in any conduction analysis. The first is to determine the temperature distribution in the medium. Thus, 2D heat transfer problems (e.g. Submarine HV cable problem) require determining the temperature distribution $T\ (x, y)$ in both the x and y directions by solving the appropriate form of the heat equation (Equation 2.34). After solving Equation 2.34 for $T\ (x, y)$, the second major objective is to simply determine the heat flux components q_x and q_y by applying the rate equation (2.3) or (2.4) (Incropera and Dewitt, 1985).

Several methods can be used to solve equation 2.33 or 2.34 such as the analytical (Carslaw and Jaeger, 1959, Arpaci, 1966, Ozisik, 1980, Incropera and Dewitt, 1985), analytical and numerical (finite-difference) approaches (Myers, 1971, Adams and Rogers, 1973, Incropera and Dewitt, 1985). Analytical methods provide solutions to simple conditions while the graphical approach may be used to obtain rough estimate of the temperature field. However, numerical or finite-difference methods of solving equation 2.33 or 2.34 provides very accurate results at discrete points, can accommodate complex conditions, well suited for use with high speed digital computers and often offer the only means by which multi-dimensional conduction problems can be solved (Myers, 1971, Adams and Rogers, 1973, Incropera and Dewitt, 1985).

2.2.4.1 Discretization of the Steady State Heat Equation

As numerical solution enables determination of the temperature field at only discrete points, the first step in any numerical analysis must therefore be to select these discrete points. This is done by subdividing the medium of interest into a number of small regions and assigning to each region a reference point (its center), thus forming a nodal network (grid) which are aggregates of these nodes (Figure 2.6) (Incropera and Dewitt, 1985).

If the x and y locations are designated by the m and n indices, respectively (Figure 2.6). Thus, determination of the temperature distribution numerically dictates that an appropriate conservation equation be written for each of the points in the nodal network. The resulting set of equation may then be solved simultaneously for the temperature at each node. For any node of a 2D system with no generation and uniform thermal conductivity, the exact form of the energy conservation requirement is given by the heat equation 2.34. However, if the system is characterised in terms of a nodal network, it is necessary to work with an approximate, or finite difference form of equation 2.34 and this can be expressed as:

$$\left.\frac{\partial^2 T}{\partial x^2}\right|_{m,n} \approx \frac{T_{m+1,n} + T_{m-1,n} - 2T_{m,n}}{(\Delta x)^2} \qquad (2.35)$$

$$\left.\frac{\partial^2 T}{\partial y^2}\right|_{m,n} \approx \frac{T_{m,n+1} + T_{m,n-1} - 2T_{m,n}}{(\Delta y)^2} \qquad (2.36)$$

Where the value of the derivative at the m, n nodal point is approximated from the second derivative temperature gradient $\frac{\partial^2 T}{\partial x^2}, \frac{\partial^2 T}{\partial y^2}$ in both the x and y directions respectively and expressed as a function of the neighbouring nodal temperatures.

Using a network for which $\Delta x = \Delta y$ and substituting equations 2.35 and 2.36 in to equation 2.34, the differential equation is reduced to an approximate algebraic equation 2.37. Thus the numerical solution of equation 2.34 at any nodal point simply requires that the sum of the temperatures associated with the neighbouring nodes be four times the temperature of the node of interest (Figure 2.6) (Incropera and Dewitt, 1985).

$$T_{m,n+1} + T_{m,n-1} + T_{m+1,n} + T_{m-1,n} - 4T_{m,n} = 0 \qquad (2.37)$$

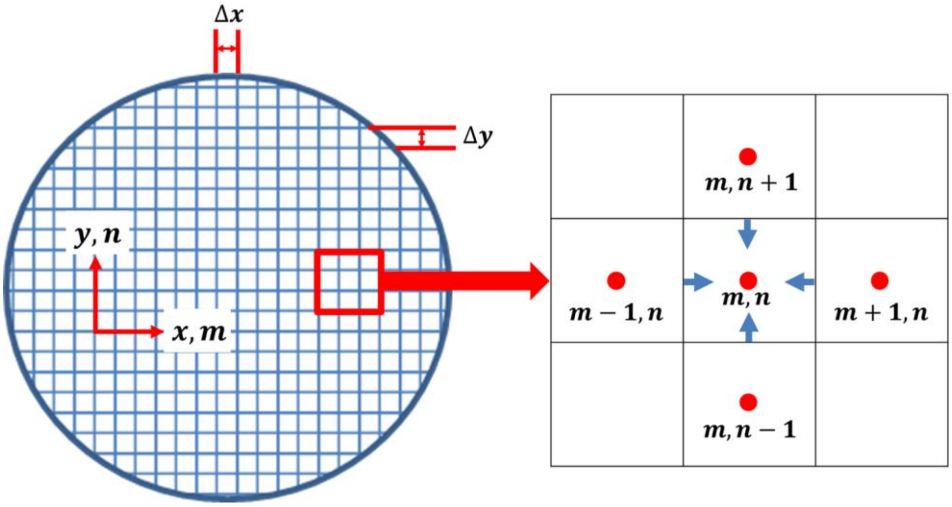

Figure 2.6: Nodal network and finite difference approximation approach for 2D heat conduction to an interior node m, n from its neighbouring nodes.

2.2.5 Transient Conduction

Many heat transfer problems are time dependent and such unsteady or transient problems arise due to changes in the system conditions such as a heat source or sink. The temperature at each point in the system will also begin to change and continues until a steady state temperature distribution is reached. Thus, for 2D systems with constant material thermal conductivity, the time dependence of the temperature distribution $T\,(x, y)$ within the system during a transient process can be determined by solving the appropriate form of the heat equation (Equation 2.38) (Carslaw and Jaeger, 1959, Incropera and Dewitt, 1985).

$$\frac{\partial^2 T}{\partial x^2} + \frac{\partial^2 T}{\partial y^2} + \frac{Q_{vol}}{\lambda} = \frac{1}{\alpha}\frac{\partial T}{\partial t} \tag{2.38}$$

2.2.5.1 Discretization of the Transient Heat Equation

As introduced in section 2.2.4.1 for steady state conditions, similarly numerical solutions are easily extended to transient problems (Myers, 1971, Adams and Rogers, 1973, Incropera and Dewitt, 1985) and are preferred for similar reasons to the analytical solutions (Carslaw and Jaeger, 1959, Arpaci, 1966, Ozisik, 1980). Thus for 2D systems under transient conditions with constant thermal conductivity and no internal generation, the general form of the heat diffusion equation 2.30 can be simplified as equation 2.39.

$$\frac{1}{\alpha}\frac{\partial T}{\partial t} = \frac{\partial^2 T}{\partial x^2} + \frac{\partial^2 T}{\partial y^2} \tag{2.39}$$

Similarly, the approximations to the spatial derivatives as prescribed by equations 2.35 and 2.36 can be used to obtain the finite difference form of equation 2.39. Also the m and n subscripts may be used to designate the x and y locations of discrete nodal points (Figure 2.6). However, equation 2.39 must be discretised both in space and time. Thus the finite difference approximation to the time derivative in equation 2.39 can be expressed as equation 2.40:

$$\left.\frac{\partial T}{\partial t}\right|_{m,n} \approx \frac{T_{m,n}^{p+1} - T_{m,n}^{p-1}}{2(\Delta t)} \tag{2.40}$$

Where p denotes the time dependence T, and the time derivative is expressed in terms of the difference in temperature associated with new $(p+1)$ and previous $(p-1)$ times. Hence calculation must be performed at successive times separated by twice the time interval $2(\Delta t)$. Substituting equations 2.35, 2.36 and 2.40 into equation 2.39, the explicit form of the finite difference equation 2.41, for any interior node, m, n (Figure 2.6) can be obtained (Incropera and Dewitt, 1985).

$$\frac{1}{\alpha}\frac{T_{m,n}^{p+1}-T_{m,n}^{p-1}}{2(\Delta t)} = \frac{T_{m+1,n}^{p}+T_{m-1,n}^{p}-2T_{m,n}^{p}}{(\Delta x)^2}+\frac{T_{m,n+1}^{p}+T_{m,n-1}^{p}-2T_{m,n}^{p}}{(\Delta y)^2} \qquad (2.41)$$

2.2.6 Summary

One of the key objectives, in any conduction analysis, are first to determine the temperature distribution through the medium. Thus, the equations for the temperature distributions and associated rate equations at which heat is conducted through each of the three common geometries - plane wall (Equation 2.13), cylindrical (Equation 2.18) and spherical (Equation 2.22) systems were derived for one dimensional steady state conditions with no heat generation. Also, the temperature gradient is often experienced only in the radial directions for cylindrical or spherical heat sources. Hence, these equations, their corresponding assumptions and applications will aid in solving the submarine HV cable problem of understanding the heat transfer mechanisms through the surrounding sediments; presented in chapter 3 and 4. Furthermore, it is necessary to account for multi-dimensional effects of heat transfer problems. Thus, the derived Equations 2.39 and 2.34 can be used to describe the 2D temperature distribution away from buried submarine HV cables during transient and steady state heat conduction respectively. Finally, due to the inherent and very accurate nature of the discretization process for handling geometrical complexities and multi-dimensional conduction problems, it is necessary to use a finite-difference solution of solving equation 2.39 and 2.34.

2.3 Convective Heat Transfer

Although the mechanism of conduction or diffusion contribute to convection heat flow, the overriding contribution is from the bulk fluid motion. In order to develop a better understanding of the nature of convection, consider fluid flow over a flat plate (Figure 2.7a), where the free stream fluid velocity u_∞ with temperature T_∞ not equal to the surface temperature of the of the flat plate (T_s); $(T_s \neq T_\infty)$. Thus, a key problem in examining convection is determining the boundary conditions at the plate surface exposed to the flowing fluid as well as the features of the fluid motion. Schematically the conditions near the surface are illustrated in Figure 2.7 (Incropera and Dewitt, 1985).

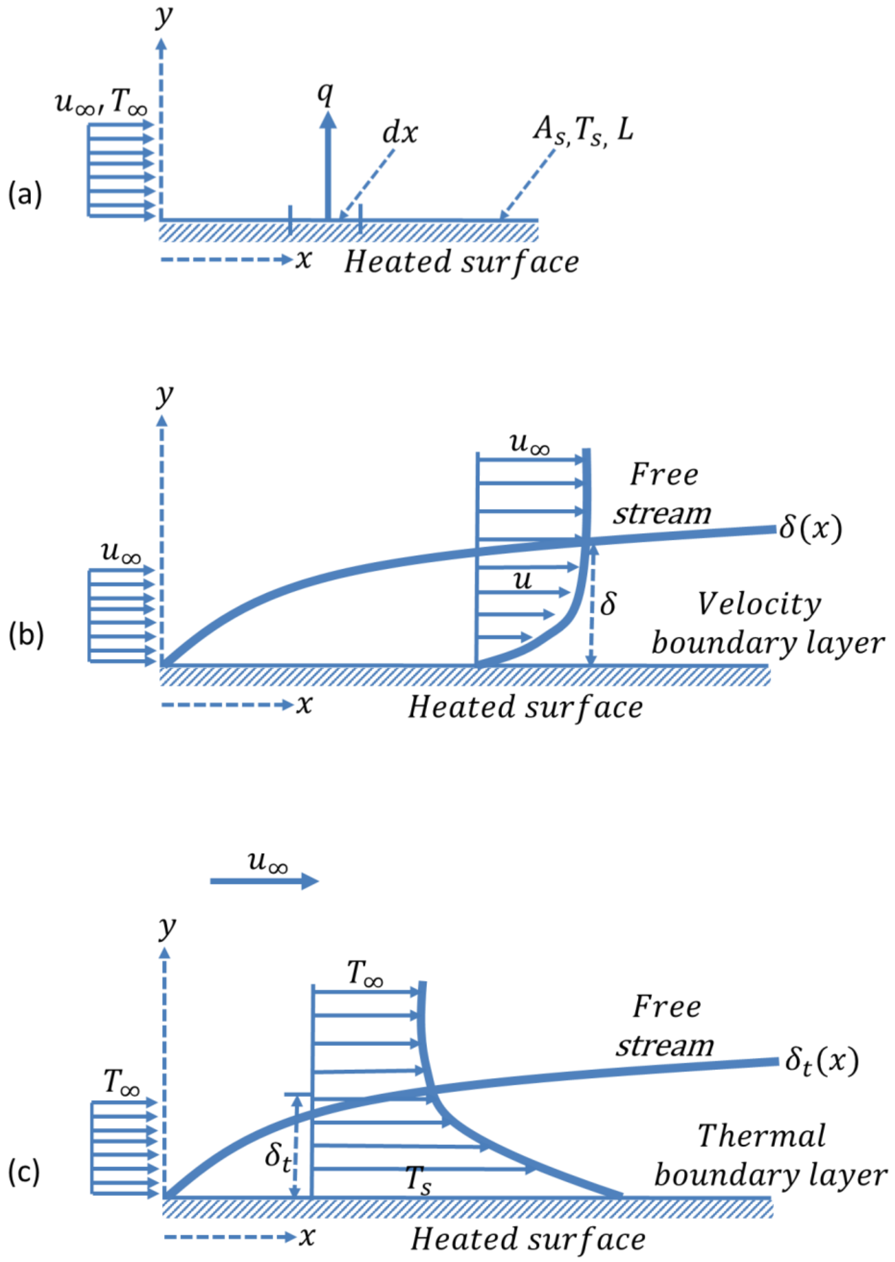

Figure 2.7: Convection heat transfer effects on a heated flat plate surface (a), velocity (b) and temperature (c) boundary layer development.

During fluid flow over a surface, the velocity of the fluid particles is zero at the plate surface and causes retardation of the particle motion within the adjoining fluid layer. This retardation of adjoining fluid particle motion continues until a distance $y = \delta$ from the surface when the effect becomes negligible as it approaches the freestream value u_∞. The quantity δ is termed the boundary layer thickness and boundary layer velocity profile refers to the manner in which u varies with y through the velocity boundary layer (Figure 2.7b). Thus, the boundary layer grows (δ increases with x) as the effects of viscocity penetrates further into the free stream with increasing y distance from the surface (Incropera and Dewitt, 1985). Similarly, Figure 2.7c, shows that at the plate surface, the temperature profile is uniform with $T(y) = T_\infty$ and fluid particles achieve thermal equilibrium at the plate surface. However, temperature gradient develop within the fluid layer as the surface particles exchange heat energy with those in the adjoining fluid layer. Thus, the thermal boundary layer thickness δ_t is the fluid region in which the temperature gradients exist and the thermal boundary layer grows with increasing y distance from the plate surface as the effect of the heat transfer penetrates further into the free stream (Incropera and Dewitt, 1985).

Thus, the heat flux (q) can be expressed as Equation (2.42) and where δ_t is generally unknown, the heat transfer flux is normally calculated using Equation 2.43. $\frac{\lambda_f}{\delta_t}$ represents the convective heat transfer coefficient (h) with units as W/m^{2}K and Equation 2.43 is refered to as Newton's Law of Cooling. The relationship between conditions in the thermal boundary layer and the convection heat transfer coefficient can be evaluated at any distance from the surface. Also, as there is no fluid motion at the surface, heat transfer occurs only by conduction. Thus, applying Fourier's law to the fluid at $y = 0$ gives the local heat flux as Equation 2.44 and by combining Equation 2.43, Equation 2.45 is obtained (Incropera and Dewitt, 1985). The heat transfer rate is determined by the conditions that strongly influence the temperature gradient $\left.\frac{dT}{dy}\right|_{y=0}$ within the thermal boundary layer. Furthermore, at constant $(T_s -$

T_∞) and with increasing x, δ_t increases, $\left.\frac{dT}{dy}\right|_{y=0}$ decreases as well as q and h decreases.

$$q = \frac{Q}{A} = \frac{\lambda_f(T_s - T_\infty)}{\delta_t} \qquad (2.42)$$

$$q = \frac{Q}{A} = h(T_s - T_\infty) \qquad (2.43)$$

$$q = -\lambda_f \left.\frac{dT}{dy}\right|_{y=0} \qquad (2.44)$$

$$h = \frac{-\lambda_f \left.\frac{dT}{dy}\right|_{y=0}}{(T_s - T_\infty)} \qquad (2.45)$$

Thus, Equation 2.43 encompasses all the effects that influence the convection heat transfer mechanism and controlled by the boundary layers that propagate on the surface. Also, the conditions in the boundary layer are influenced by a multiplicity of independent variables such as the surface geometry, nature of the fluid motion (flow condition), and many fluid thermodynamic and transport properties such as density, viscosity, thermal conductivity and specific heat (Incropera and Dewitt, 1985).

2.3.1 Laminar and Turbulent Flow

An essential first step in the treatment of any convection issue, is to determine whether the boundary layer is laminar or turbulent (Turcotte and Schubert, 2002). The boundary layer is initially laminar, but at some distance from the leading edge, transition to turbulent flow begins to occur (Figure 2.8). The fluid motion within the laminar boundary region is highly ordered and identification of streamlines along which particles move are possible. The streamline fluid motions are characterized in the x and y directions by velocity components, u and v respectively. Fluid fluctuations begin to develop in the transition region, and the boundary layer eventually becomes completely turbulent. In contrast, the fluid motion is highly irregular and characterized by velocity fluctuations. Thus, momentum and energy transfer are enhanced mainly due to interchange of fluid particles as well as increased surface friction and convection heat transfer rate. Also the turbulent region is accompanied by significant increases in the boundary layer thicknesses, the wall shear stress, and the convection coefficient. Figure 2.8 schematically describes immediate vicinity above buried heat source within water saturated sediments and the associated three different boundary regions that may be delineated; the laminar region, buffer region and turbulent region. Within the laminar region, transport is dominated by diffusion and the velocity profile is nearly linear. There is an adjoining buffer region in which diffusion and turbulent mixing are comparable, and a further turbulent zone in which transport is dominated by turbulent mixing (Incropera and Dewitt, 1985, Turcotte and Schubert, 2002).

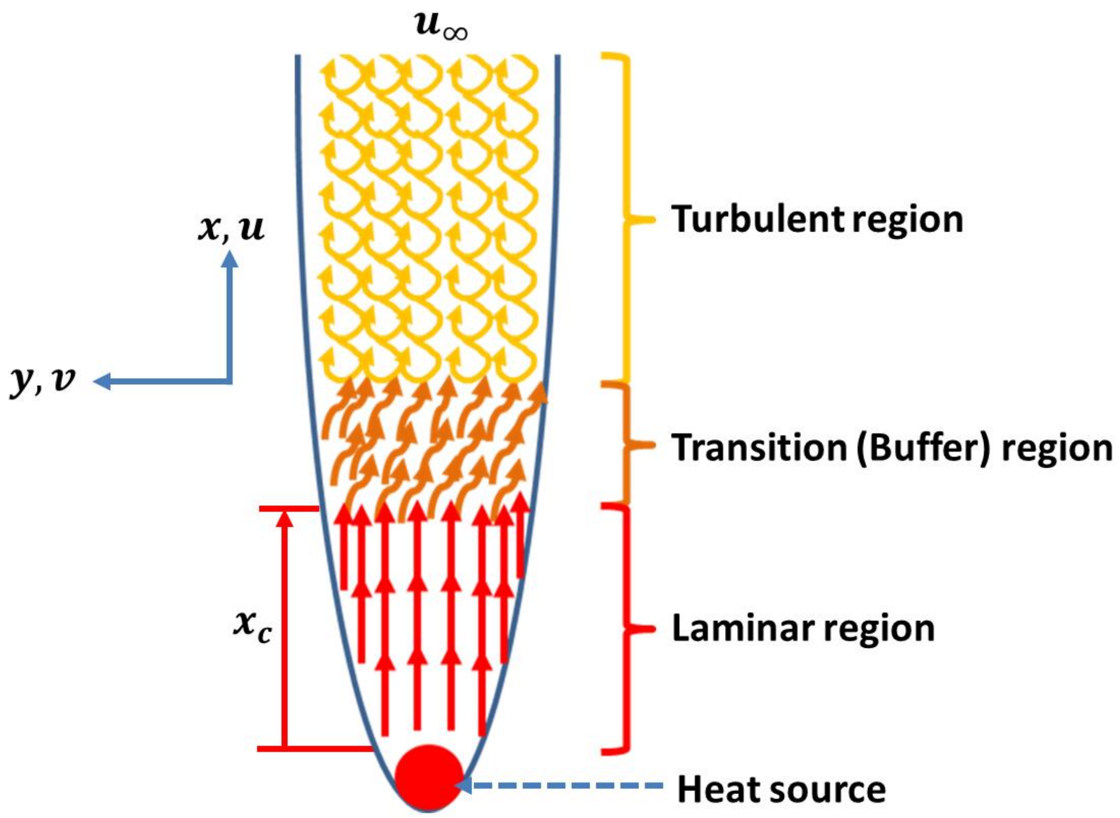

Figure 2.8: Boundary layer development within heated pore fluid above the vicinity of a buried heat source.

In calculating boundary layer behaviour, it is reasonable to assume that the transition from laminar to turbulent zone begins at some location x_c. This location is determined by a dimensionless grouping of variables called the Reynolds number, Re_x, (Equation 2.46). Where the characteristic length x is the distance from the leading edge. The critical Reynolds number is the value of Re_x for which transition begins and for external flow, it is known to vary from 10^5 to 3 x 10^6, (Turcotte and Schubert, 2002) depending on surface roughness, the turbulence level of the free stream and the nature of the pressure variation along the surface. A representative value of equation 2.47 is generally assumed for boundary layer calculations.

$$Re_x = \frac{\rho \mu_\infty x}{\mu} \qquad (2.46)$$

$$Re_{x,c} = \frac{\rho \mu_\infty x_c}{\mu} = 5\ x\ 10^5 \qquad (2.47)$$

The resistance of a porous medium to flow depends on the size, number, and tortuosity of the fluid pathways through the solid matrix and a measure of this resistance is the permeability (k) of the medium. According to Darcy's law (1), the flow through a porous medium is linearly proportional to the applied pressure gradient and inversely proportional to the viscosity of the fluid. For a one-dimensional geometry in which the volumetric flow rate per unit area (u) is driven by the applied pressure gradient $(\frac{dp}{dx})$, Darcy's law takes the form (Equation 2.48):

$$u = -\frac{k}{\mu}\frac{dp}{dx} \qquad (2.48)$$

Where k is the permeability of the medium and μ is the dynamic viscosity of the fluid. Also the volumetric flow rate per unit area (u) has the dimensions of velocity, referred as the Darcy velocity and computed as the average velocity per unit area. The more permeable the medium is, the smaller is the pressure gradient required to drive flow. Also Darcy's law for vertical upward flow in sediments is given by equation (2.49) where the pressure increases more rapidly with depth than it does when the fluid is motionless.

$$v = -\frac{k}{\mu}\left(\frac{dp}{dy} - \rho g\right) \qquad (2.49)$$

Where v is the vertical Darcy velocity, ρ = fluid density and g = acceleration due to gravity.

2.3.2 Conservation of Mass and Energy Equations

The solution of one dimensional flows requires only Darcy's law and simple mass balance equation. However, two dimensional heat transport requires differential equations for conservation of mass and energy in two dimensions and Darcy's law (Turcotte and Schubert, 2002). At steady state heat flow (time-independent) with no density variations and no net (into or out) flow; the two dimensional conservation of mass for a viscous incompressible fluid is given as the continuity or conservation of fluid equation (equation 2.50). This equation can also be applied to flows in sediments if the solid matrix cannot deform and the velocity components are the Darcy velocities which is equivalent to the ordinary viscous fluid average velocity component in regards to mass and heat transport.

$$\frac{\partial u}{\partial x} + \frac{\partial v}{\partial y} = 0 \tag{2.50}$$

The energy equation for a two dimensional flow of incompressible fluid in sediment is given by equation 2.51

$$\rho_m c_{p_m} \frac{\partial T}{\partial t} + \rho_f c_{p_f} \left(u \frac{\partial T}{\partial x} + v \frac{\partial T}{\partial y} \right) = \lambda_m \left(\frac{\partial^2 T}{\partial x^2} + \frac{\partial^2 T}{\partial y^2} \right) \tag{2.51}$$

Equation 2.51 assumes same temperature (T) of the fluid and solid matrix, constant thermal conductivity (λ_m) for the diffusion of heat by conduction through the entire medium (right hand side). Also the thermal inertia term (left hand side) is a volumetric average as the thermal energy is stored both in the fluid filled pores and the solid matrix. The fluid density (ρ_f) and specific heat (c_{p_f}) are used in the advective terms (left hand side) because only the fluid transports heat. The horizontal (2.48) and vertical (2.49) equations for Darcy's velocities are further required for a complete solution (Turcotte and Schubert, 2002).

2.3.3 One Dimensional Heat Convection

As a buried heat source heats the surrounding sediments, the pore fluid becomes less dense and rises (Figure 2.9). A one dimensional solution can be obtained for the temperature depth dependence of the upwelling flow. Thus, for steady one dimensional up-flow, equation 2.50 and 2.51 is simplified as equation 2.52 and 2.53 respectively, where v is a constant and equation 2.53 can be integrated to obtain equation 2.54 (Turcotte and Schubert, 2002).

$$\frac{dv}{dy} = 0 \qquad (2.52)$$

$$\rho_f c_{p_f} v \frac{dT}{dy} = \lambda_m \frac{d^2T}{dy^2} \qquad (2.53)$$

$$\rho_f c_{p_f} v\, T = \lambda_m \frac{dT}{dy} + c_1 \qquad (2.54)$$

c_1 is the constant of integration and can be determined from the uniform ambient sediment temperature T_r conditions of the upwelling fluid at great depth. Hence as y approaches ∞, $\frac{dT}{dy}$ and T becomes 0 and T_r respectively. Thus equation 2.54 becomes 2.55 and 2.56. Also equation 2.56 can be rearranged and integrated to give equation 2.57 and 2.58 or 2.59 respectively.

$$c_1 = \rho_f c_{p_f} v \, T_r \tag{2.55}$$

$$\rho_f c_{p_f} v \, (T - T_r) = \lambda_m \frac{d}{dy}(T - T_r) \tag{2.56}$$

$$\frac{d(T - T_r)}{(T - T_r)} = \frac{\rho_f c_{p_f} v}{\lambda_m} \, dy \tag{2.57}$$

$$In \, \frac{T - T_r}{c_2} = \frac{\rho_f c_{p_f} v}{\lambda_m} \, y \tag{2.58}$$

Or

$$T - T_r = c_2 exp\left(\frac{\rho_f c_{p_f} v}{\lambda_m} \, y\right) \tag{2.59}$$

As y approaches ∞, the right hand side of equation 2.59 approaches zero because v is negative for vertical up-flow. At the surface with $y = 0$ and $T = T_0$, the integration constant c_2 can be evaluated as equation 2.60 and thus, the temperature depth function is expressed as equation 2.61 (Turcotte and Schubert, 2002).

$$c_2 = T_0 - T_r \tag{2.60}$$

$$T = T_r - (T_r - T_0) \, exp\left(\frac{\rho_f c_{p_f} v}{\lambda_m} \, y\right) \tag{2.61}$$

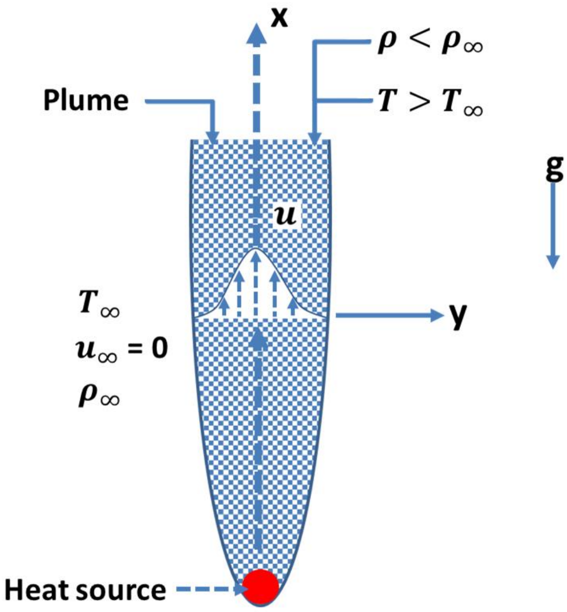

Figure 2.9: 2D plume of rising heated buoyant pore fluid in the vicinity of the heat source (line source). The increased width of the plume away from the heat source eventually dissipates due to viscous effects and the buoyancy force reduction caused by cooling of the fluid in the plume.

Buoyancy forces are due to small density decrease that occurs upon heating (Gebhart, 1979) (equation 2.62). Thus, If the flow is driven by the buoyancy of the hot water, Darcy velocity can be used to estimate the permeability of the system.

$$\rho_f = \rho_{f_0} - \alpha_f \rho_{f_0} (T_r - T_0) \qquad (2.62)$$

Where, $\rho_{f_0}$is the water density at temperature T_0 and α_f is the water thermal expansion volume coefficient. Thus substituting equation 2.62 into Darcy's law (Equation 2.49), give Equation 2.63. Also assuming for the upwelling flow the hydrostatic value is negligible in relation to an excess pressure gradient, equation 2.63 can then be used as equation 2.64. Thus, demonstrating that buoyancy of heated fluid can easily drive flow (Gebhart, 1979, Jaluria, 1980, Turcotte and Schubert, 2002).

$$v = -\frac{k}{\mu}\left(\frac{dp}{dy} - \rho_{f_0} g\right) - \frac{k}{\mu}\alpha_f \rho_{f_0} g (T_r - T_0) \qquad (2.63)$$

$$v = -\frac{k}{\mu}\alpha_f \rho_{f_0} g (T_r - T_0) \qquad (2.64)$$

2.3.4 Two Dimensional Heat Convection

A two dimensional approach can be used to describe the complete thermal circulation pattern for convection in a fluid saturated sediment heated from below and contained between impermeable isothermal boundaries (Turcotte and Schubert, 2002). The upper boundary, y=0, is maintained at temperature T_0, and the lower boundary, y = b, at temperature T_1 $(T_1 > T_0)$. Before convection can start, a critical temperature gradient across the layer must be exceeded. The conduction solution (equation 2.65), describe the temperature distribution before the onset of convection. The temperature difference $(T' \equiv T - T_c)$ and Darcy's velocity components u', v' at the onset of convection (when motion first takes place) is infinitesimal. Assuming the Boussinesq approximation and incompressible fluid with exception of Darcy's law buoyancy term for the vertical Darcy velocity component, the energy equation 2.51 is expressed as equation 2.66, in terms of T' (Turcotte and Schubert, 2002).

$$T_c = T_0 + \left(\frac{T_1 - T_0}{b}\right) y \qquad (2.65)$$

$$\rho_m c_{p_m} \frac{\partial T'}{\partial t} + \rho_f c_{p_f} \left(u' \frac{\partial T'}{\partial x} + v' \frac{\partial T'}{\partial y}\right) + \rho_f c_{p_f} v' \frac{(T_1 - T_0)}{b} = \lambda_m \left(\frac{\partial^2 T'}{\partial x^2} + \frac{\partial^2 T'}{\partial y^2}\right) \qquad (2.66)$$

The nonlinear terms $u' \frac{\partial T'}{\partial x}$ and $v' \frac{\partial T'}{\partial y}$ (left hand side) of equation 2.66 can be disregarded as T', u', and v' are infinitesimal quantities. Thus, for minor perturbations of temperature T', velocity u', v' and pressure p', the appropriate forms of equations 2.48, 2.49, 2.50 and 2.66 can be expressed as 2.67, 2.68, 2.69 and 2.70 respectively. As the sediment layer boundaries are isothermal and impermeable, equations 2.67 to 2.70 must be solved subject to the boundary conditions $v' = T' = 0$ at $y = 0$.

$$u' = -\frac{k}{\mu} \frac{dp'}{dx} \qquad (2.67)$$

$$v' = -\frac{k}{\mu} \left(\frac{dp'}{dy} - \alpha_f \rho_f g T'\right) \qquad (2.68)$$

$$\frac{\partial u'}{\partial x} + \frac{\partial v'}{\partial y} = 0 \qquad (2.69)$$

$$\rho_m c_{p_m} \frac{\partial T'}{\partial t} + \rho_f c_{p_f} v' \frac{(T_1 - T_0)}{b} = \lambda_m \left(\frac{\partial^2 T'}{\partial x^2} + \frac{\partial^2 T'}{\partial y^2}\right) \qquad (2.70)$$

For the onset of convection, the critical condition can be derived by setting $\frac{\partial}{\partial t} = 0$. Hence equation 2.70 becomes equation 2.71. The pressure perturbation in equations 2.67 and 2.68 can be removed by differentiating and subtracting Equation (2.67) with respect to y and Equation (2.68) with respect to x, to obtain equation

2.72. Also u' can be removed from equations 2.69 and 2.71 by similarly cross differentiation and subtraction procedure to obtain equation 2.73. Then a single equation (2.74) for T' can be obtained by solving Equation 2.71 for v' and substituting into equation 2.73 (Turcotte and Schubert, 2002).

$$\rho_f c_{p_f} v' \frac{(T_1 - T_0)}{b} = \lambda_m \left(\frac{\partial^2 T'}{\partial x^2} + \frac{\partial^2 T'}{\partial y^2} \right) \tag{2.71}$$

$$\frac{\partial u'}{\partial y} - \frac{\partial v'}{\partial x} = \frac{k \alpha_f \rho_f g}{\mu} \frac{\partial T'}{\partial x} \tag{2.72}$$

$$\frac{\partial^2 v'}{\partial x^2} + \frac{\partial^2 v'}{\partial y^2} = \frac{-k \alpha_f \rho_f g}{\mu} \frac{\partial^2 T'}{\partial x^2} \tag{2.73}$$

$$\frac{\partial^4 T'}{\partial x^4} + 2 \frac{\partial^4 T'}{\partial x^2 \partial y^2} + \frac{\partial^4 T'}{\partial y^4} = \frac{-k \alpha_f \rho^2{}_f g c_{p_f} (T_1 - T_0)}{\mu \, \lambda_m b} \frac{\partial^2 T'}{\partial x^2} \tag{2.74}$$

The boundary conditions must also be expressed in regards to T' because $T' = 0$ on y = 0, b, $\frac{\partial^2 T'}{\partial x^2} = 0$, on the boundaries. $v' = 0$ and $\frac{\partial^2 T'}{\partial x^2} = 0$, on y = 0, b, Equations 2.66 generates $\frac{\partial^2 T'}{\partial y^2} = 0$, on the boundaries. Thus for the fourth order differential equation, the complete set of boundary conditions for T' is $T' = \frac{\partial^2 T'}{\partial y^2} = 0$, on y = 0, b. To satisfy both differential equation and the boundary conditions, the elementary solution for T' is given by equation 2.75, where ${T_0}'$ is the temperature perturbation amplitude and γ is its wavelength, which can be obtained (equation 2.76) by substituting Equation 2.75 into equation 2.74. Thus, right hand side of equation 2.76 generates a dimensionless combination of parameters (equation 2.77) known as the Rayleigh number (Ra) for heat convection in a water saturated sediment layer heated from below (Turcotte and Schubert, 2002). The critical Rayleigh number (lowest value, equation 2.79) for the onset of convection in terms of wavelength value can be derived by differentiating equation 2.77 (left hand side) with respect to $\frac{2\pi b}{\gamma}$, equating the result to zero (2.78) and then substituting it into the left hand side of equation 2.77.

$$T' = T_0' \sin\frac{\pi y}{b} \sin\frac{2\pi x}{\gamma} \tag{2.75}$$

$$\frac{\left\{\left(\frac{2\pi b}{\gamma}\right)^2 + \pi^2\right\}^2}{\left(\frac{2\pi b}{\gamma}\right)^2} = \frac{\alpha_f g {\rho^2}_f c_{p_f} k b (T_1 - T_0)}{\mu \, \lambda_m} \tag{2.76}$$

$$Ra \equiv \frac{\alpha_f g {\rho^2}_f c_{p_f} k b (T_1 - T_0)}{\mu \, \lambda_m} \tag{2.77}$$

$$\gamma = 2b \tag{2.78}$$

$$\min(Ra_{cr}) = 4\pi^2 = 39.4784 \tag{2.79}$$

2.3.5 Summary

Thus, from Equation 2.77 the expectation of the occurrence of convection when Ra exceed Ra_{cr} can be summarised in many ways. If other quantities remains fixed, increasing the surface temperature of HV cable (buried heat source), increases the temperature difference $(T_1 - T_0)$ across the surrounding sediment pore fluid layer beyond a certain minimum value or decreases the viscosity of the fluid below a critical value before the onset of convection. Also the analysis for the onset of convection can be examined for a fluid layer heated uniformly from within and cooled from above (and assumed to be insulating with no heat flow across the boundary). The fluid nearer the upper boundary is cooler and more dense than the heated fluid beneath. Thus, buoyancy forces can drive convective fluid motion provided they are strong enough to overcome the viscous resistance. Furthermore, from Equation 2.77, the permeability (k) of the surrounding sediment is also a key controlling factor for the onset of convection heat transfer through the sediments around a buried heat source (HV cable), as it controls the ease of fluid flow. Thus, heat convection could occur within a high permeability sediment around a relatively lower heat source temperature (temperature difference $(T_1 - T_0)$) as compared to within a surrounding sediment with a low permeability that will require a relatively higher heat source temperature.

2.4 Synthesis of Previous Thermal Properties Measurements

Heat propagation in sediments is regulated by linked key thermal properties (Harrison and Phizacklea, 1987b, Harrison and Phizacklea, 1987a) namely, volumetric heat capacity, thermal diffusivity and thermal conductivity. Thus this sub-section aims to review and synthesise previously published near surface marine sediments thermal properties measurements methods and results to gain a better understanding of these properties, their variability with varying sediments and pore fluid properties.

2.4.1 Thermal Conductivity, λ

The thermal conductivity determines where and how much heat flows in response to temperature differences in the sediment. The unit of thermal conductivity is $Wm^{-1}K^{-1}$. Steady-state and transient methods are both used to measure thermal conductivity of sediments. The steady-state method (divided-bar, Figure 2.10) is the long-time standard for measuring thermal conductivity; by placing a disk-shaped sample of material between two cylindrical metal bars held at constant temperature. After a steady state is reached, the sample’s thermal conductivity is estimated by comparing the temperature drop across its faces with the drop across those of reference materials of known conductivity flanking the sample (Ratcliffe, 1960, Chekhonin *et al.*, 2012).

The divided bar method defines the standard for accuracy in measuring thermal conductivity, but is time-consuming and hence not suitable for in-situ measurements. In addition, the process is time consuming, involving cutting, trimming and polishing the disk to ensure good thermal contact with the heating bars. This last step is difficult to complete with fractured and unconsolidated sediments (Beck, 1957, Pribnow and Sass, 1995, Chekhonin *et al.*, 2012). Also to estimate the in-situ temperature and pressure conditions, the thermal conductivity measurements in the laboratory must be corrected accordingly (Ratcliffe, 1960).

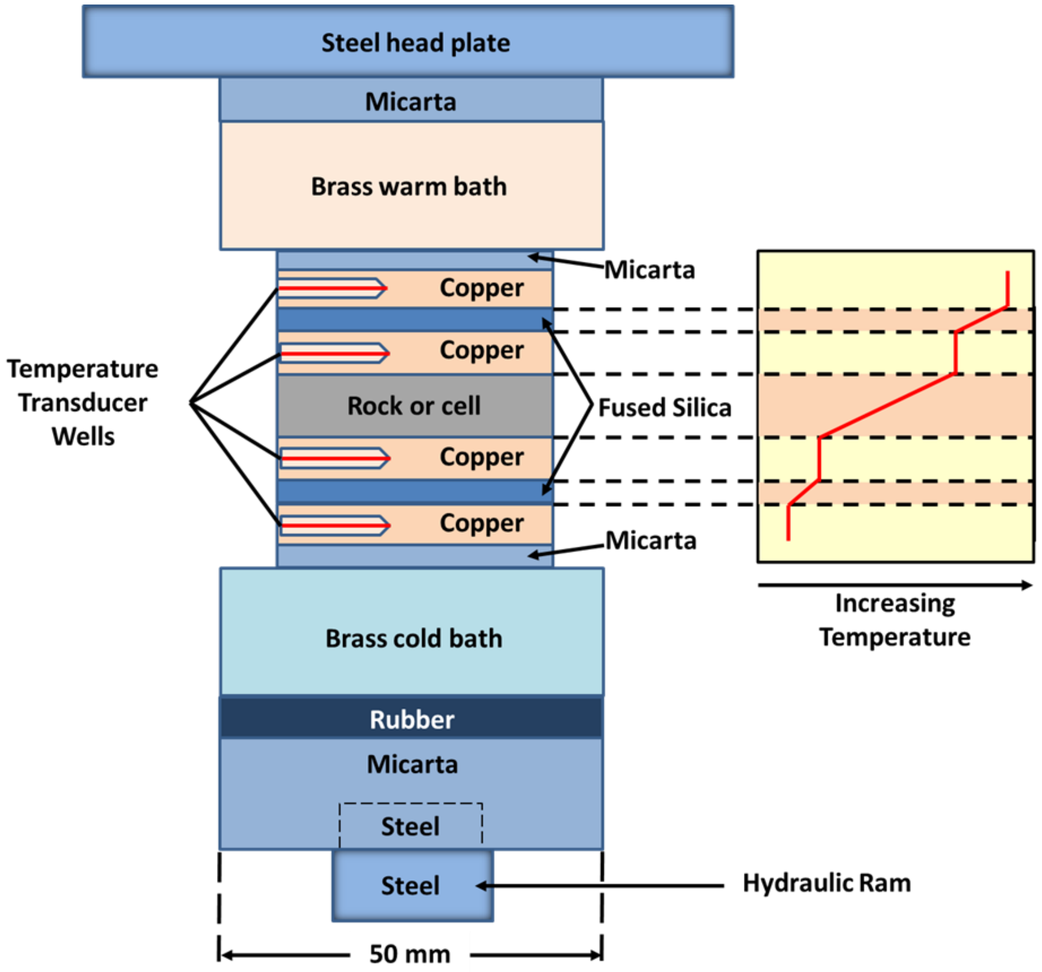

Figure 2.10: Schematic diagram of the divided bar method for measuring sediment thermal conductivity. The method sandwiches a disk-shaped sediment sample between brass plates over the two ends of a divided bar, which are held at different temperatures. The sample is flanked by disks of a reference material of known thermal conductivity (fused silica is a commonly used reference with a thermal conductivity of 1.38 $Wm^{-1}K^{-1}$). After a steady state is reached, as indicated by steady temperatures in the transducer wells, the sample's thermal conductivity is determined by comparing the temperature drop across its length with the drop across the reference material, adapted from (Chekhonin *et al.*, 2012).

Another method of measuring thermal conductivity is the constant heating or transient method. Von Herzen and Maxwell (Von Herzen and Maxwell, 1959) carried out thermal conductivity measurement of a deep-sea sediment contained in a tube 6.4cm long of a hypodermic needle enclosing a single loop of heating wire and a temperature sensing thermistor placed at the middle of the needle. At a constant applied heat, the slope of the temperature rise (T) of the probe inserted into the sediment is inversely related to the sediment thermal conductivity. Von Herzen and Maxwell (Von Herzen and Maxwell, 1959) estimated the thermal conductivity from the slope of the plot of T versus $In\,(\mathrm{t})$, for time 10 seconds to 10 minutes, using equation 2.80.

$$T = \frac{q}{4\lambda\pi}\left(In\frac{4\alpha t}{Ba^2}\right) \qquad (2.80)$$

Where T is needle probe temperature rise, q is the heat input per unit length per unit time t, λ and α are the thermal conductivity and diffusivity respectively, a is the probe radius and B is an empirical value of 1.7811 specific for deep sea clay.

Von Herzen and Maxwell (Von Herzen and Maxwell, 1959) demonstrated that for deep-sea clay sediments, the results of sediment thermal conductivity computation using both the needle and steady-state methods are within the error limit of each respective method of about 3 to 4%. The constant heating probe technique is more quickly carried out and conveniently used on board ship as well as can be adapted for simultaneous in-situ measurement of thermal conductivity and temperature gradient on the ocean floor. Particularly for material at very shallow depths below the seafloor, this approach largely remove the problems and uncertainties involved in raising a sediment sample to the surface as well as the need to correct lab based measurements to in-situ temperature and pressure conditions (Von Herzen and Maxwell, 1959, Ratcliffe, 1960).

The heat-pulse method is another extensively used transient method for measuring λ of sediment (Hartmann and Villinger, 2002, Hyndman *et al.*, 1979, Lister, 1979). It involves the use of a geothermal probe of approximately up to 4.5m (Goto *et al.*, 2012) long (Figure 2.11), with several temperature sensors that penetrate into the sediment (Jaeger, 1958, Von Herzen and Maxwell, 1959, Waite *et al.*, 2006, Woodside and Messmer, 1961a, Woodside and Messmer, 1961b, Ratcliffe, 1960), depending on the target of investigation. This method is based on temporal decay of the temperature of a cylinder inserted in sediment after impulse heating of the probe cylinder (Carslaw and Jaeger, 1959). The heat-pulse method uses a temperature sensor and a heating wire contained within a cylinder, which is similar to the previous method (Von Herzen and Maxwell, 1959); however, it requires less electric power for heating than the continuous heating method. Hence, it is more appropriate for in-situ thermal conductivity measurements of sediment on the seabed. It has also been used by numerous researchers to jointly measure in-situ sediment thermal conductivity along with the geothermal gradient (Goto *et al.*, 2012, Goto and Matsubayashi, 2009, Goto and Matsubayashi, 2008, Becker *et al.*, 1996, Harris *et al.*, 2010). However, the thermal probe methods may not return pure conductivity and this is key limitation. If the heat transfer through the sediment is convective, the thermal probe measurements will be the “equivalent thermal conductivity” not the actual thermal conductivity, as there will be heat transfer by convection as well.

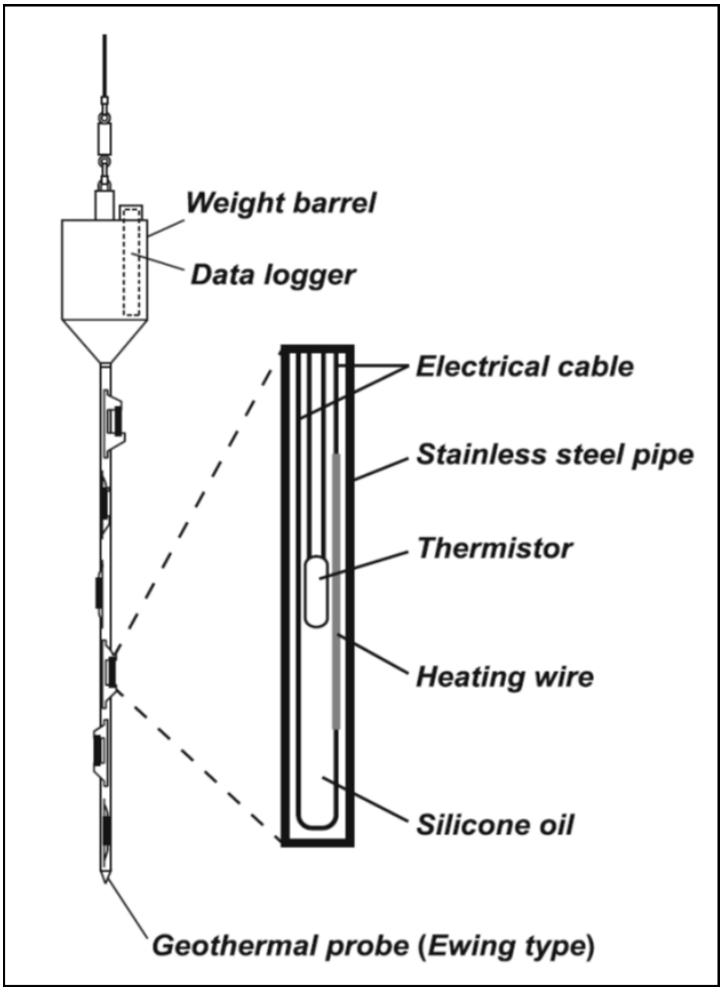

Figure 2.11: Schematic diagram of the heat-pulse method probe, from (Goto *et al.*, 2012).

2.4.2 Thermal Diffusivity, α

Thermal diffusivity determines the speed at which a temperature front propagates though sediments, with units of m^2s^{-1}. Harrison (Harrison, 1985) used the first harmonic amplitude (24h) to calculate α by applying simple harmonic analysis (Carson, 1963, Greenland, 1969) on Chichester Harbour time series data to derive a 24-h sinusoidal temperature wave form (equation 2.81). This uses Fourier decomposition and the form of the equation for which the longest period is the one which dominates at depth. Hence calculation of α may be based on linear change in phase or exponential change in amplitude with depth; because field soils diurnal temperature waves exhibit changing phase and amplitude with depth, reflecting the nature of heat flow. This approach (equation 2.81) has been used regularly by researchers (Harrison and Phizacklea, 1985, Vugts and Zimmerman, 1985, Piccolo *et al.*, 1993) to determine α (Tables 2.1, 2.2 and 2.3).

$$\alpha = \frac{\pi(Z_1 - Z_2)^2}{P\,[In\,(A_1/A_2)]^2} \qquad (2.81)$$

Where P is the period of wave oscillation (86400 s), Z_1 and Z_2 are the depths (m) between which diffusivity is to be calculated, A_1 and A_2 are amplitudes of the sediment temperature sinusoidal waves at depths Z_1 and Z_2

Due to its simplicity, equation (2.81) has been used regularly for tidal flat sediments to calculate α under the assumption that in situ temperature varies as a sinusoidal function of time. However, in situ temperature does not vary sinusoidally as they assumed but changes in a more complex way determined by the combination of tidal flat exposure time duration, time of day, solar radiation (Harrison and Morrison, 1993, Cho *et al.*, 2005). It also depends on the depth of investigation as Equation 2.58, shows that the shorter periods drop more rapidly with depth.

Alternatively, sediment thermal diffusivity can be calculated from observed sediment temperatures using the one-dimensional heat conduction equation (2.82) of Horton *et al*. (Horton *et al.*, 1983) This approach has also been used regularly by researchers (Harrison, 1985, Harrison and Phizacklea, 1985, Vugts and Zimmerman, 1985, Piccolo *et al.*, 1993, Kim *et al.*, 2007, Thomson, 2010) with similar results (Tables 2.1, 2.2 and 2.3).

$$\frac{\partial T}{\partial t} = \alpha \frac{\partial^2 T}{\partial Z^2} \qquad (2.82)$$

Where, T is sediment temperature in a layer with thickness Z. The thermal diffusivities α are estimated as the slope of the fitted lines from the graph of the temperature change with the time ($\frac{\partial \mathrm{T}}{\partial \mathrm{t}}$) and the second derivative of the sediment temperature profile ($\frac{\partial^2 \mathrm{T}}{\partial \mathrm{Z}^2}$).

2.4.3 Volumetric Heat Capacity, C_v

Volumetric heat capacity is the amount of heat needed to raise the temperature of a unit volume ($1\mathrm{m}^3$) of sediments and pore fluids, by one-degree Kelvin with units of J $\mathrm{m}^{-3}\mathrm{K}^{-1}$. The $\mathrm{C_v}$ of tidal flat sediment can be expressed as the weighted sum of the heat capacities of the soil constituents as given for terrestrial sediment by Campbell and Norman (Campbell, 1985, Campbell and Norman, 1998) (equation 2.83):

$$C_v = \rho_s C_s n + \rho_f C_f (1-n) \qquad (2.83)$$

Where ρ_s and ρ_f are density of solid and fluid respectively; $\mathrm{C_s}$ and $\mathrm{C_f}$ are specific heat capacity of solid and fluid respectively while n is the porosity of sediments. Many researchers (Ochsner *et al.*, 2001, Bristow, 1998, Abu-Hamdeh, 2003) have verified equation (2.83) with comparable results and were carried out mostly in intertidal environment (Tables 2.1, 2.1 and 2.3).

Use of equation (2.83) is vital as it can be used to calculate $\mathrm{C_v}$ from the physical properties of sediment (bulk density of sediment and volume fraction of solid and water), without information on the sediment temperature. This is useful as seawater and sediment temperature changes rapidly due to varying atmospheric conditions. It avoids the risk of temperature measurement errors propagating into the estimation of $\mathrm{C_v}$. The $\mathrm{C_v}$ can also be determined by the ratio of λ and α (equation 2.84).

$$C_v = \frac{\lambda}{\alpha} \tag{2.84}$$

2.4.4 Theoretical Models

Lovell (Lovell, 1985b, Lovell, 1985a) developed a model for computing thermal conductivity (equation 2.85) based on laboratory experimental results on the sediments thermal conductivity using a geometric combination of the thermal conductivity of water and solid (e.g. quartz mineral). Lovell (Lovell, 1985b, Lovell, 1985a) model result demonstrates that there are strong differences in thermal characteristics between water and solid minerals and other researchers (Jackson and Richardson, 2002, Rajan and Frisk, 1992) has successfully applied the model.

$$K = {\lambda_f}^{n} \ {\lambda_s}^{(1-n)} \tag{2.85}$$

Thomson (Thomson, 2010) combined the models of Lovell (Lovell, 1985b, Lovell, 1985a) for conductivity (equation 2.85) and Campbell and Norman (Campbell and Norman, 1998) for volumetric heat capacity (equation 2.83), to develop a novel theoretical model (equation 2.86) relating sediment porosity to thermal diffusivity.

$$\alpha = \frac{\lambda}{C_v} = \frac{{\lambda_f}^{n} + {\lambda_s}^{(1-n)} + 1}{\rho_f C_f n + \rho_s C_s (1-n)} \tag{2.86}$$

Where λ_s and λ_f are the conductivities of the solid and fluid constituents, respectively.

2.4.5 Summary

In conclusion, the synthesis of published results following the review carried out on the thermal properties of near surface marine sediments, particularly within shallow (0 to 1m) sub-seabed, shows that thermal diffusivity mean ranges (Tables 2.1, 2.2 and 2.3) are 0.22 to 0.34 x 10^{-6} m^2s^{-1} for clays, 0.39 to 0.55 x 10^{-6} m^2s^{-1} for mud and 0.55 to 1.31 x 10^{-6} m^2s^{-1} for sand. Similarly, the thermal conductivity mean ranges (Tables 2.1, 2.2 and 2.3) are 0.80 to 1.11 $Wm^{-1}K^{-1}$ for clays, 0.80 to 1.51 $Wm^{-1}K^{-1}$ for mud and 1.64 to 3.55 $Wm^{-1}K^{-1}$ for sand. Thus, these thermal properties in general, increases with changing lithology such as from clays to sands. Tables 2.1, 2.2 and 2.3 provides more details on the synthesis of thermal property measurements. Also the review and synthesis of the various published research results demonstrates that there is a relatively very little research on near surface marine sediment thermal properties measurements compared to other sediment physical properties. It is important to emphasise that most of the rather little previous thermal properties measurements in marine environment were mostly carried out in intertidal environments.

Table 2.1: Synthesis of previous published thermal properties measurements of near surface (top 1m) marine sandy sediment

S/N	Author	Study Location	Observ. Depth (cm)	Environment & Sediment Composition	Vol. Heat Capacity C_V, $(10^6\ J\ m^{-3}\ K^{-1})$	Thermal Diffusivity α, $(10^{-6}\ m^2\ S^{-1})$	Thermal Diffusivity α, Error Range $(10^{-6}\ m^2\ S^{-1})$	Thermal Conductivity K, $(W\ m^{-1}\ K^{-1})$	Thermal Conductivity K, Error Range $(W\ m^{-1}\ K^{-1})$
1	Van Der Hoeven (1974)	Dutch Wadden Sea, Mok Bay, Holand	0-30	Inter-tidal Sand	2.71^{L}	1.31^{b}	-	3.55^{k}	-
2	Jackson & Richardson (2002)	Off Fort Walton Beach, Florida, USA	0-70	Shallow-water Sand	2.73^{L}	1.2^{k}	$1.1\text{-}1.3^{k}$	3.28^{g}	$2.98\text{-}3.58^{g}$
3	Thomson (2010)	Willapa & Skagit flat, Washington, USA	0-40	Inter-tidal Sand	-	0.95^{h}	$0.86\text{-}1.04^{h}$	-	-
4	Vugts & Zimmerman (1985)	Dutch Wadden Sea, Mok Bay, Holand	0-30	Inter-tidal Very fine sand	2.93^{L}	1.06^{b}	$1.0\text{-}1.12^{b}$	3.11^{k}	$2.91\text{-}3.31^{k}$
5	Van Boxel (1986)	Dutch Wadden Sea, Mok Bay, Holand	0-30	Inter-tidal Very fine sand	-	1.02^{b}	-	-	-
6	Lovell (1985a)	Artificial Sand	–	Artificial Sand	2.93^{k}	0.99^{j}	$0.9\text{-}1.08^{j}$	2.9^{g}	$2.5\text{-}3.3^{g}$
7	White et al. (1984)	Table 8.2	0-30	Wet Sand:	2.96^{L}	0.74^{k}	-	2.2^{L}	-
8	Cyr (2012)	Lake Opeongo, Ontario, Canada	0-5	Shallow-water Sand: 96% Sand, 4% Mud	-	0.55^{a}	$0.5\text{-}0.6^{a}$	-	-
9	Harrison & Morrison (1993)	Patara Beach, Turkey	0-10	Inter-tidal Fine Sand	2.95^{L}	0.61^{b}	-	1.8^{k}	-
10	Jackson & Richardson (2002)	Off Fort Walton Beach, Florida, USA	0-70	Shallow-water Sand	2.73^{L}	0.6^{a}	$0.54\text{-}0.66^{a}$	1.64^{k}	$1.28\text{-}2.0^{k}$

Key:

[a] Calculated with Horton et al. 1993, 1D heat conduction using observed temperature in lab.

[b] Calculated with Horton et al. 1993, 1D heat conduction using in-situ temperature

[g] Calculated using Lovell 1985 model.

[h] Calculated using Thomson 2010 model.

[j] Calculated using Von Herzen and Maxwell 1959 empirical relation.

[k] Calculated using the two others thermal property parameters.

[L] Quoted in previous study

Table 2.2: Synthesis of previous published thermal properties measurements of near surface (top 1m) marine muddy sediment.

S/N	Author	Study Location	Observ. Depth (cm)	Environment & Sediment Composition	Vol. Heat Capacity C_V, (10^6 J m^{-3} K^{-1})	Thermal Diffusivity α, (10^{-6} m^2 S^{-1})	Thermal Diffusivity α, Error Range (10^{-6} m^2 S^{-1})	Thermal Conductivity K, (W m^{-1} K^{-1})	Thermal Conductivity K, Error Range (W m^{-1} K^{-1})
11	Harrison & Phizacklea (1987b)	Forth Estuary, Scotland	0-30	Inter-tidal Mud: 4% org. material, 16% sand, 80% silt & clay	-	0.812[b]	-	-	-
12	Kim et al. (2007)	Baeksu tidal flat, South-western Coast, Korea	0-40	Inter-tidal Mud: 7% sand, 67% silt, 26 % clay	2.96[f]	0.51[b]	0.43-0.59[b]	1.51[k]	1.23-1.79[k]
13	Guarini et al. (1997)	Marennes-Oleron Bay, France	0-1	Inter-tidal Mud	1.65[e]	0.48[k]	-	0.80[L]	-
14	Andrews (1980)	–	0-30	Inter-tidal Mud	-	0.48[L]	-	-	-
15	Harrison (1984a)	Forth Estuary, Scotland	0-10	Inter-tidal Mud	1.87[L]	0.47[a]	-	0.88[k]	-
16	Harrison & Phizacklea (1985)	Forth Estuary, Scotland	0-10	Inter-tidal Mud: 4% org. m., 16% sand, 80% silt & clay	1.87[k]	0.47[a]	-	0.88[c]	-
17	Harrison & Phizacklea (1987a)	Forth Estuary, Scotland	0-30	Inter-tidal Mud 4% org. m., 16% sand, 80% silt & clay	-	0.47[a]	0.4-0.54[a]	-	-
18	Thomson (2010)	Willapa & Skagit flat, Washington, USA	0-40	Inter-tidal Mud	-	0.55[h]	0.45-0.65[h]	-	-
19	Harrison (1985)	Chichester Harbour, England	0-26.5	Inter-tidal Mud	2[L]	0.41[b]	-	0.82[k]	-
20	Harrison (1981)	–	0-10	Inter-tidal Mud	-	0.41[L]	-	-	-
21	Piccolo et al. (1993)	Minas Basin, Bay of Fundy, Canada	0-10	Inter-tidal Mud: 51.9% silt, 35.7% sand,	-	0.41[b]	-	-	-
22	Heath (1977)	Pauatahanui Inlet, New Zealand	0-30	Inter-tidal Mud	2.15[L]	0.39[b]	-	0.84[k]	-

Key:

[a] Calculated with Horton et al. 1993, 1D heat conduction using observed temperature in lab.

[b] Calculated with Horton et al. 1993, 1D heat conduction using in-situ temperature

[c] Calculated using divided bar steady-state method in lab.

[e] Calculated using minimised sum of the between air-sediment interface heat flux and the quantity of heat change in the sediment during exposure.

[f] Calculated using Campbell and Norman 1998 relationship.

[h] Calculated using Thomson 2010 model.

[k] Calculated using the two others thermal property parameters.

[L] Quoted in previous study

Table 2.3: Synthesis of previous published thermal properties measurements of near surface (top 1m) marine clay sediment

S/N	Author	Study Location	Observ. Depth (cm)	Environment & Sediment Composition	Vol. Heat Capacity C_V, $(10^{6}\ J\ m^{-3}\ K^{-1})$	Thermal Diffusivity α, $(10^{-6}\ m^{2}\ S^{-1})$	Thermal Diffusivity α, Error Range $(10^{-6}\ m^{2}\ S^{-1})$	Thermal Conductivity K, $(W\ m^{-1}\ K^{-1})$	Thermal Conductivity K, Error Range $(W\ m^{-1}\ K^{-1})$
23	Lee & Von Herzen (1994)	Indian & Atlantic Ocean	Simu.	Deep-water Clay	3.39[k]	0.26[j]	0.23-0.28[j]	0.88[d]	0.82-0.95[d]
24	Lee et al. (2003)	Lake Baikal, Siberia	in-situ	Deep-water Clay	3.0[L]	0.33[k]	0.27-0.4[k]	1.0[d]	0.8-1.2[d]
25	Lovell (1985a)	Northeast Atlantic Ocean	Surficial Sample 0-3m	Deep-sea Clay	3.39[k]	0.28[j]	0.19-0.37[j]	0.95[g]	0.7-1.2[g]
26	Von Herzen & Maxwell (1959)	Southeast Pacific Ocean	Core (Lab) samples	Deep-water Clay	3.32[k]	0.25[i]	0.18-0.31[j]	0.83[d]	0.68-0.98[d]
27	Ratcliffe (1960)	Atlantic, Pacific & Mediterranean Ocean	Core (Lab) samples	Deep-water Clay	3.41[k]	0.27[j]	0.19-0.34[j]	0.92[c]	0.71-1.13[c]
28	Sclater et al. (1969)	Pacific Ocean	Core (Lab) samples	Deep-water Clay	3.27[k]	0.34[j]	0.33-0.35[j]	1.11[d]	1.08-1.14[d]
29	Rajan & Frisk (1992)	Gulf of Mexico	0-15m	Shallow-water Clay	3.64[k]	0.22[j]	-	0.8[L]	-
30	Sclater et al. (1969)	Pacific Ocean	in-situ	Deep-water Clay	3.30[k]	0.33[j]	0.31-0.35[j]	1.09[d]	1.05-1.13[d]
31	White et al. (1984)	Table 8.2	Samples	Dry Sand:	1.08[L]	0.28[k]	-	0.30[b]	-
32	Harrison & Phizackley (1987b)	Forth Estuary, Scotland	0-30	Inter-tidal Dry Sand	-	0.246[b]	-	-	-

Key:

[b] Calculated with Horton et al. 1993, 1D heat conduction using in-situ temperature

[c] Calculated using divided bar steady-state method in lab.

[d] Calculated using Needle-probe transient methods on ship board and lab.

[g] Calculated using Lovell 1985 model.

[j] Calculated using Von Herzen and Maxwell 1959 empirical relation.

[k] Calculated using the two others thermal property parameters.

[L] Quoted in previous study

Page intentionally left blank.

3

The Thermal Regime Around Buried Submarine High Voltage Cables

3.1 Introduction

[1]This chapter presents the first set of temperature measurements from a 2D laboratory experiment designed as an analogue to a buried submarine HV cable. A

---

[1] This chapter have been published as: Emeana, C.J., Hughes, T.J., Dix, J.K., Gernon, T.M., Henstock, T.J., Thompson, C.E.L. & Pilgrim, J.A., 2016. The thermal regime around buried submarine high voltage cables, *Geophysical Journal International,* 206**,** 1051 - 1064. doi:10.1093/gji/ggw195. Author list are reflective of relative contributions. Particularly, the Finite Element Method (FEM) model figures of the steady state heat flow regimes and corresponding figures presented in the GJI article as well as in this chapter were carried out by T.J. Hughes. The FEM figures were added to the GJI article following reviewers comments requesting the addition of numerical models to support the physical modelling results carried out by C.J. Emeana.

range of realistic cable surface temperatures were used to identify how the thermal regimes and heat transport mechanisms may vary with a range of typical shelf sediments. The observed results were compared with the predictions of numerical models and explored to understand some of the environmental implications.

3.2 Method Development

3.2.1 Experimental Set-up

Temperature time series data are measured using a 2D experimental tank (height: 2.5 m, width: 2.0 m and thickness: 0.11 m, Figure 3.1a) filled with prototype scale, tap water saturated, sediments and with an inserted heat source (Figure 3.1b), designed as a proxy to a buried sub-seafloor HV cable. The heat source is capable of generating cable surface temperatures up to 100°C. This approach is adapted from analogue experiments involving gas-particle fluidization in volcanic systems (Gernon *et al.*, 2008). The tank is constructed from 2 cm thick Perspex, reinforced with steel bars (Figure 3.1a). The vicat softening temperature, coefficient of thermal expansion and thermal conductivity of the Perspex are 110 °C, 7×10^{-5} K^{-1}, and 0.2 Wm^{-1} K^{-1}, respectively. The tank is open at the top and has integrated outlets at the base to allow in-fill and removal of sediments and water. Three layers of 10 cm thick Celotex™ TA4000 insulation sheets are directly attached to the external sides of the tank to limit heat loss through the Perspex sides. Each of the attached insulation sheets has a thermal conductivity of 0.022 Wm^{-1} K^{-1} and low emissivity aluminium foil facings on both sides, providing high performance insulation (Celotex, 2013).

The heat source was constructed using an INC800 heating element (Length: 2.44m and Loading Watt: 2000) that is tightly coiled inside a drilled cavity in the middle of a cylindrical aluminium block (radius: 0.11 m and thickness: 0.10 m), providing a good thermal contact. A variable autotransformer (variac) and voltage stabilizer are used to provide a controlled heat input and stabilise the fluctuating mains output. Water ingress into the cavity of the heat source is prevented using two tightly sealed aluminium side coverings. During the design phase modelling of the heat source (Hughes *et al.*, 2015) ensured an isothermal outer surface could be produced. Subsequently, a number of initial measurements on the heat source were conducted to assess its operation, and to test the predicted isothermal outer surface. Six K6-type thermocouples (hereafter referred to as TCs) were attached equidistantly around the surface of the heat source. The TCs have a solid diameter of 0.376mm and an operating temperature range of -75°C to 250°C, a quoted accuracy of ± 1.5°C and a precision of ± 0.25% (equivalent to ± 0.1-0.3 °C over the measured temperature range). Each welded ‘single shot’ tip of the TCs are at the termination point of 5 m long PTFE, water tight, insulated cables. During a pilot study, the heat source was inserted in a small tank filled with a mixture of sediments and water. Measurements from the attached 6 TCs gave surface temperatures at three time steps (0.7, 2.8 and 4.9 days respectively) of 29.7 ±0.1 °C, 38.6 ±0.1 °C and 48.2 ±0.2 °C respectively. The low standard deviation of these measurements (within the quoted precision of the TCs) supports the isothermal heat distribution predicted from the initial modelling.

Temperatures within the tank are measured using 120 of the K6-type TCs attached to nodes on a pre-constructed mesh. The TC grid varied between a nodal spacing of 10 cm and 20 cm with the higher density grid immediately adjacent to the heat source and the central section of the tank (Figure 3.1c). After installation of the TCs inside the experimental tank, and prior to adding the sediment, high resolution digital imagery of the TCs along with multiple scales has been taken and the images rectified to locate each TC to an accuracy of 1 mm. Temperature time series measurements are recorded at 60 second intervals on a Campbell Scientific CR1000 measurement control system, with a fixed measurement range of -44 to 80°C for all experiments. The temperature time series data were filtered using a moving average filter with a span of 5 minutes to smooth the remnant variation in the temperature data due to the fluctuating mains output. The TCs are distributed throughout the tank (Figure 3.1c) to measure the surface temperature of the heat source (1 TC), the temperature distribution within the sediment (113 TCs), the water column at the top of the tank (3 TCs) and the ambient air temperature throughout each experiment (3 TCs externally located at the top and bottom of the tank and on the outermost insulation sheet).

For the experiments presented in this chapter, the tank is filled with a mixture of water (undistilled) and ballotini, a synthetic sediment composed of spherical Soda-lime glass beads material made up of 72.0% silicon dioxide (SiO_2), 13.5% sodium oxide (Na_2O), 9.0% calcium oxide (lime, CaO), 3.4% magnesium oxide (MgO), 2.0% aluminium oxide (Al_2O_3) and 0.1% iron oxide (Fe_2O_3) minerals (Potters-Ballotini, 2011). Also the physical characteristics of ballotini are: 2.5 specific gravity, 1172 $JKg^{-1}K^{-1}$ specific heat capacity and 0.94 $Wm^{-1}K^{-1}$ thermal conductivity (Potters-Ballotini, 2011) and measurements from various near surface marine environments with high porosity sediments, demonstrated that thermal conductivity of approximately 1 $Wm^{-1}K^{-1}$ is quite representative for such environments (Woodside and Messmer, 1961c, Beck, 1976, Lovell, 1985b, Lovell, 1985a). Thus, ballotini was chosen to ensure uniform composition and size of the grains, and provides greater control of the porosity and permeability as well as enables application of the laboratory experiment results to the natural thermal regimes experienced by submarine HV cables buried within near surface shelf sediments.

Three different pre-sieved, very well sorted, symmetric and mesokurtic samples of ballotini were used. Table 3.1 shows the measured mean grain sizes ($\boldsymbol{d_m}$) 0.045mm (Coarse Silt), 0.20mm (Fine Sand) and 1.23mm (Very Coarse Sand) of the three size classes and the results are based on sieve analysis, graphical methods of Folk and Ward (Folk and Ward, 1957) in GRADISTAT version 8 (Blott and Pye, 2001) and the Udden-Wentworth grain-size scale for siliciclastic sediments (Wentworth, 1922). The mean and range of porosities (n) of the three samples are measured based on the gravimetric grain volume approach (Amyx *et al.*, 1960) and subsequently their permeabilities (k) are calculated using the Kozeny-Carman (Carman, 1937) equation (1). The porosity ($\boldsymbol{n}$) estimates are, Coarse Silt: 0.2 ± 0.05; Fine Sand: 0.32 ± 0.06 and Very Coarse Sand: 0.4 ± 0.05. Thus, the corresponding permeability ($\boldsymbol{k}$) estimates and the other measured physical properties of the three different pre-sieved size classes of ballotini are summarised in Table 3.1 and are consistent with typical estimates of shelf sediments (Bear, 1972, Van Brakel, 1975, Quiblier, 1984, Blair *et al.*, 1996, Turcotte and Schubert, 2002, Jackson and Richardson, 2007, Hughes *et al.*, 2015).

$$\mathrm{k} = \frac{1}{180}\frac{\mathrm{n}^3}{(1-\mathrm{n})^2}\mathrm{d}_\mathrm{m}^2 \qquad (3.1)$$

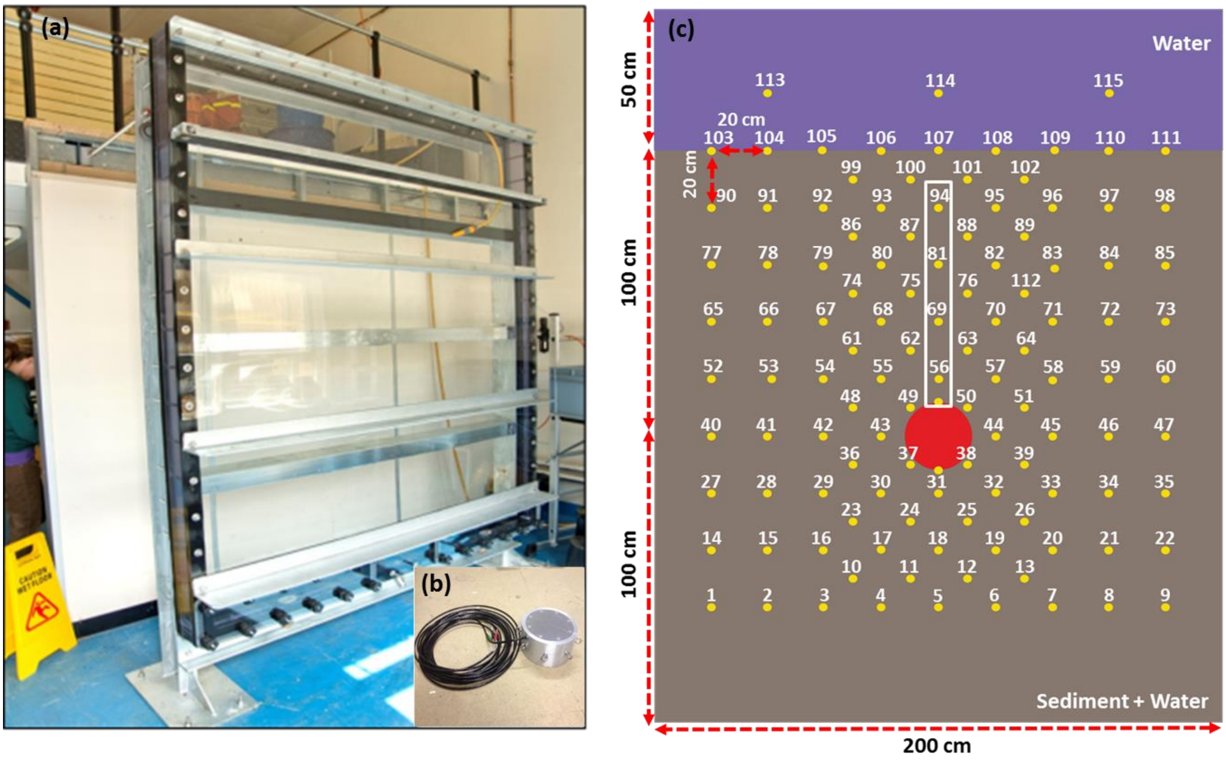

Figure 3.1: (a) Photograph of the 2D experimental tank, (b) aluminium heat source (22 cm diameter) and (c) a schematic diagram showing the TC grid locations. The temperature measurements from the TC attached on the heat source (TC 116) and those located vertically above it (inside the marked white box) were used to assess attainment of steady state temperature distribution of each experiment.

Table 3.1: Ballotini sediment properties for the three different size classes

Ballotini materials	Grain size range	Grain size, d_m (m)	Porosity range, n	Permeability range, k (m^2)
Low Permeability Class	Lower	32×10^{-6}	0.15	2.66×10^{-14}
	Mean	45×10^{-6}	0.2	1.41×10^{-13}
	Upper	58×10^{-6}	0.25	5.19×10^{-13}
Medium Permeability Class	Lower	150×10^{-6}	0.26	4.01×10^{-12}
	Mean	200×10^{-6}	0.32	1.57×10^{-11}
	Upper	250×10^{-6}	0.38	5.0×10^{-11}
High Permeability Class	Lower	1000×10^{-6}	0.35	5.64×10^{-10}
	Mean	1230×10^{-6}	0.4	1.49×10^{-09}
	Upper	1400×10^{-6}	0.45	3.28×10^{-09}

3.2.2 Achieving Steady State Thermal Distribution

For each experiment, we ensure that a steady state thermal distribution has been reached by calculating temperature change with time. Examples of this approach using the very coarse sand sample with a permeability of 1.49 x 10^{-9}m^2 are shown in Figure 3.2a and 3.2b for experiments with surface temperatures of 7^{o}C and 18^{o}C above ambient respectively. Figure 3.2 is based on the TC temperature measurements attached directly to the top of the heat source (TC116) and within the surrounding sediments; from the nearest (TC56 – 11.7cm from TC116) to the most distally heated TC located vertically above the heat source (TC94 – 69.9 cm from TC116). The experiments with surface temperature 7^{o}C and 18^{o}C above ambient, achieved steady state after 7200 (5 days) and 2448 minutes (1.7 days) respectively (Figure 3.2). Similar assessments were made for all experiments undertaken to ensure equilibrium had been achieved.

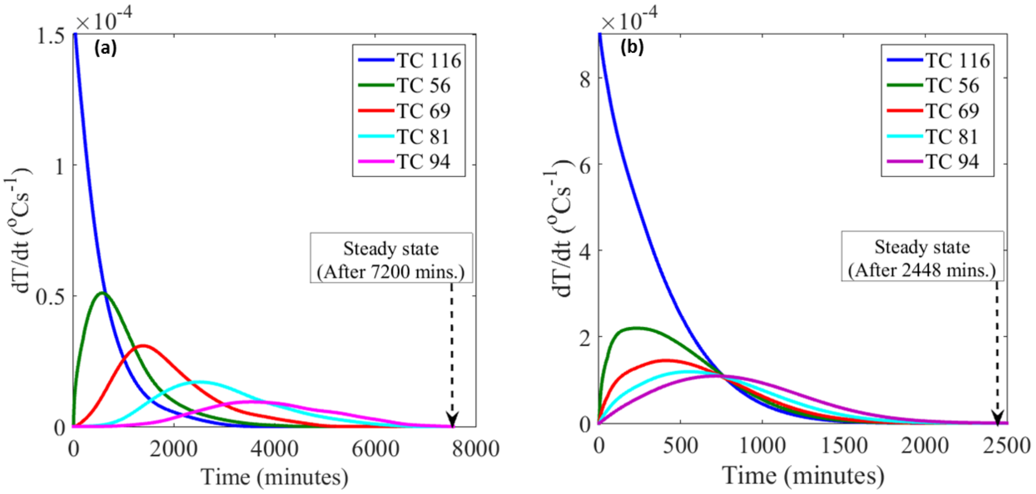

Figure 3.2: The rate of change in temperature (∂T/∂t) plot shows attainment of steady state at zero ∂T/∂t for the heat flow through the high permeability (10^{-9} m^2) very coarse sand sediment with temperatures of 7 ^{o}C (a) and 18 ^{o}C (b) above ambient.

3.2.3 Temperature Data Measurement Reproducibility

The reproducibility of the temperature time series data has been tested through two replicate experiments, A and B (Figure 3.3), using the fine sand sized sample at steady state. TC9 (i.e. bottom right hand corner of the tank) shows a temperature that is the most stable throughout the run (Figure 3.3a) with less change than either the ambient air temperature (TC119) or the temperature of the water above the sediment interface (TC114). With the same power input, the measured surface temperatures of the heat source (TC116) were 37.9^{o}C and 34.8^{o}C with ambient sediment temperature (TC9) of 19.3^{o}C and 16.0^{o}C respectively. The two experiments show the same pattern of temperatures (Figure 3.3b), but a 2.9 ± 0.4^{o}C mean difference from all sediment TCs at steady-state. When all temperatures are corrected to be relative to TC9, the mean offset between the two experiments is 0.4 ± 0.4^{o}C (Figure 3.3c). Consequently, we report all measurements as the temperature above ambient sediment temperature, as recorded at TC9 at the steady state time step. Comparing the temperature measurements at each time step of the two experiments from the 100 sediment TCs gives a high correlation coefficient (R^2) of 0.97 which is significant at the 95% confidence limit and with a T-statistic of 3.60 x 10^3 and P-value of zero (Figure 3.3d). The points on the scatter plot are coloured based on the density variation of the clustered points.

We also generated 2D time dependent heat flow surfaces based on linear interpolation of the neighbouring temperature distributions measured at each TC location for each replica experiment after correction (Figure 3.3e-3.3f). This further visually confirms reproducibility between experiments.

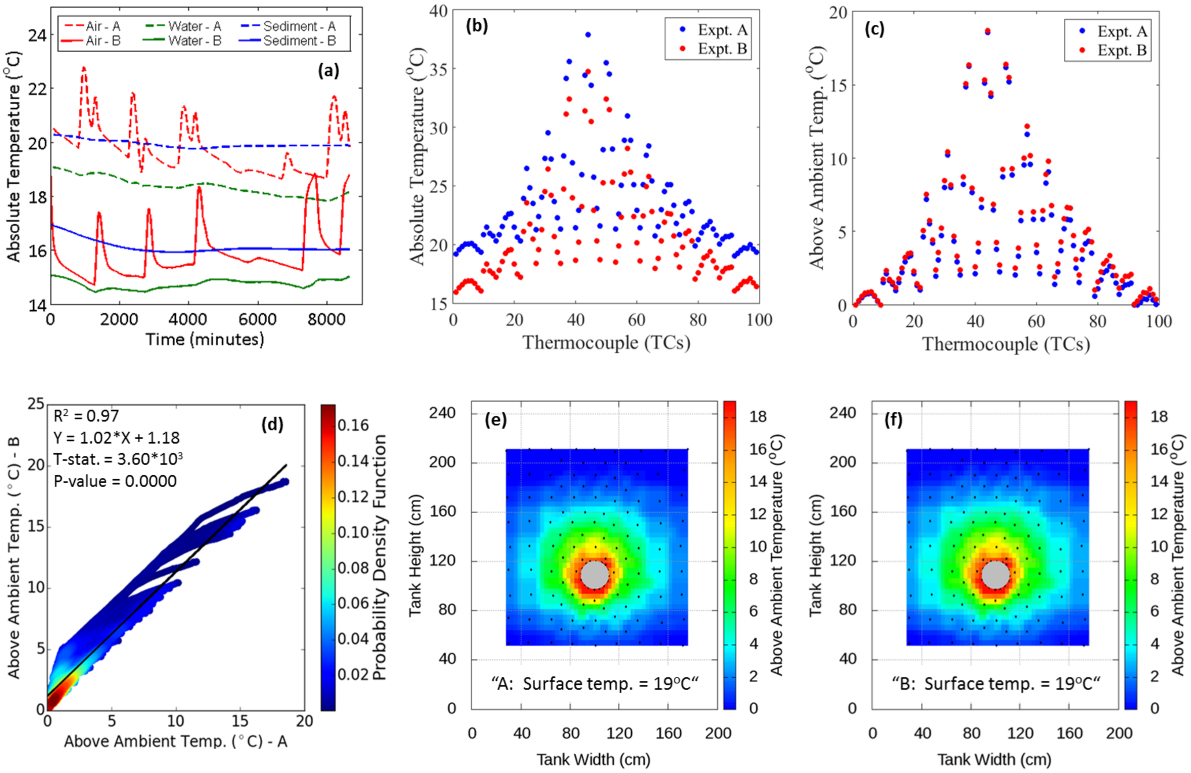

Figure 3.3: Assessment of the data measurement reproducibility using two replicate experiments A and B with steady state skin temperature (TC116) of 37.9 °C and 34.8 °C with ambient sediment temperature (TC9) of 19.3 °C and 16.0 °C respectively. Panel (a) represents the ambient air, water and sediment temperature; (b) and (c) are the steady state temperature distributions before and after correction respectively; (d) cross-plot of the 864000 temperature measurements from the two replicate experiments; and (e) and (f) are the steady state 2D heat flow surfaces after correction for the two replicate experiments with heat source surface temperature 19 °C above ambient.

3.3 Results

A total of fourteen heat flow experiments have been conducted to investigate the thermal regimes generated from typical cable surface temperatures within low, medium and high permeability sediments, to cover a range representative of the continental shelf. Normalised heat flow surfaces and radial temperature distributions were used to determine whether the heat transfer mode from a cable buried in such sediments is dominated by conduction or convection.

Finite Element Method (FEM) simulations have also been undertaken to model the steady state heat transfer within the tank experiment from the heat source flowing through the surrounding ballotini sediments. The construction of the model is based on the procedure described in Hughes et al. (2015), but has been modified to use the input parameters of the tank experiment. This included altering the model geometry to mimic the tank dimensions, and a constant temperature boundary condition being imposed at the surface of the simulated heat source. Thus, each heat flow experiment is compared with corresponding numerical simulation results using the same heat source surface temperatures and surrounding sediments properties of the low permeability mean class, medium permeability upper class and high permeability mean class (Table 3.1).

3.3.1 Thermal Regime at Low Permeability

The steady state temperature distributions within the low permeability sediment have been acquired from four experimental runs with heat source surface temperatures of 10, 18, 45 and 60°C above ambient. They all show radially symmetrical temperature distributions centred on the heat source, for surface temperatures of 10°C (Figure 3.4a) to 60°C (Figure 3.4c) above ambient measured at TC9. At the highest heat source temperature of 60°C (Figure 3.4c), there is a >10 °C temperature rise in the surrounding sediments up to 40 cm from the heat source.

Figure (3.4a’ to 3.4c’) shows the FEM model runs completed for each low permeability case with varying heat source temperature and further shows radially symmetrical temperature distributions centred on the heat source, for surface temperatures of 10°C (Figure 3.4a'), 18°C (Figure 3.4b') and 60°C (Figure 3.4c') above ambient. This heat flow pattern are highly comparable with the thermal regimes demonstrated with the lab experimental data (Figure 3.4a to 3.4c) within low permeability sediments. The heating effect to the surrounding sediment is also comparable for the lower heat source temperatures (Figure 3.4a and 3.4b), but as the temperature reaches 60°C (Figure 3.4c and 3.4c'), the disparity is due to remnant heat loss to the sides of the experimental tank after insulation. Thus for the numerical simulation result (Figure 3.4c'), at 60°C there is a >10 °C temperature rise in the surrounding sediments up to 60 cm from the heat source.

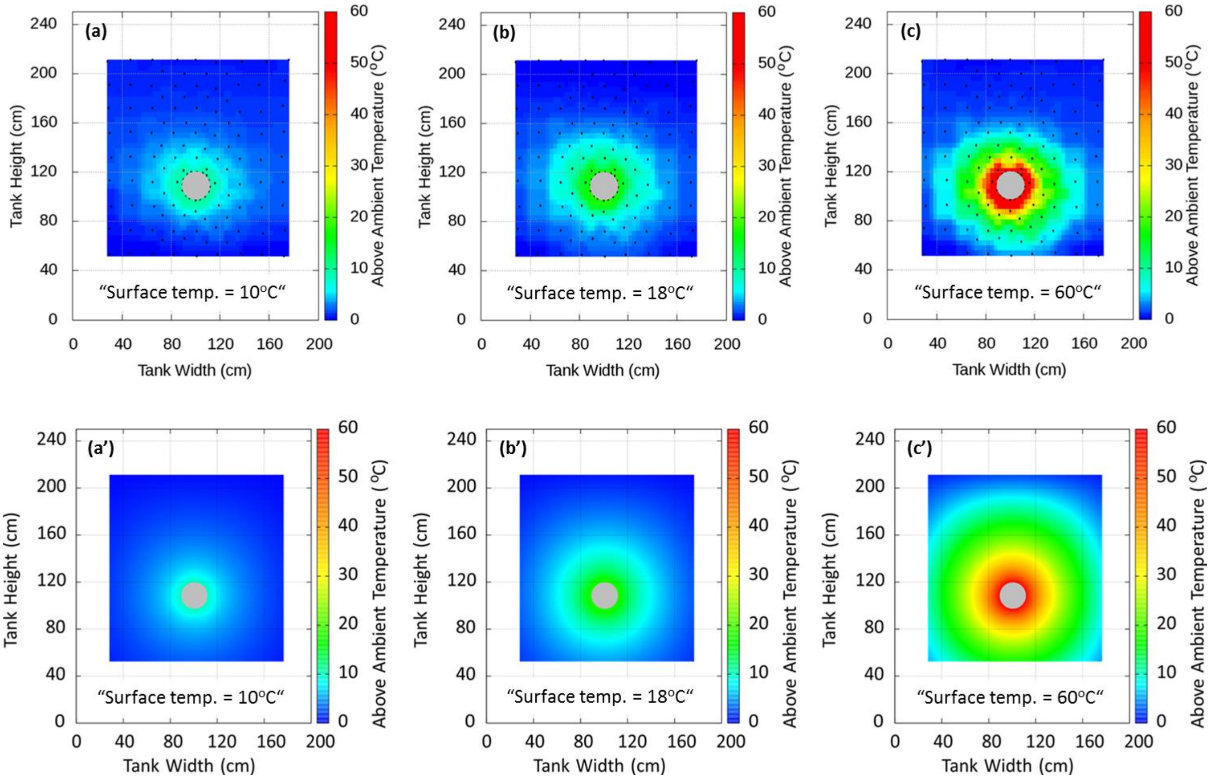

Figure 3.4: Steady state temperature distributions for low permeability (1.41 x 10^{-13} m^2) sediments with 10°C, 18 °C and 60 °C above ambient cable surface temperatures from the lab experiments (a, b and c) and corresponding numerical simulation results (a', b' and c').

3.3.2 Thermal Regime With Medium Permeability

The steady state temperature distributions within the medium permeability sediment from six experiments is driven by heat source surface temperatures of 10, 19, 36, 43, 51 and 55°C above ambient respectively. The temperature is centred on the heat source for skin temperatures of less than 10°C above ambient (Figure 3.5a), but is increasingly asymmetric as the skin temperature increases (Figures 3.5b-3.5d). At skin surface temperatures of >19°C there is a temperature increase >10°C at 40 cm radius from the heat source (Figure 3.5b); vertically above the heat source this 10°C increase reaches 100 cm at a heat source surface temperature of 55°C (Figure 3.5d). Also, at the highest heat source temperature (55°C – Figure 3.5d) the shallowest 20 cm of the sediment experiences an increase in temperature of up to 20°C over a zone about 60 cm wide.

Figure (3.5a’-3.5d’) shows the FEM simulations for the medium permeability case with varying heat source temperature. Again at 10°C (Figure 3.5a’), the modelled thermal regime shows radially symmetrical temperature distributions centred on the heat source, however as the temperature exceeds 19°C (Figure 3.5b’) an asymmetric heat flow pattern starts to develop and progresses with increasing heat source temperature (Figure 3.5b’-3.5d’); similar to the lab experimental results (Figure 3.5a-3.5d). The heating effect to the surrounding sediment is also comparable for lower and higher heat source temperatures (Figure 3.5a-3.5b) because with increasing source temperature, asymmetric vertically upwards heat flow pattern develops with negligible impact of the remnant heat loss to the sides of the experimental tank after insulation.

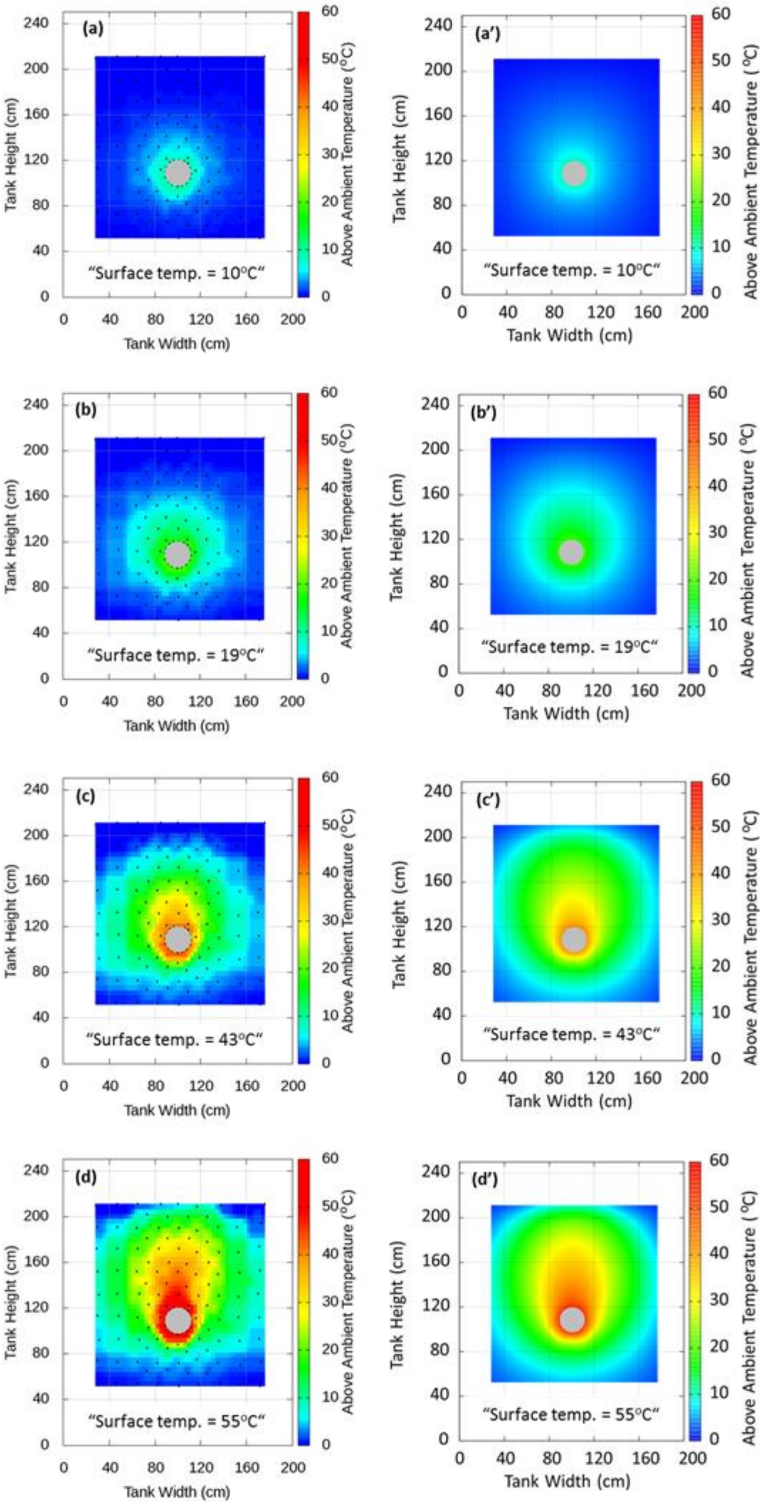

Figure 3.5: Steady state temperature distributions for medium permeability (5 x 10^{-11} m^2) sediments with 10°C, 19 °C, 43 °C and 55 °C above ambient cable surface temperatures from the lab experiments (a, b, c and d) and corresponding numerical simulation results (a', b', c' and d').

3.3.3 Thermal Regime At High Permeability

The steady state temperature distributions within the high permeability very coarse sand sediment are recorded for four experiments with heat source surface temperatures of 7, 9, 14 and 18^{o}C above ambient. They all show temperature distributions that are highly asymmetric, even at the lowest input surface temperature of 7^{o}C above ambient (Figure 3.6a). At these initial temperature inputs, the generated thermal plume has a width up to 140 cm for a 7^{o}C rise above ambient, narrowing to 100 cm, 80 cm and 60 cm as the heat source surface temperature is increased to 9, 14 and 18^{o}C above ambient respectively.

The FEM heat flow simulation results for the high permeability case (Figure 3.6a’ to 3.6c’) are also comparable with the lab experimental results, as all the thermal regimes demonstrate highly asymmetric patterns even at the lowest heat source temperature run of 7^{o}C above ambient (Figure 3.6a’). The heating effect of the vertical heat plume to the surrounding sediments are relatively broader for the observed results (Figure 3.6a to 3.6c), due to remnant heat loss to the sides of the experimental tank after insulation.

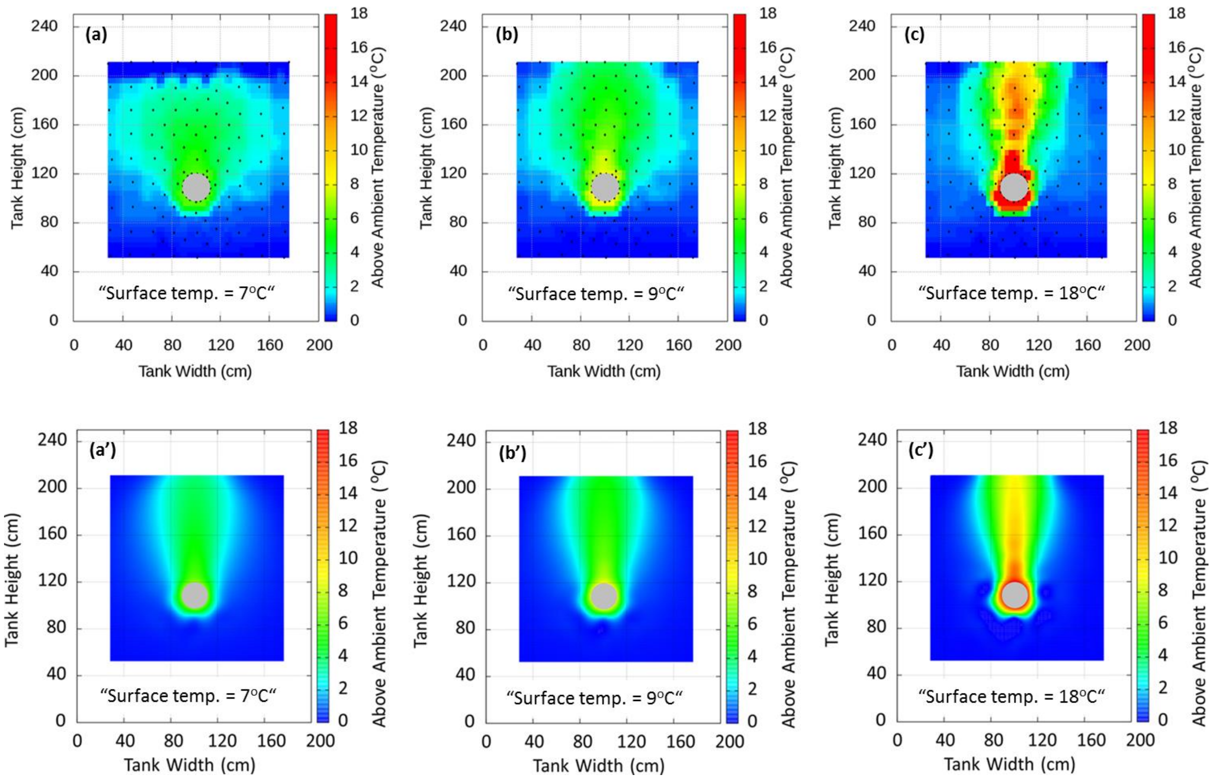

Figure 3.6: Steady state temperature distributions for high permeability (1.49 x 10^{-9} m^2) sediments with 7^{o}C, 9 ^{o}C and 18 ^{o}C above ambient cable surface temperatures from the lab experiments (a, b and c) and corresponding numerical simulation results (a', b' and c').

3.4 Discussion

3.4.1 Comparing the Different Thermal Regimes

To allow comparison of the temperature distributions between the steady state runs that are not affected by the different temperatures at the heat source or the variations in ambient conditions in the laboratory (i.e. characterize only the shape of the distribution rather than absolute values), normalized difference surfaces are generated using Figure 3.4c with a radial heat flow pattern at 60^{o}C above ambient temperature difference as reference in all cases. For example, for the 10^{o}C (Figure 3.5a) above ambient surface temperature experiment $(Nor.Diff_{10})$:

$$\mathrm{Nor.Diff}_{10} = \frac{\mathrm{T}_{10} - \mathrm{T}_{\mathrm{a}_{10}}}{\mathrm{T}_{\mathrm{m}_{10}} - \mathrm{T}_{\mathrm{a}_{10}}} - \frac{\mathrm{T}_{60} - \mathrm{T}_{\mathrm{a}_{60}}}{\mathrm{T}_{\mathrm{m}_{60}} - \mathrm{T}_{\mathrm{a}_{60}}} \qquad (3.2)$$

Where T, T_a , T_m are the observed TC, ambient, and maximum surface temperatures at steady state, and the additional suffix gives the temperature difference from ambient.

Thus, a normalized difference of zero implies that the shape of the temperature distribution is the same as the reference (Figure 3.4c), but not that the absolute temperatures, or the temperature increases above ambient, are the same. Normalised temperatures are close to zero (Figure 3.7a) within the low permeability sediments even up to 60 ^{o}C above ambient and also for the medium permeability sediments with skin temperatures up to 10 ^{o}C above ambient. However, within the medium permeability experiments, as the skin temperature increases above 19^{o}C, an area of small positive normalised temperature difference is observed above the heat source (Figure 3.7b). This becomes progressively larger in magnitude and extent as the temperature difference increases further (Figure 3.7c-3.7d), extending up to 80 cm above the source with a 55 ^{o}C skin temperature (Figure 3.7d). Within the high permeability sediments, even a 9^{o}C skin temperature leads to a high positive normalised temperature extending beyond 100 cm above the source while relatively small negative normalise difference develops up to 20 cm below and either sides of the source (Figure 3.7e-3.7f).

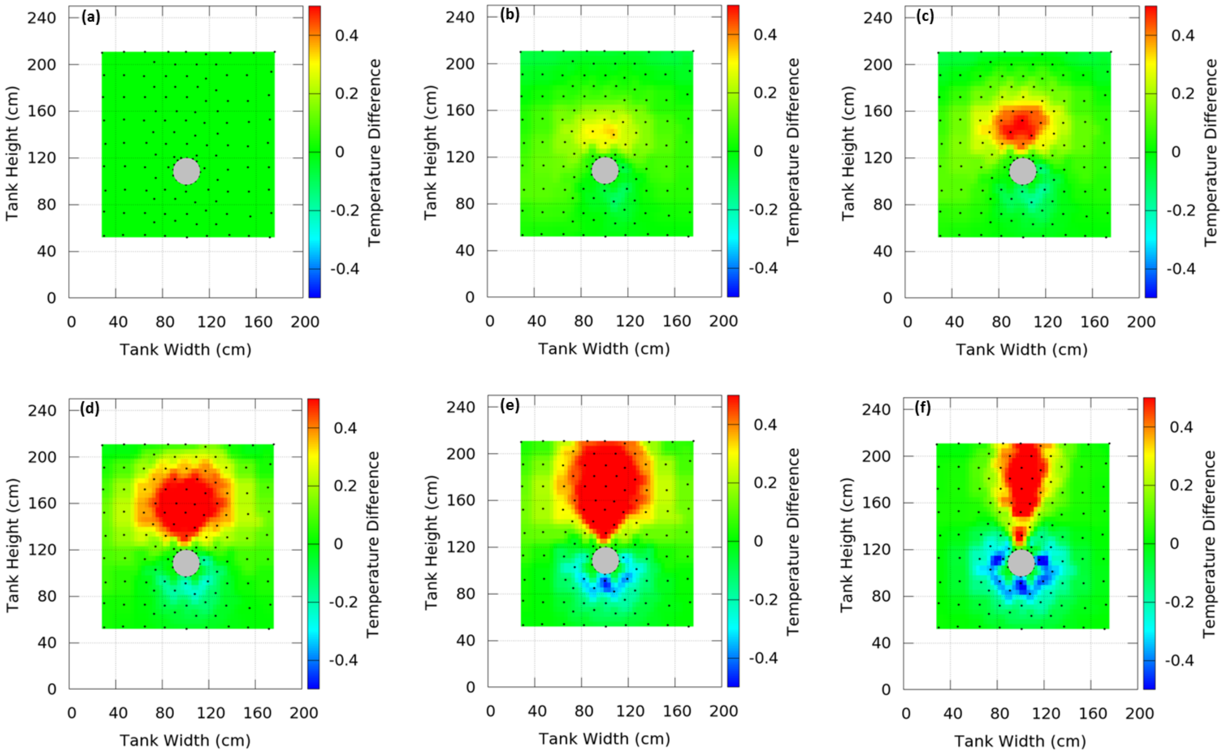

Figure 3.7: Normalised difference surfaces of the steady state temperature within: (a) low permeability (1.41 x 10^{-13} m^2) sediment with 45 °C above ambient skin temperature; (b), (c) and (d) medium permeability (5.0 x 10^{-11} m^2) sediment with skin temperature 36 °C, 43 °C, 55 °C above ambient respectively; and (e), (f) high permeability (1.49 x 10^{-9} m^2) sediment with skin temperature 9 °C, 18 °C above ambient cable surface temperature respectively.

3.4.2 Mode of Heat Transfer

The temperature distribution around a line source in homogeneous sediments is expected to be approximately radial if heat transfer is occurring by conduction (Carslaw and Jaeger, 1959, Turcotte and Schubert, 2002). All points on radial distance plot of temperature should fall along a radial curve for steady state conductive heat flow with negligible heat generation. However, at the onset of a convective heat flow, the points on the radial plots begin to scatter. Thus, the transition from conductive to convective heat transfer as a function of cable surface temperature and permeability are assessed statistically from the degree of scatter in the data and depicted by the histogram line plot of the standard deviation (Figure 3.11) of points as a function of surface temperature against 10cm bins of radial distance starting from the heat source surface.

For the low permeability thermal regimes, radial symmetry is clearly demonstrated by plotting the observed TC temperature against the radial distance of each TC away from the center of the internal heat source (Figure 3.8a to 3.8c). There is less than 4^{o}C temperature variation at any radial distance from the source, with high temperatures at the source and essentially ambient conditions at the furthest distances. The average standard deviation histograms of the binned radial scatter points with varying surface temperatures ranges from 0.03 to 0.05 (Figure 3.11a). Also the radial point plots (Figure 3.8a' to 3.8c') extracted from the FEM heat flow simulation shows radial symmetry with 0.03 average standard deviation and overlapped histogram plots for all temperatures (Figure 3.11a') that are comparable with the corresponding lab results.

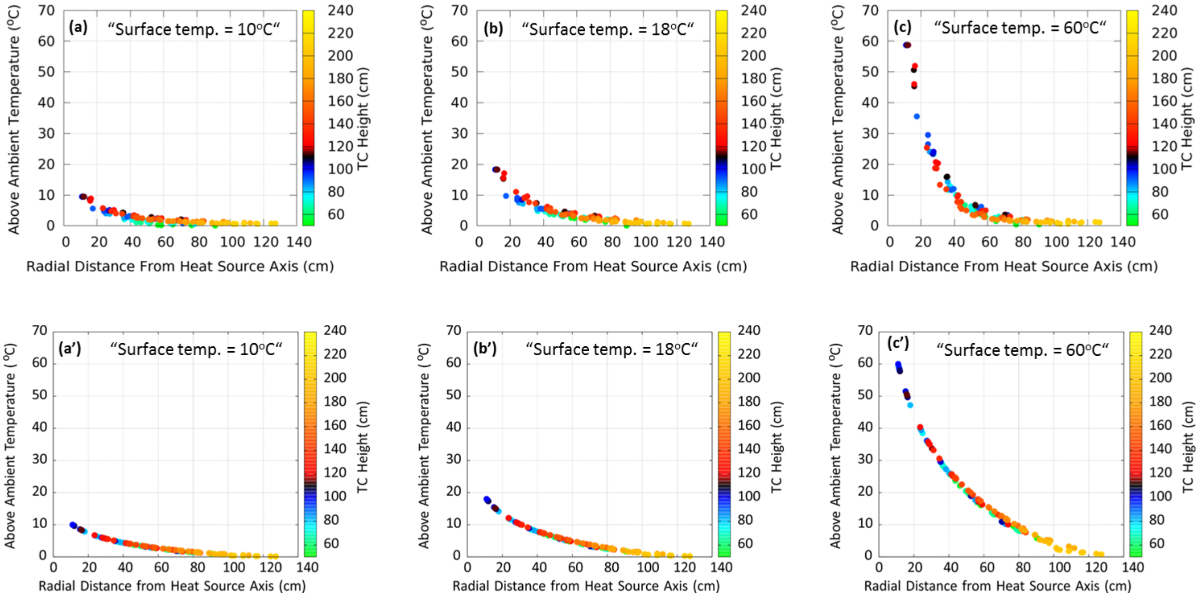

Figure 3.8: Radial steady state temperature distributions within low permeability (1.41×10^{-13} m^2) sediments with 10°C, 18 °C and 60 °C above ambient cable surface temperatures from the lab experiments (a, b and c) and corresponding numerical simulation results (a', b', c').

The observed thermal regimes within the medium permeability sediments (Figure 3.5), shows that at 10°C above ambient surface temperature, the temperature distribution is primarily radial with less than 4°C temperature range at any single distance from the source (Figure 3.9a). However, with increasing heat source temperatures this pattern changes as the range of temperature measurements at any single radial distance increases significantly (Figure 3.9b-3.9d), reaching 40°C at the highest surface temperature used (55°C: Figure 3.9d). TCs below the heat source (110cm height) show a similar temperature variation with distance irrespective of the temperature of the heat source. However, above the heat source, the spread in TC values is in response to the well-developed thermal plume (Figure 3.5c-3.5d). At 10°C heat source temperature, the standard deviation histogram of the binned radial scatter points shows a similar pattern to the low permeability case with an average value of 0.05. However, as the temperature increases from 19°C to

55^{o}C, the average value of the standard deviation histogram increases further; ranging from 0.6 to 1.5 respectively (Figure 3.11b). The critical (average) standard deviation per surface temperature value is 0.06 (representing the onset of radial asymmetric pattern) and it is the average degree of scatter with 19 ^{0}C (Figure 3.9b and 3.9b’). For the FEM heat flow simulations, the extracted radial point plots (Figure 3.9a’ to 3.9d’) shows radial symmetry at 10^{o}C heat source temperature with an onset of radial asymmetric pattern as the surface temperature exceeds 19^{o}C (Figure 3.9b’). Thus, the radial scatter points and standard deviation histogram plots (Figure 3.11b’) from FEM models are comparable with the corresponding lab experiment results.

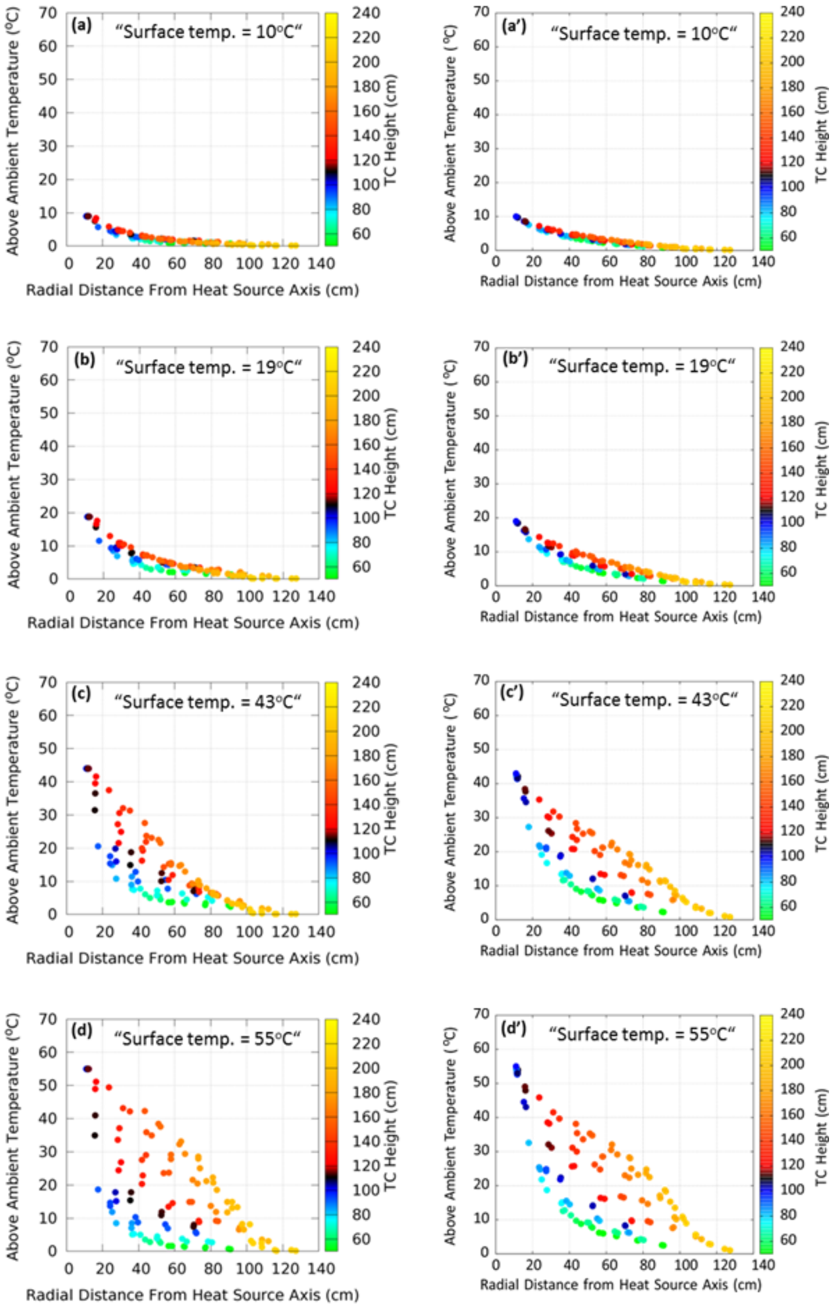

Figure 3.9: Radial steady state temperature distributions within medium permeability (5.0 x 10^{-11} m^2) sediments with 10 °C, 19 °C, 43 °C and 55 °C above ambient cable surface temperatures from the lab experiments (a, b, c and d) and corresponding numerical simulation results (a', b', c' and d').

For the observed high permeability thermal regimes, the plot of TC temperature against the radial distance from the heat sources (Figure 3.10a-3.10c), shows a broad spread of temperatures at each radial distance increasing from 6°C with a skin temperature of 7^{o}C above ambient to 18^{o}C with a skin temperature of 18^{o}C above ambient. The highest temperatures are recorded at the TCs above the heat source, and the TCs below the heat source remain essentially at ambient conditions. The average standard deviation histograms of the binned radial scatter points with varying surface temperatures ranges from 0.19 to 0.23 (Figure 3.11c). The radial point plots (Figure 3.10a' to 3.10c') extracted from the FEM heat flow simulation, also shows radial asymmetric pattern with an average standard deviation histogram plots (Figure 3.11c') that are comparable with the corresponding lab results (Figure 3.11c).

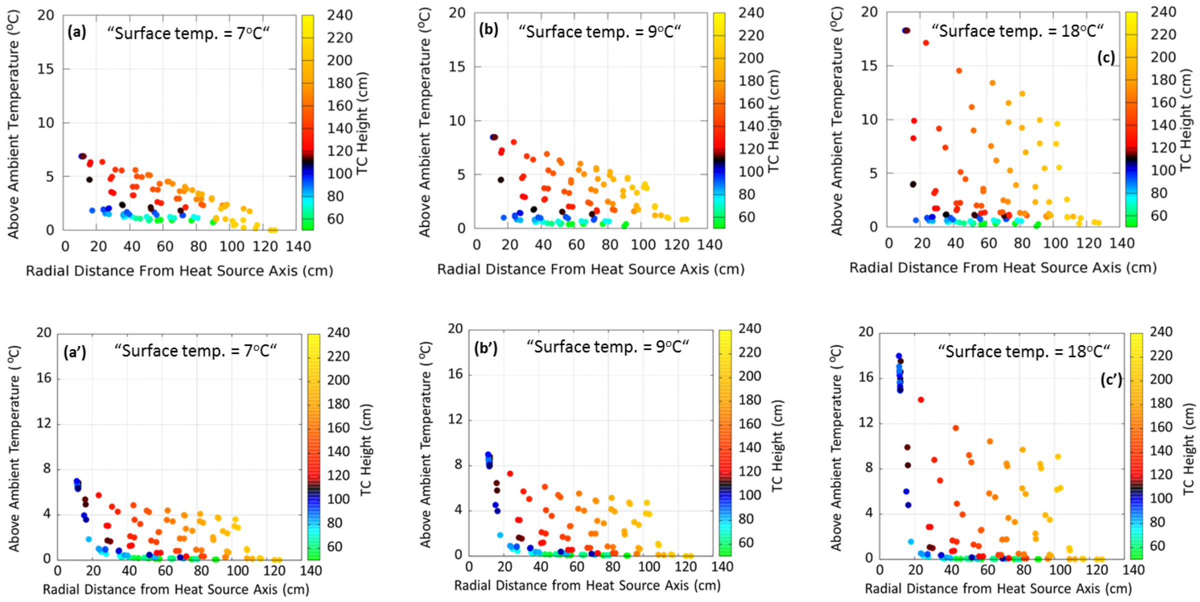

Figure 3.10: Radial steady state temperature distributions within high permeability (1.49 x 10^{-9} m^2) sediments with 7 ^{o}C, 9 ^{o}C and 18 ^{o}C above ambient cable surface temperatures from the lab experiments (a, b and c) and corresponding numerical simulation results (a', b', c').

Thus, the radial temperature distribution in our experiments suggests that the primary mode of heat transfer is conductive within the low permeability sediments irrespective of the heat source surface temperature (Figure 3.4 and 3.8) as well as conductive within the medium permeability sediments for heat source surface temperatures below 10^{o}C above ambient (Figure 3.5a, 3.5a’, 3.7a, 3.9a and 3.9a’). Conversely, the increasing non-radial component temperature distribution within the medium permeability sediments with 19^{o}C above ambient temperature, suggests the onset of convective heat transport (Figure 3.5b, 3.5b’, 3.7b, 3.9b and 3.9b’). The temperature distribution within the high permeability sediments is not radially symmetric even at 7^{o}C above ambient temperature, suggesting a convective heat transfer mode (Figure 3.6, 3.7e-3.7f and 3.10).

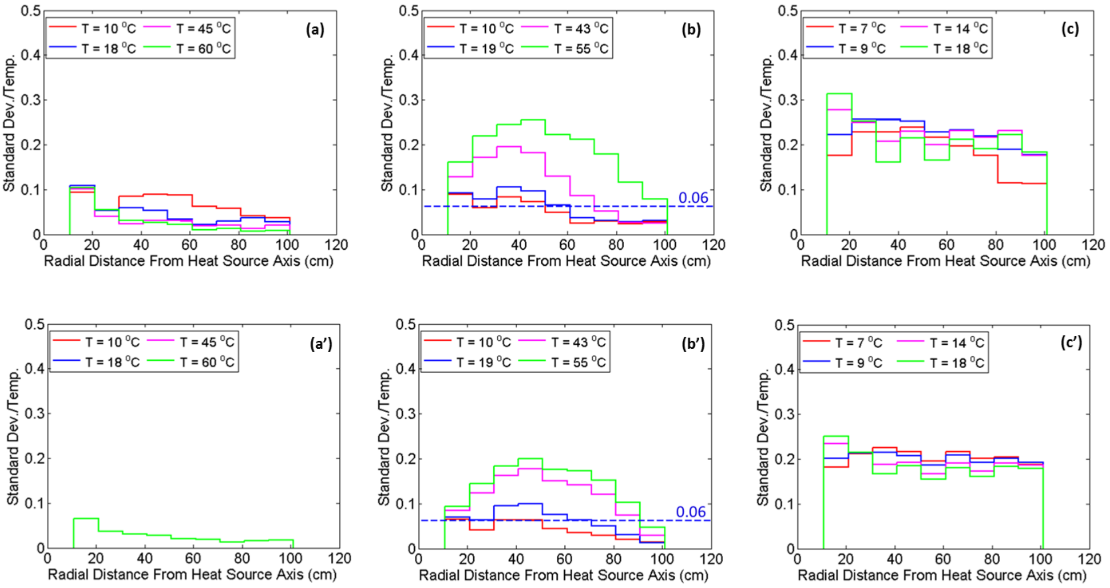

Figure 3.11: The standard deviation histograms of 10cm binned radial scatter points with varying surface temperatures within low, medium and high permeability sediments from the lab experiments (a, b and c) and corresponding numerical simulation results (a’, b’, c’). The critical (average) standard deviation per surface temperature value is 0.06 (horizontal dash blue line) which represent the onset of radial asymmetric pattern and transition from conductive to convective heat transfer.

To precisely ascertain the curve line for the transition from conduction to convection heat flows, further FEM heat flow simulations and associated radial plots were carried out. Figure 3.12 shows the numerical simulation results of the steady state heat flow surfaces and corresponding radial plots for 1.0 x 10^{-12} m^2 permeability sediments with varying above ambient cable surface temperatures. This further confirms radial temperature distribution and thus conduction heat transfer mechanism away from the heat source for surrounding sediments with permeability of 1.0 x 10^{-12} m^2 regardless of the heat source surface temperature.

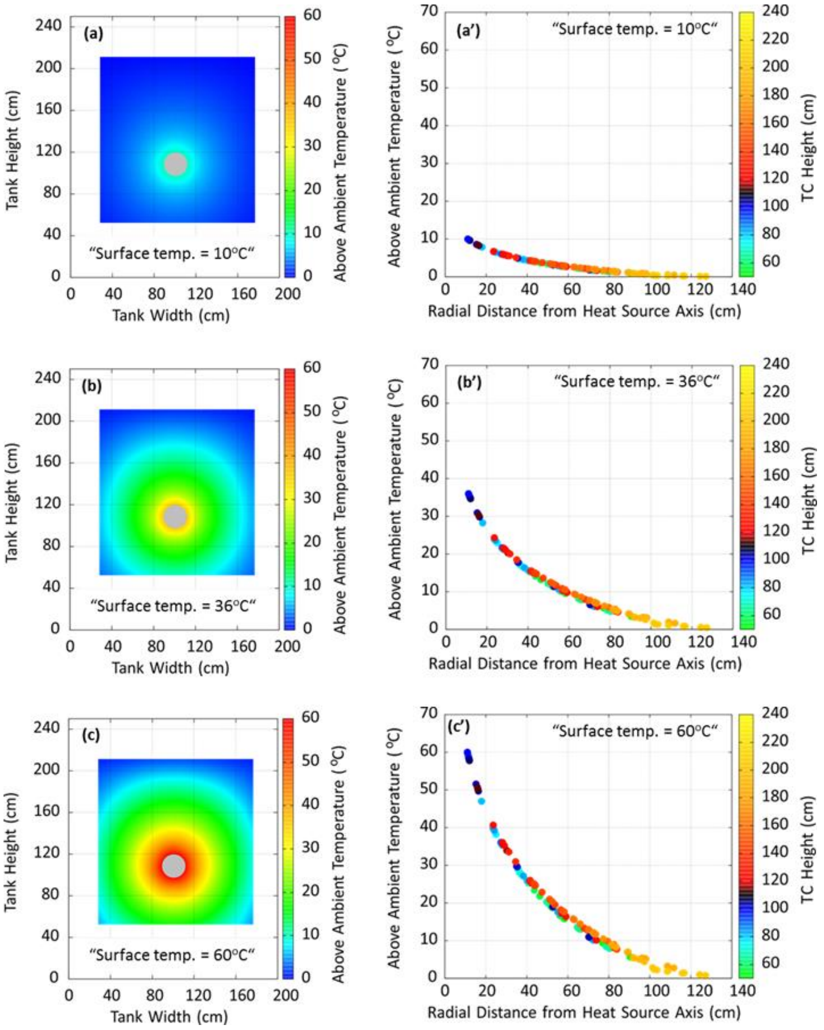

Figure 3.12: Numerical simulation results of the steady state heat flow surfaces and corresponding radial plots for 1.0 x 10^{-12} m^2 permeability sediments with varying above ambient cable surface temperatures: (a) 10 ^{o}C; (b) 36 ^{o}C and (c) 60 ^{o}C.

As the permeability of the surrounding sediment increases from 1.0 x 10^{-12} m^2 (Figure 3.12) to 1.67 x 10^{-11} m^2 (Figure 3.13 and 3.14), both the steady state heat flow surfaces (Figure 3.13) and corresponding radial plots (Figure 3.14) starts to show radial asymmetric heat flow pattern at 36 ^oC. Thus, signifying the onset of convection heat transfer at an above ambient heat source surface temperature of 36 ^oC.

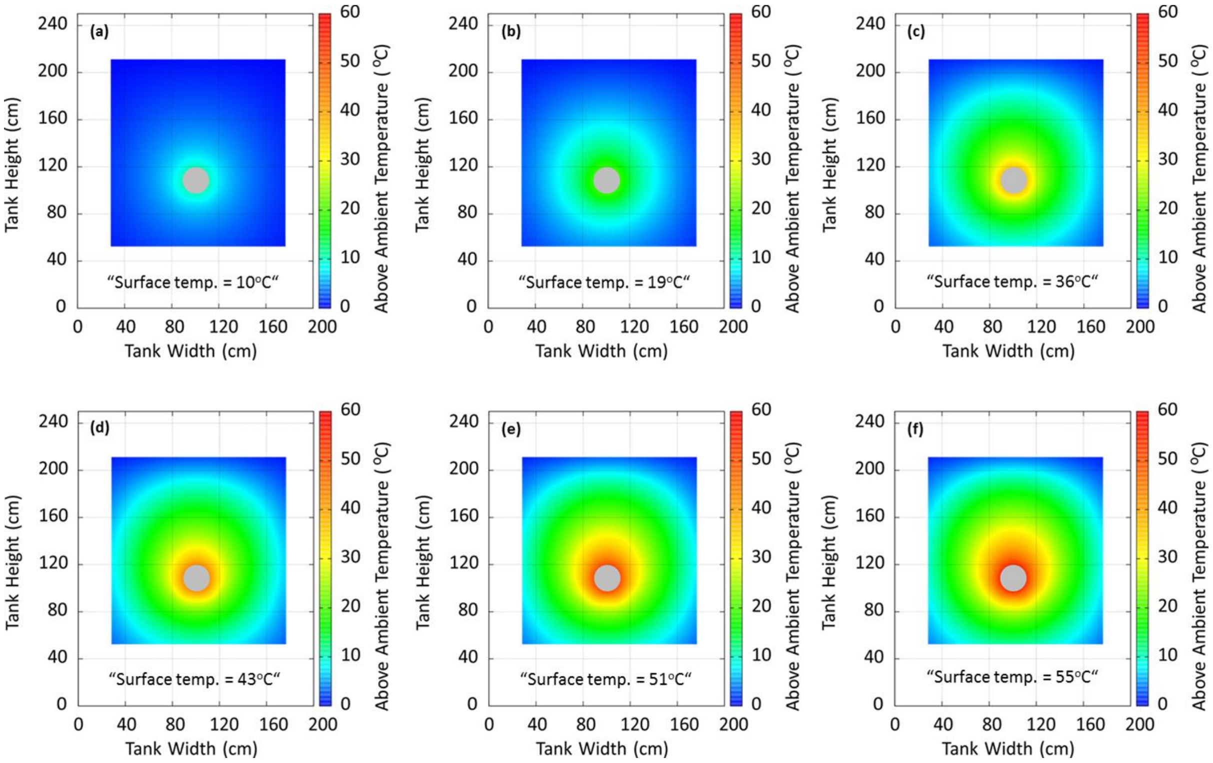

Figure 3.13: Numerical simulation results of the steady state heat flow surfaces for 1.67 x 10^{-11} m^2 permeability sediments with varying above ambient cable surface temperatures: (a) 10 ^oC; (b) 19 ^oC; (c) 36 ^oC; (d) 43 ^oC; (e) 51 ^oC and (f) 55 ^oC.

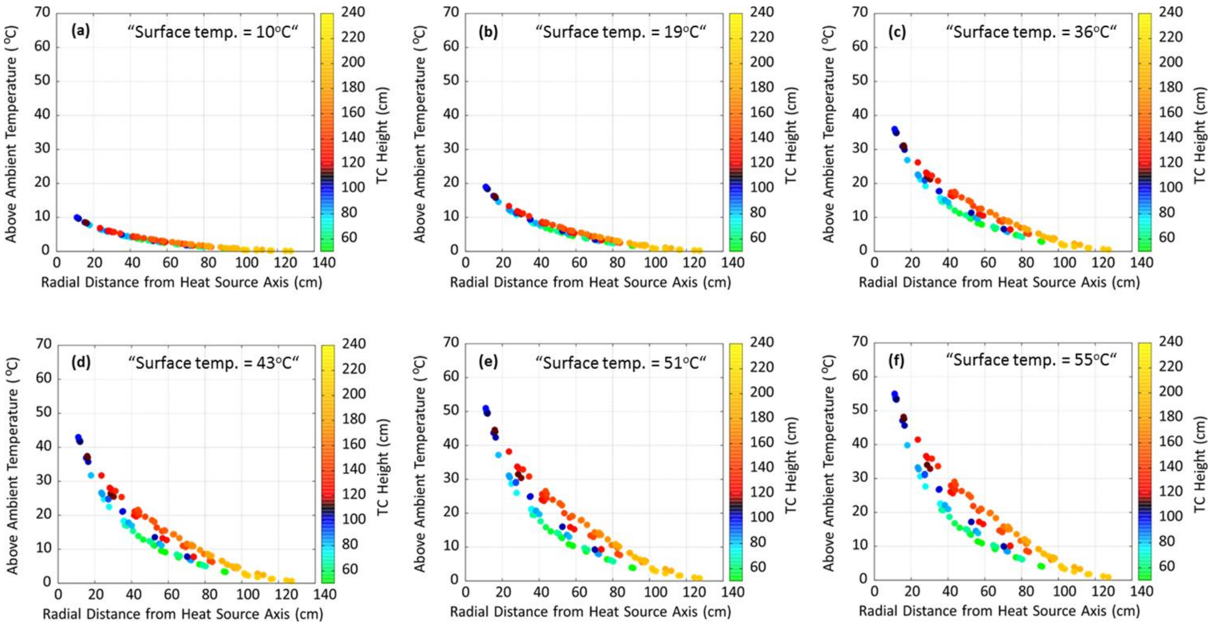

Figure 3.14: Numerical simulation results of the radial steady state temperature distribution for 1.67 x 10^{-11} m^2 permeability sediments with varying above ambient cable surface temperatures: (a) 10 °C; (b) 19 °C; (c) 36 °C; (d) 43 °C; (e) 51 °C and (f) 55 °C.

Furthermore, as the permeability of the surrounding sediment increases further from 1.67 x 10^{-11} m^2 (Figure 3.13 and 3.14) to 1.0 x 10^{-10} m^2 (Figure 3.15), both the steady state heat flow surfaces and corresponding radial plots (Figure 3.15) starts to show radial asymmetric heat flow pattern at 10 °C. Thus, signifying the onset of convection heat transfer at a comparatively lower above ambient heat source surface temperature of 10 °C.

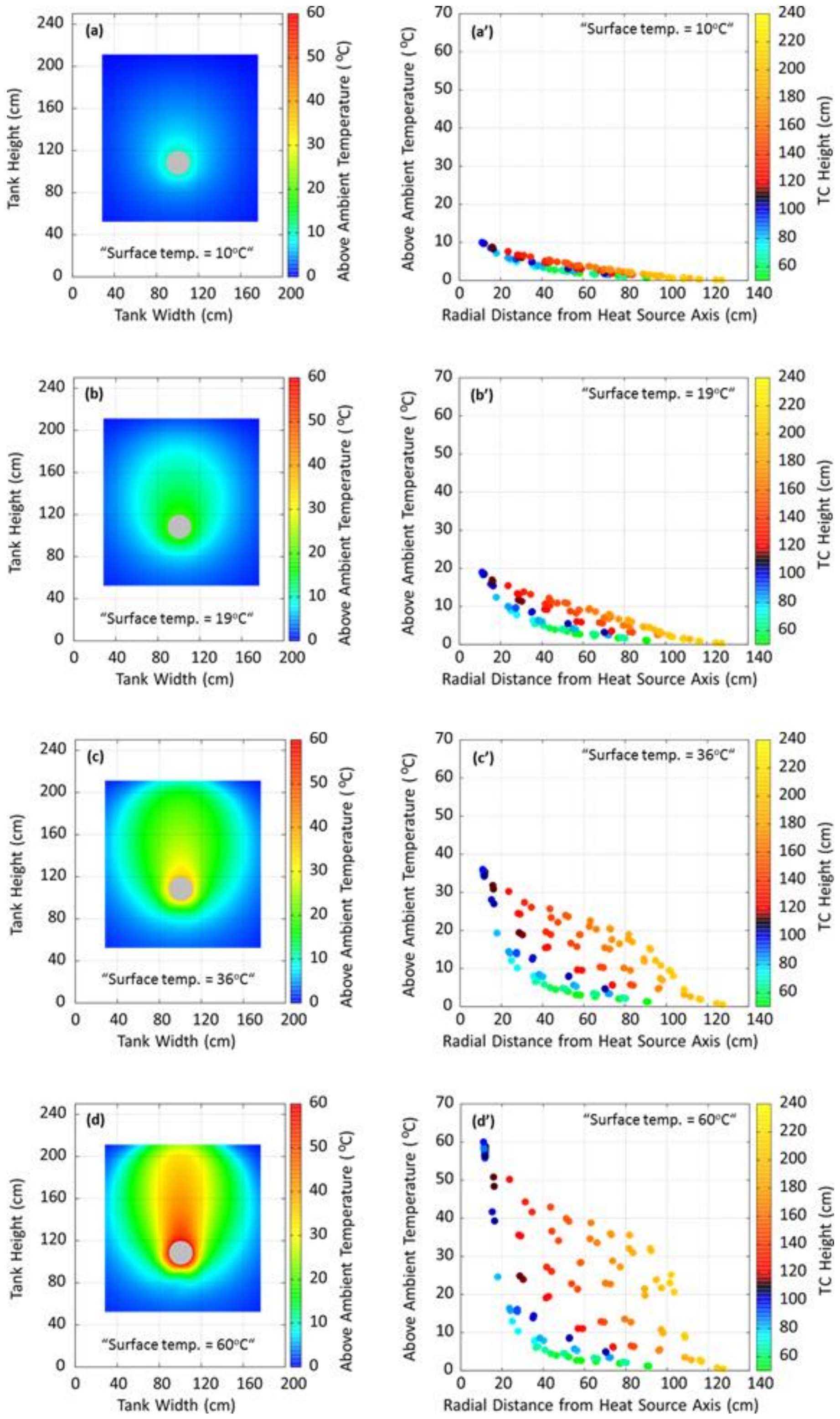

Figure 3.15: Numerical simulation results of the steady state heat flow surfaces and corresponding radial plots for 1.0 x 10^{-10} m^2 permeability sediments with varying above ambient cable surface temperatures: (a) 10 °C; (b) 19 °C; (c) 36 °C and (d) 60 °C.

Figure 3.16 shows the transition curve line for the onset of convective heat transfer and the space of cable surface temperature and permeability that leads to conductive and convective heat transfer. All points with varying cable surface temperatures for permeabilities 1.41 x 10^{-13} m^2, 5.0 x 10^{-11} m^2 and 1.49 x 10^{-9} m^2 are overlapped points from both lab experiments and FEM heat flow simulations results. The additional result points along permeabilities 1.0 x 10^{-12} m^2, 1.67 x 10^{-11} m^2 and 1.0 x 10^{-10} m^2 with varying cable surface temperatures are only from FEM heat flow simulation results. (Figure 3.12 to 3.15).

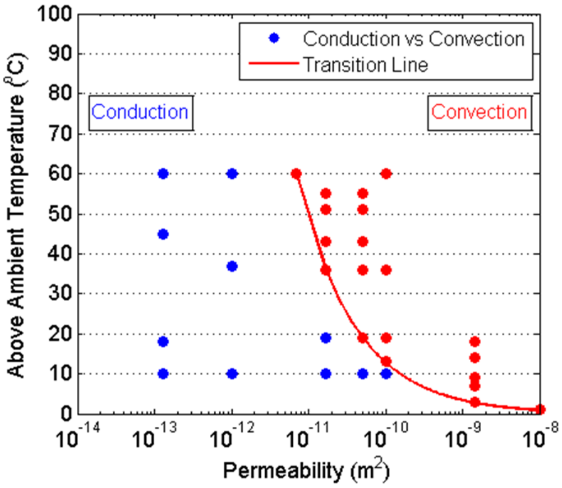

Figure 3.16: Plot of cable surface temperature against permeability of the surrounding Ballotini sediments, showing the onset of convective heat transfer (transition curve line) and the space of cable surface temperature and permeability that leads to conductive and convective heat transfer

Further, the increase of temperature above the heat source (Figures 3.7d-3.7f) is consistent with our interpretation of significant convective heat transport component, with pore fluid being heated around the source and rising vertically. The ambient temperatures recorded below the heat source show the convective recharge. This transition from conductive to convective heat transport is consistent with the predictions of the modelling approach of Hughes et al. (2015).

3.4.3 Implications For Environments Around Submarine HV Cables

Our results show that in the conductive examples (low permeability sediments, Figure 3.4c, and medium permeability sediments with low skin temperatures, Figure 3.5a) sediment temperature increases of more than 10^{o}C are limited to within less than a 40 cm radius of the heat source. However, in the convective heat transport regimes sediment can be heated by more than 10^{o}C at significantly greater distances above the cable. In medium permeability sediment, as the skin temperature increases beyond 19^{o}C, the heating extends beyond 40cm (Figure 3.5b) and increases to 100 cm as the temperature reaches 55^{o}C (Figure 3.5d). Furthermore, within high permeability sediments, the convective heating effect of at least 9^{o}C (Figure 3.6b) extends vertically beyond the typical 100 cm burial depth of submarine HV cables.

Thus, with regards to the environmental regulations of the German Federal Maritime and Hydrographic Agency (BSH) acceptable limit of < 2 K (2 ^{o}C) above ambient temperature rise at 20 cm below the seabed (BSH, 2014), our results clearly shows 2^{o}C temperature rise below the 20 cm depth line for conductive thermal regimes even for skin temperatures of 60^{o}C above ambient (Figure 3.17a-3.17b). However, the 2^{o}C temperature rise is above the 20 cm depth line for strongly convective thermal regimes even at 7^{o}C above ambient heat source skin temperature (Figure 3.17c-3.17d).

Furthermore, temperature is an important and long recognised environmental factor in the ecosystems of benthic biota (benthic communities and those living in the top 20 cm sub-seafloor). In particular, the convective thermal regime with observed above ambient temperature increase of between 5 and 14^{o}C in the top 20 cm (Figure 3.17c-3.17d) can impact the evolutionary, physiological and behavioural responses of benthic biota as well as impact their geographical distribution over both the short and long-term (Price *et al.*, 1979, Southward and Southward, 1988, Holt, 1990, Hiscock *et al.*, 2004). Species that cannot withstand and adapt to these high surrounding thermal regimes could diminish in abundance, become extinct or migrate to colder environments (Price *et al.*, 1979, Hiscock *et al.*, 2004).

The stability of the installed buried cable could be impacted by the geotechnical properties of the seabed and these properties may be significantly changed, both during installation as well as post-installation operation (SP-Transmission and NationalGrid, 2011). With external cable surface temperatures approaching 70°C (Swaffield *et al.*, 2008, Hughes *et al.*, 2015), the surrounding host seawater-saturated sediments will endure excessive thermal conditions. Consequently, in the short term, these excessive sediment temperatures could initiate significant pore-water convection (typical to Figure 3.17c-3.17d), movement of individual grains, reduction of bed shear stress (and fluidization), enhanced erodibility and seabed scour; leading to possible cable exposure and damage by ship anchor and fishing gear. In the medium to long term, the temperature changes could cause changes in pore water and solid phase geochemistry including: degradation of solid organic matter, recrystallization and dehydration of clay minerals, mobilization of potentially toxic metals and precipitation of calcium carbonate.

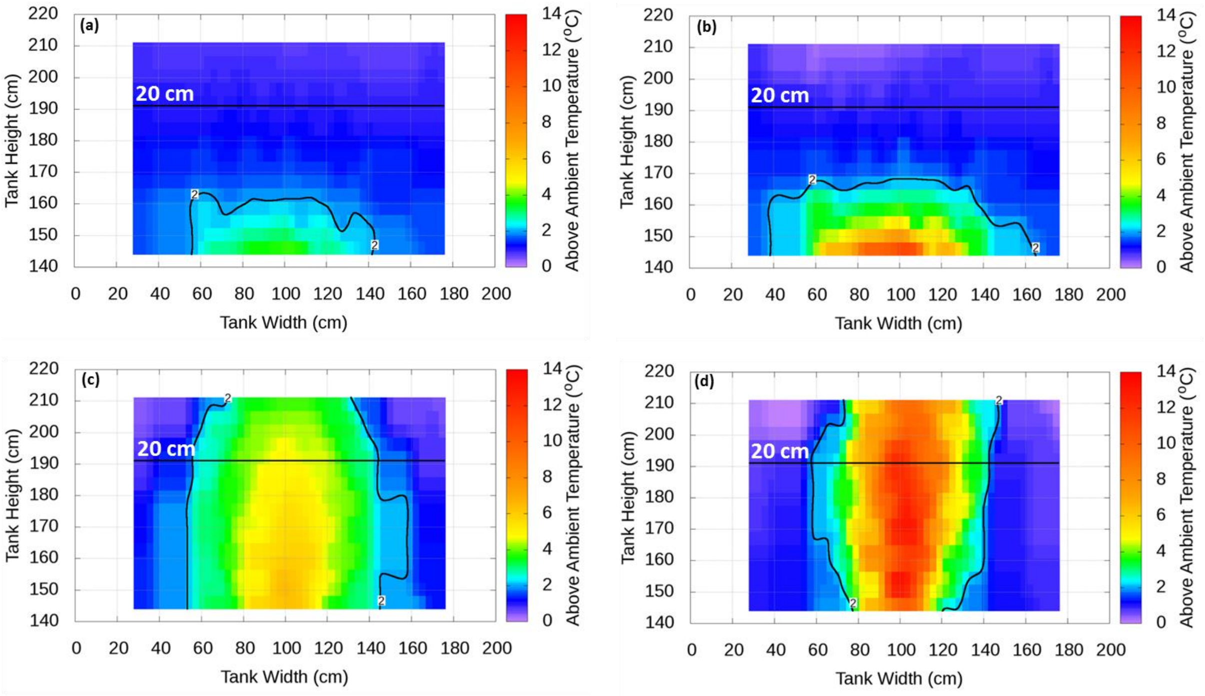

Figure 3.17: Steady state temperature surfaces for the upper 80cm of the sediments showing the 20 cm depth mark and 2 ^{o}C contour typical for: (a), (b) low permeability (1.41 x 10^{-13} m^{2}) conductive thermal regimes with skin temperature 18 ^{o}C and 60 ^{o}C above ambient respectively; and (c), (d) high permeability (1.49 x 10^{-9} m^{2}) convective thermal regimes with skin temperatures 9 ^{o}C and 18 ^{o}C above ambient respectively.

3.4.4 Implications For Cable Rating and Ampacity

Our results show the varied thermal regimes associated with submarine HV cables buried in different substrates, and conditions for occurrence of both conductive and convective heat transfer modes. Cable ampacity ratings are based on the ability to transfer heat generated by the cable into the surrounding environment. Excessive temperatures within the cable insulation would lead to premature cable degradation and potentially failure. Convective heat transport is significantly more efficient than conductive, so that the same heat transport produces a lower cable temperature (e.g., Hughes et al., 2015) due to the constant pore fluid recharge (Figure 3.8e-3.8f).

Since the transition between conduction-dominated and convection-dominated heat transport occurs within the ranges of sediment commonly found on continental shelves, the basic assumptions of isothermal ground temperature, homogeneous burial sediment and only conductive heat transfer as contained in the IEC 60287 standard (BS-IEC-60287-1-1:2014, 2014) are not appropriate for the marine environment. Use of this standard in coarser sediments with medium to high permeabilities where convection occurs will lead to significant under-rating of submarine HV cables. Consequently, we suggest that the influence of sedimentary environments on the thermal performance of cables should be taken into account during the cable route planning phases of such infrastructure projects.

3.5 Conclusions

Temperature measurements from a specifically designed 2D laboratory experiments were used to demonstrate the impacts of varying sediment permeability and generated temperature on the surrounding thermal regimes experienced by submarine HV cables buried within near surface shelf sediments. Our results suggest that, for submarine HV cables with surface temperatures up to 60°C above ambient and buried within clays to coarse silts with low permeability up to ~ 10^{-13} m^2, the surrounding thermal regime and mode of heat transfer will be dominantly conductive. Temperatures are only raised significantly within 40 cm radius of the cable. Fine sands with medium permeability ~10^{-11} m^2 are a transitional environment which is conductive at low cable surface temperatures, but becomes convective as the cable surface temperatures increase above ~20°C relative to ambient. Significantly increased temperatures are observed up to 1 m above the cable at skin temperatures of 55^{o}C. In very coarse sands with high permeability ~10^{-9} m^2 convective heat transfer occurs even at skin temperatures as low as 9°C above ambient, and the fluid remains hot over distances exceeding the typical 100 cm burial depth of submarine HV cables. These results are supported by the FEM model results run following the approach of Hughes et al. (2015). While widespread convective heat transport would increase cable ampacity ratings, it could also cause problems with existing environmental regulations which are based solely on temperature changes at a specific depth in the sediment.

Page intentionally left blank.

4

Subsea HV Cable Thermal Regime: Natural Sediments

4.1 Introduction

Chapter 3 (Emeana *et al.*, 2016) showed the varying thermal regimes and associated heat flow mechanisms around a HV cable analogue buried within coarse silt, fine sand and very coarse sand size artificial sediments. This work demonstrates the vital control of the surrounding sediment's permeability and cable surface temperature on these thermal regimes. In these earlier experiments, artificial ballotini sediments were used because of the high sorting, uniform particle size distributions, and spherical shapes of ballotini ensured greater control on the critical porosity and permeability estimates of the sediments. It is vital to understand how applicable the results of Chapter 3 (Emeana *et al.*, 2016) are to the real world where natural sediments have varying grain size distributions and sorting, grain shapes, textures, surface areas and compositions.

During convection heat transfer, the degree of flow of the heated pore fluids through the surrounding sediments are dominantly controlled by sediment permeability. However, for natural sediments with highly variable grain shapes and sizes, the permeability will be influenced by variations in pore structure due to a wide range of factors inherent to natural sediments; such as the grain size and grain size distribution, grain shape and packing, porosity and pore-space connectivity, tortuosity and constriction factors as well as their natural covariance (Carrier, 2003, Berg, 2014). Thus, the objectives of this research are to investigate the impacts of different pore structures within ballotini (eg. spherical and uniform grains sizes) and natural sediments (eg. varying grain sizes and shapes) on permeability estimates. An allied aim is to understand the thermal regimes within natural sediments and compare the results to the corresponding artificial ballotini sediments with similar permeability ranges. As such, this will allow us to understand how applicable the results of Chapter 3 are to real world situations.

4.2 Brief Review of Permeability Estimation Methods

The intrinsic permeability (k) of sediments depends on the solid matrix and are in some way correlated to sediment structure and grain-to-grain arrangements and thus the pore space of sediments (Darcy, 1856, Bear, 1988, Dullien, 1992, Berg, 2014). A fundamental question is how to understand the relationship between permeability (k) and porosity (n) using the pore structure characteristics, particularly for flow within natural sediments with varying grains shape, size, sorting and surface areas. This variability could reduce the effective pore space connectivity and the ease of fluid flow and thus the degree of flow of the heated pore fluids during convection heat transfer.

Kozeny-Carman Formula

A well-known relationship between permeability (k) and porosity (n) is the semi-empirical relationship (equation 4.1) initially proposed by Kozeny (Kozeny, 1927). Carman (1937) explained that linking the microscopic fluid velocity to the Darcy velocity for sediments involves scaling with the sediment tortuosity (τ), which describes the relative difference between the microscopic (interstitial) head gradient and macroscopic heat gradient. Thus Carman modified Kozeny's equation 4.1 as equation 4.2 (Carman, 1937). Equation 4.3 is the general simplified form of the Kozeny-Carman equation, which is mainly suitable for spherical and uniform grain sizes, as it simplifies the sediment tortuosity effect to a constant ($\frac{1}{180}$) and d_m is the effective (mean) grain size (Carman, 1937).

$$k \propto \tau \frac{n^3}{(1-n)^2} d_m^2 \qquad (4.1)$$

$$k \propto \tau^2 \frac{n^3}{(1-n)^2} d_m^2 \qquad (4.2)$$

$$k = \frac{1}{180} \frac{n^3}{(1-n)^2} d_m^2 \qquad (4.3)$$

Considering the grain specific surface area, Carman (1938, 1956) further modified equation 4.2 to equation 4.6 (Carman, 1938, Carman, 1956). Where γ, μ, C_{K-C}, S_0 and e are the fluid unit weight (a function of the density (ρ) and gravity (g)); fluid viscosity; Kozeny-Carman empirical coefficient, grain specific surface area per unit volume (cm^{-1}) and void ratio respectively. The void ratio is defined as the ratio of the volume of voids to the total volume of the sediment and is related to the porosity (equation 4.4 and 4.5). Where V_V, V_S and V_T are the void space, solids and total or bulk volume.

$$e = \frac{V_V}{V_S} = \frac{V_V}{V_T - V_V} = \frac{n}{1-n} \tag{4.4}$$

$$n = \frac{V_V}{V_T} = \frac{V_V}{V_S + V_V} = \frac{e}{1+e} \tag{4.5}$$

$$k = \left(\frac{\gamma}{\mu}\right)\left(\frac{1}{C_{K-C}}\right)\left(\frac{1}{S_0^2}\right)\left[\frac{e^3}{(1+e)}\right] \tag{4.6}$$

$\frac{\gamma}{\mu}$ = 9.93 x 10^4 cm^{-1} s for water (fluid) at 20° (Lambe, 1965, Terzaghi *et al.*, 1996) and for grains with uniform size and spherical shapes C_{K-C} = 4.8 $\pm$ 0.3 and normally used as 5, (Carman, 1956). Consequently, equation 4.6 can be simplified to equation 4.7:

$$k = 1.99 \times 10^4 \left(\frac{1}{S_0^2}\right)\left[\frac{e^3}{(1+e)}\right] \tag{4.7}$$

Carrier (2003) explained that S_0 can be estimated from the grain size distribution for sediments with uniform size and perfectly spherical grains of diameter, D (equation 4.8). Thus, equation 4.7, becomes equation 4.9.

$$S_0 = \frac{area}{volume} = \frac{(\pi D^2)}{\left[\left(\frac{\pi D^3}{6}\right)\right]} = \frac{6}{D} \tag{4.8}$$

$$k = 552 \times D^2 \left[\frac{e^3}{(1+e)}\right] \tag{4.9}$$

Carrier (2003) further demonstrates that for sediments with non-uniform size and spherical grains, the resultant effective diameter (D_{eff}) can be estimated using the grain size distribution and equation 4.10. Where f_i and $D_{ave\ i}$ is the grain fraction between two sieve sizes; larger [l] and smaller [s] (%) and mean grain size between two sieve sizes (cm). $D_{ave\ i}$ can be expressed by equation 4.11 and equation 4.8 becomes 4.12. Smaller grains will have the greatest effect on the estimated values of D_{eff} and S_0 (Carrier, 2003).

$$D_{eff} = \frac{100\%}{\left[\Sigma\left(\frac{f_i}{D_{ave\ i}}\right)\right]} \tag{4.10}$$

$$D_{ave\ i} = D_{li}^{0.5} \times D_{si}^{0.5} \tag{4.11}$$

$$S_0 = \frac{6}{D_{eff}} \tag{4.12}$$

Furthermore, to account for angularity in sediments grains, Carrier (2003) introduced a shape factor (SF), equation 4.13. Thus, equation 4.7 can be re-written as equation 4.14, which is similar to the Kozeny-Carman formula modifications (Fair and Hatch, 1933, Loudon, 1952, Carman, 1956, Todd, 1959). The shape factor (SF) provides an understanding of the sediment grain morphology and can be calculated using equation 4.15 (Rodriguez *et al.*, 2013). Where a, b and c are the long, intermediate and short lengths respectively, measured along the three axis of the sediment grain.

$$S_0 = \frac{SF}{D_{eff}} \tag{4.13}$$

$$k = 1.99 \times 10^4 \left(\frac{100\%}{\left\{\Sigma\left[\frac{f_i}{\left(D_{li}^{0.5} \times D_{Si}^{0.5}\right)}\right]\right\}}\right)^2 \left(\frac{1}{SF^2}\right)\left[\frac{n^3}{(1+n)}\right] \tag{4.14}$$

$$SF = \frac{c}{\sqrt{a * b}} \tag{4.15}$$

However, the Kozeny-Carman equation is unsuitable for clay-bearing sediments because it assumes there is no electrochemical reaction between sediment grains and pore fluid. However, it can be applied to non-plastic silts (Carrier and Beckman, 1984), sands and gravelly sands but not applicable to gravels of >3 mm effective grain sizes (Hazen, 1892, Scheidegger, 1974, Aberg, 1992, Carrier, 2003). Also its not applicable for very wide grain size distribution as well as for very irregular grain shapes due to re-entrant surfaces and intragranular porosity causing ‘‘dead end’’ and ‘‘bypassed’’ flow channels, which does not add to the effective specific surface area and pore space connectivity (Carrier *et al.*, 1991, Berg, 2014).

Thus numerous other investigators have proposed various relationships (Equation 4.16 - 4.21) for the description of permeability, taking into account the grain size and sediment type (e.g. Hazen, 1892; Terzaghi and Peck, 1964; Breyer, 1991; Slichter, 1898). These relationships are now described.

Hazen (1892): For uniformly graded sand but suitable from fine sand to gravel grain size range; provided the uniformity coefficient (U) of the grains are <2 and effective grain sizes between 0.1 and 3 mm (Terzaghi and Peck, 1964).

$$k = 6 \times 10^{-4}[1 + 10(n - 0.26)]d_{10}^{2} \qquad (4.16)$$

$$U = \left(\frac{d_{60}}{d_{10}}\right) \qquad (4.17)$$

Breyer (1991): For sediments with heterogeneous distributions, poorly sorted grains, uniformity coefficient (U) between 1 and 20 and from 0.06 mm to 0.6 mm effective grain size. Porosity is not considered.

$$k = 6 \times 10^{-4} \, log \frac{500}{U} d_{10}^2 \tag{4.18}$$

Slichter (1898): Most applicable for grain sizes ranging from 0.01 mm to 5 mm.

$$k = 1 \times 10^{-2} n^{3.287} d_{10}^2 \tag{4.19}$$

Terzaghi and Peck (1964): Most applicable for coarse-grained sand. C_t = sorting coefficient and ranges from 6.1 – 10.7 x 10^{-3}. An average C_t value of 8.4 x 10^{-3} was used for estimating the permeability of the ballotini and natural sediments, presented in section 4.3.1.

$$k = C_t \left(\frac{n - 0.13}{\sqrt[3]{1-n}} \right)^2 d_{10}^2 \tag{4.20}$$

U.S. Bureau of Reclamation (USBR) (1951): Most applicable for medium grain sand with a uniformity coefficient <5. This relationship uses d_{20} as the effective grain size and does not account for porosity.

$$k = 4.8 \times 10^{-4} \, d_{20}^{0.3} \times d_{20}^2 \tag{4.21}$$

A sensitivity test comparing the permeability estimates for the ballotini and natural sediments with the above stated empirical and semi-empirical relationships are presented in section 4.3.1.

4.3 Methods

4.3.1 Ballotini and Natural Sediment Characteristics

Energy Dispersive X-ray Microanalysis (Swift-ED from Oxford Instruments) were carried out using the Hitachi TM1000 Tabletop Scanning Electron Microscope (SEM) and demonstrates that the grains of the ballotini sediments are composed mainly of 63.0% silicon, 28.7% calcium and 5.6% sodium while the natural sediment grains are composed mainly of 90.7% silicon, 5.4% iron and 3.9% aluminium. The SEM was also used to provide high resolution sample images. The images clearly demonstrate that the surface morphology and shape of the ballotini grains are uniform, well rounded with high sphericity (Figure 4.1a-c) while the grains of the natural sediments are sub-rounded to sub-angular with low sphericity (Figure 4.1a'-c') (Powers, 1953). It also shows the variability in the grain's surface areas and texture, with the ballotini grains very smooth (Figure 4.1a-c) while the grains of the natural sediments are very rough (Figure 4.1a'-c').

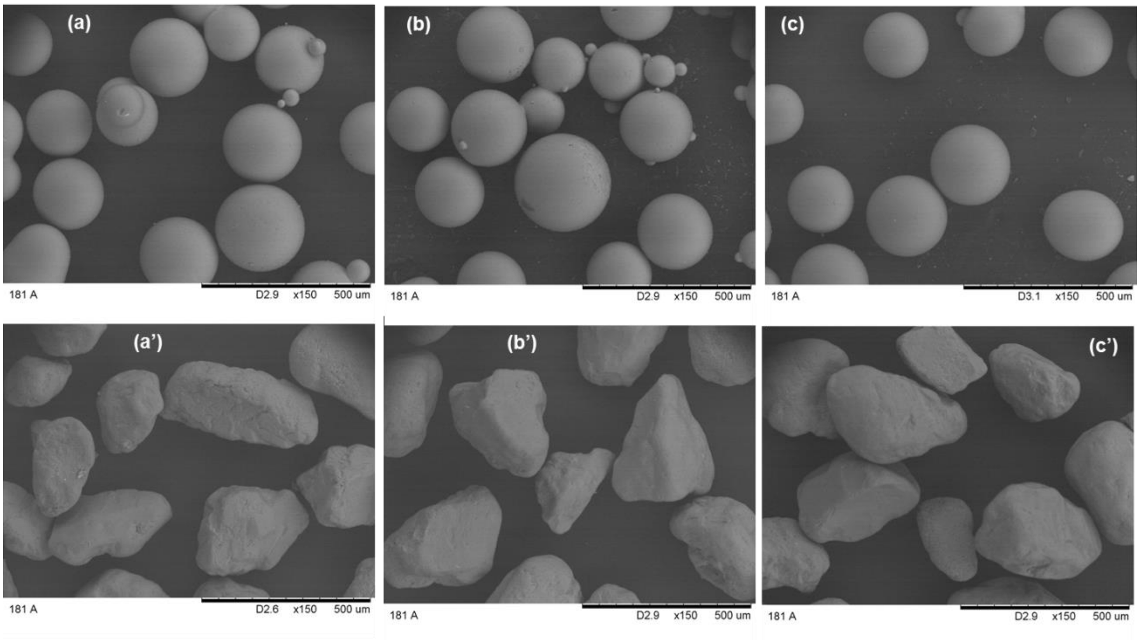

Figure 4.1: High resolution Scanning Electron Microscope (SEM) images demonstrating the variability in the surface morphology, shape, surface area and texture of the individual grains within in the ballotini (a-c) and natural (a’-c’) sediments.

Sieve particle size analysis demonstrates that both the ballotini and natural sediments are fine sands with symmetrical skewness and mesokurtic kurtosis (Figure 4.2 and Table 4.1) using the Folk and Ward (Folk and Ward, 1957) classification and Udden-Wentworth grain-size scale (Wentworth, 1922). However and importantly, it further shows that the ballotini is very well sorted with a narrow grain size distribution range, containing 94.2% fine sand and 5.2% medium sand. The natural sediments are moderately sorted with a wide grain size distribution, containing 52.8% fine sand, 43.0% medium sand and 4.2% very fine sand (Figure 4.2 and Table 4.1). These classifications are based on Folk and Ward (Folk and Ward, 1957) from GRADISTAT version 8 (Blott and Pye, 2001) and Udden-Wentworth grain-size scale (Wentworth, 1922).

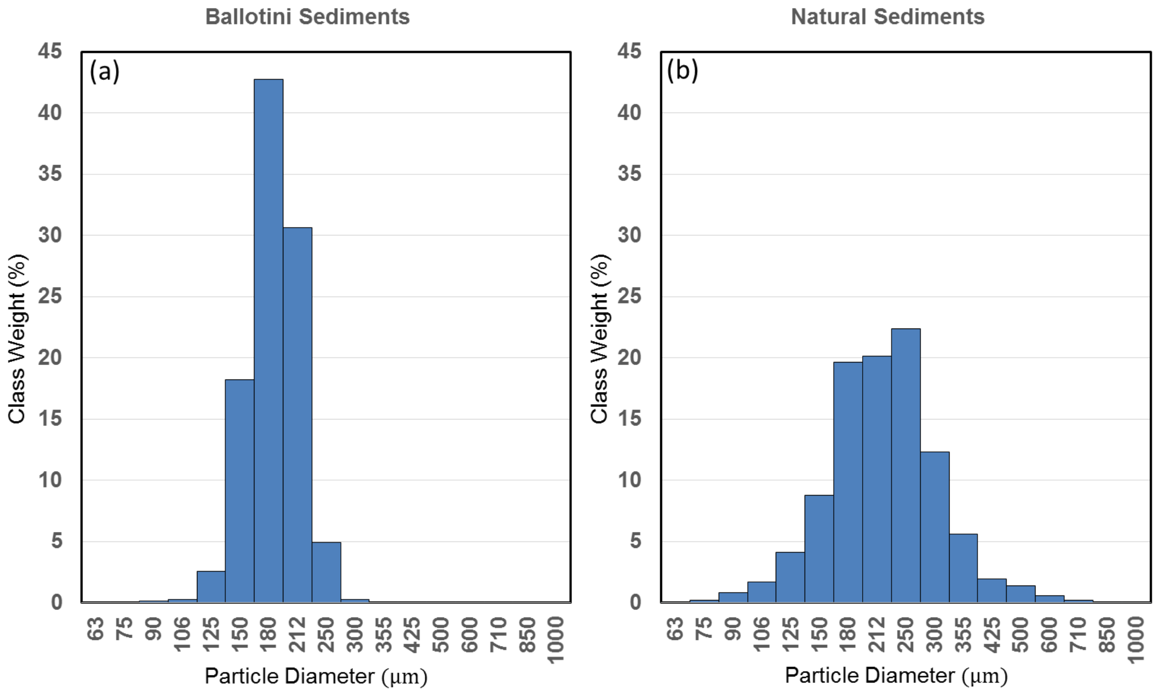

Figure 4.2: Comparison of the grain size distribution for the sand (a) ballotini and (b) natural sediments. It shows a narrow and wide distribution range for the ballotini and natural sediments respectively.

Table 4.1: Detailed comparison of the grain size statistics for the ballotini and natural sediments.

SAMPLE STATISTICS		BALLOTINI SEDIMENT	NATURAL SEDIMENT
GRAIN SIZE DISTRIBUTION	DESCRIPTION	CLASS WEIGHT (%)	CLASS WEIGHT (%)
	Medium sand	5.2	43.0
	Fine sand	94.2	52.8
	V. fine sand	0.6	4.2
FOLK AND WARD METHOD CLASSIFICATION	DESCRIPTION	GEOMETRIC (μm)	GEOMETRIC (μm)
	Mean	Fine Sand (203.3)	Fine Sand (246.7)
	Sorting	Very Well Sorted (1.17)	Moderately Well Sorted (1.45)
	Skewness	Symmetrical (-0.049)	Symmetrical (-0.007)
	Kurtosis	Mesokurtic (0.986)	Mesokurtic (1.044)
MEASURES OF CENTRAL TENDENCY	DESCRIPTION	(μm)	(μm)
	Mode	196.0	215.0
	D10	160.7	160.7
	Median (D50)	200.0	240.0
	D90	248.0	355.0

In order to understand the variability in the permeability estimates due to the variable grain shape, size and size distribution of the ballotini and natural sediments, a sensitivity analysis was carried out using the various empirical and semi-empirical permeability relationships presented in section 4.2. The median (50% mark) grain size was estimated and Equation 4.17 was used to calculate the uniformity coefficient of the sediment grains for which 60% and 10% of the sediments are finer

(Figure 4.3). The same approach was used to extract the d_5, d_{10}, d_{16}, d_{20}, d_{50}, d_{60}, d_{84}, d_{85}, d_{90} and d_{95} grain size values (Table 4.2). Subsequently, the logarithmic Folk and Ward (1957) graphical method was used to calculate the mean grain size (equation 4.22) and standard deviation (equation 4.23). Also the grain specific surface area was estimated using the calculated shape factor of 1 for ballotini with spherical grains and shape factor of 0.79 for the natural sediments with angular grains (Table 4.2). The shape factor calculations are based on Corey (1949) and Rodriguez (1949) approach using the SEM images (Figure 4.1). Subsequently, the sediment permeabilities are estimated (Table 4.2) using the various empirical permeability relationships presented in section 4.2.

$$Mean\ (GM) = \frac{\Phi_{16} + \Phi_{50} + \Phi_{84}}{3} \tag{4.22}$$

$$Standard\ Deviation\ (SD) = \frac{\Phi_{84} - \Phi_{16}}{4} + \frac{\Phi_{95} - \Phi_5}{6.6} \tag{4.23}$$

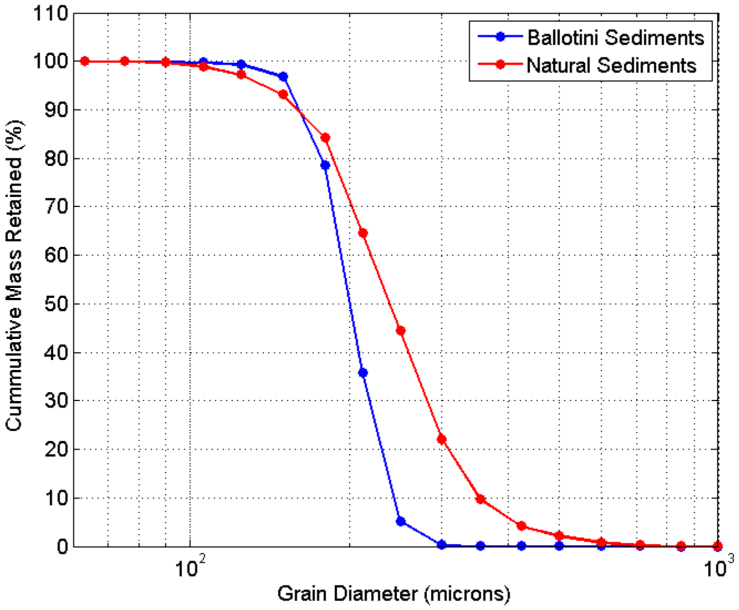

Figure 4.3: Cummulative grain size distribution curves for the ballotini and natural sediments.

Table 4.2: Ballotini and natural sediment permeability estimates from grain size analysis using various empirical relationships and shows the impacts of varying grain shape and size distribution

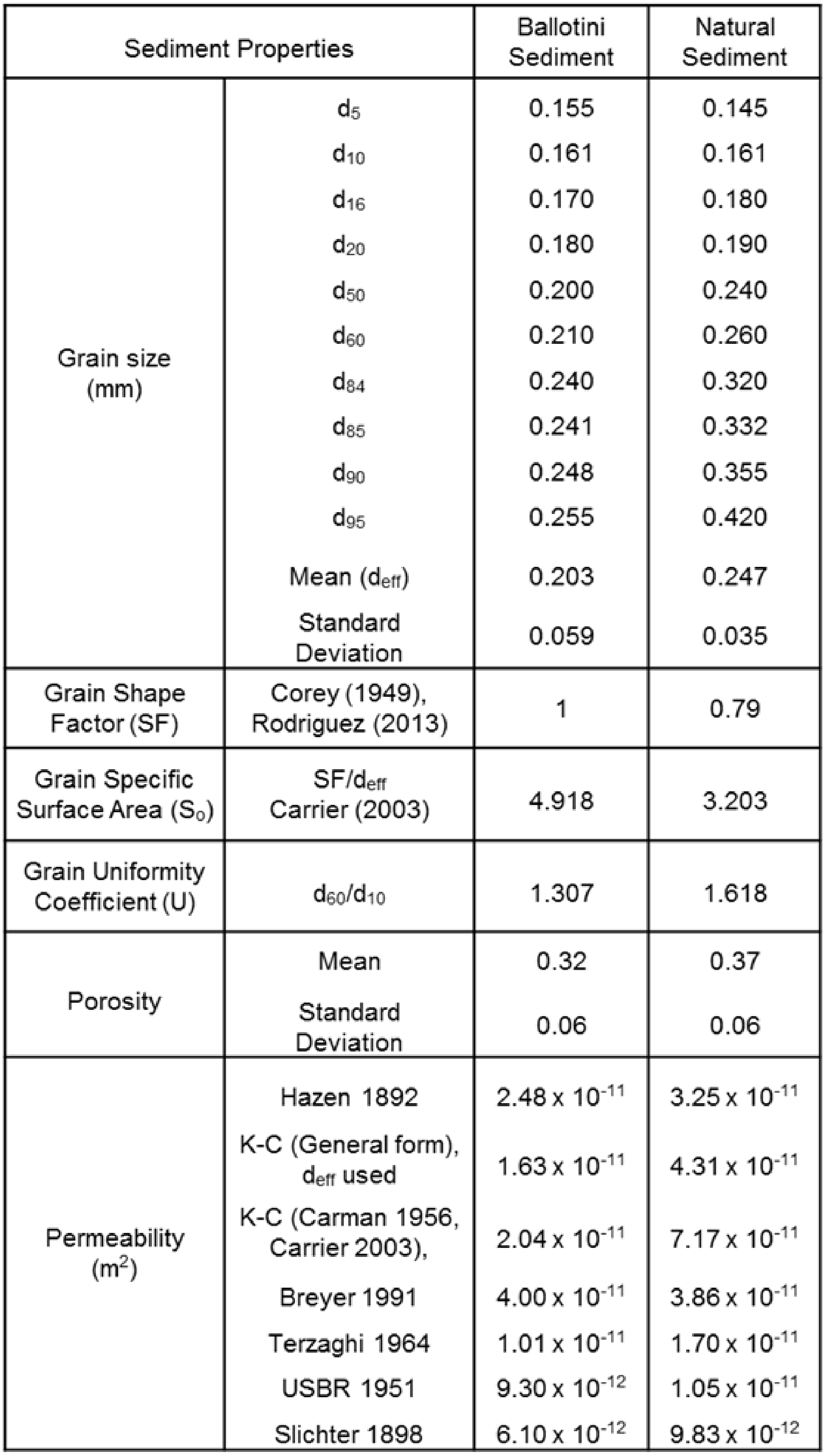

Sediment Properties		Ballotini Sediment	Natural Sediment
Grain size (mm)	d_5	0.155	0.145
	d_{10}	0.161	0.161
	d_{16}	0.170	0.180
	d_{20}	0.180	0.190
	d_{50}	0.200	0.240
	d_{60}	0.210	0.260
	d_{84}	0.240	0.320
	d_{85}	0.241	0.332
	d_{90}	0.248	0.355
	d_{95}	0.255	0.420
	Mean (d_{eff})	0.203	0.247
	Standard Deviation	0.059	0.035
Grain Shape Factor (SF)	Corey (1949), Rodriguez (2013)	1	0.79
Grain Specific Surface Area (S_o)	SF/d_{eff} Carrier (2003)	4.918	3.203
Grain Uniformity Coefficient (U)	d_{60}/d_{10}	1.307	1.618
Porosity	Mean	0.32	0.37
	Standard Deviation	0.06	0.06
Permeability (m^2)	Hazen 1892	2.48×10^{-11}	3.25×10^{-11}
	K-C (General form), d_{eff} used	1.63×10^{-11}	4.31×10^{-11}
	K-C (Carman 1956, Carrier 2003),	2.04×10^{-11}	7.17×10^{-11}
	Breyer 1991	4.00×10^{-11}	3.86×10^{-11}
	Terzaghi 1964	1.01×10^{-11}	1.70×10^{-11}
	USBR 1951	9.30×10^{-12}	1.05×10^{-11}
	Slichter 1898	6.10×10^{-12}	9.83×10^{-12}

The sensitivity analysis shows that the various permeability estimates (Table 4.2) for the ballotini and natural sediments are within the medium permeability ranges, as described in Chapter 3, and are within the same order of magnitude (~10^{-11} m^2). Estimates from Slichter (1898), USBR (1951) and Terzaghi (1964) relationships are relatively lower than for the other methods. This may be because the ballotini and natural sediments are both fine sands while the relationships of both USBR and Terzaghi are mostly applicable to medium grained to coarser grained sediments. Additionally, an average sorting coefficient (8.4 x 10^{-3}) was used in the Terzaghi estimates. The Hazen and Breyer relationships are suitable for fine sands and do not take into account the sediment porosity and thus, their respective results are closely comparable to the permeability estimates from the general form of the Kozeny-Carman, which incorporates the sediment porosity. This further validates the results of the measured porosity values. Finally, the permeability estimates using Carman (1956) and Carrier (2003) relationships takes into account the shape factor variability between the spherical ballotini and the natural angular sediments as well as the variability in their respective grain size distributions (Figure 4.1 - 4.3). Thus, adopted as the best permeability estimates for the ballotini (2.04 x 10^{-11} m^2) and natural (7.17 x 10^{-11} m^2) sediments (Table 4.2).

4.3.2 Experimental Set-up

Pilot experiments were initially carried in a small tank (0.80 m height x 0.40 m width x 0.10 m thickness) in order to assess the newly developed experimental set-up, recording and carrying out initial analysis of the temperature time series measurements. From the pilot temperature time series analysis, heat flow maps were generated to understand the thermal regimes upon application of internal heat flows through the surrounding sediments (Figure 4.8). Following on from successful test results from the small tank experiments, the experiment set-up was upscaled to a large tank (2.5 m height x 2.0 m width x 0.11 m thinkness) in order to provide a more realistic prototype-scale experimental set-up for modelling the burial thermal regimes of submarine HV cables to a typical burial depth of 1.0 m. Further description of the large tank experiment set-up are presented in Chapter 3 (subsection 3.2.1).

The small tank pilot measurements were carried out using 45 K6-type thermocouples (TCs) arranged in a 0.05 m x 0.05 m grid attached to a 0.30 m x 0.50 m frame (Figure 4.4) and inserted into a small tank (Figure 4.5). The TCs are attached to a rigid frame to avoid movement while the sediments or water are added into the tank and maintain their measured locations used for generating the heat flow maps. The 0.05 m x 0.05 m regular spaced TC grid pattern allows dense recording of the temperature distribution away from the heat source. The small tank is constructed from 0.015 m thick Perspex, open only at the top to allow sediment and water in-fill and removal (Figure 4.5). The sides and base of the tank were insulated externally using three layers of 0.10 m thick Celotex™ TA4000 insulation sheets. More details of the insulation material properties are described in Chapter 3 subsection 3.2.1.

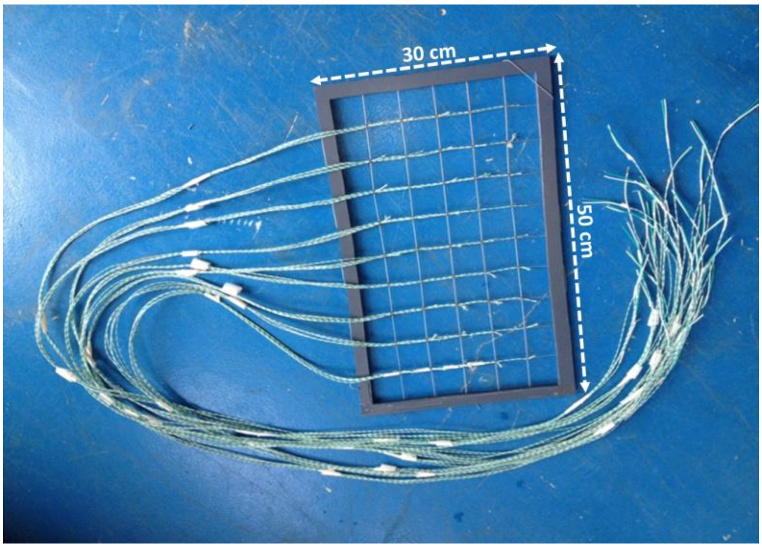

Figure 4.4: Photograph of the 45 thermocouples (TCs) arranged in a 5cm x 5cm grid used for measuring the sediment temperature time series data for the small tank experiments.

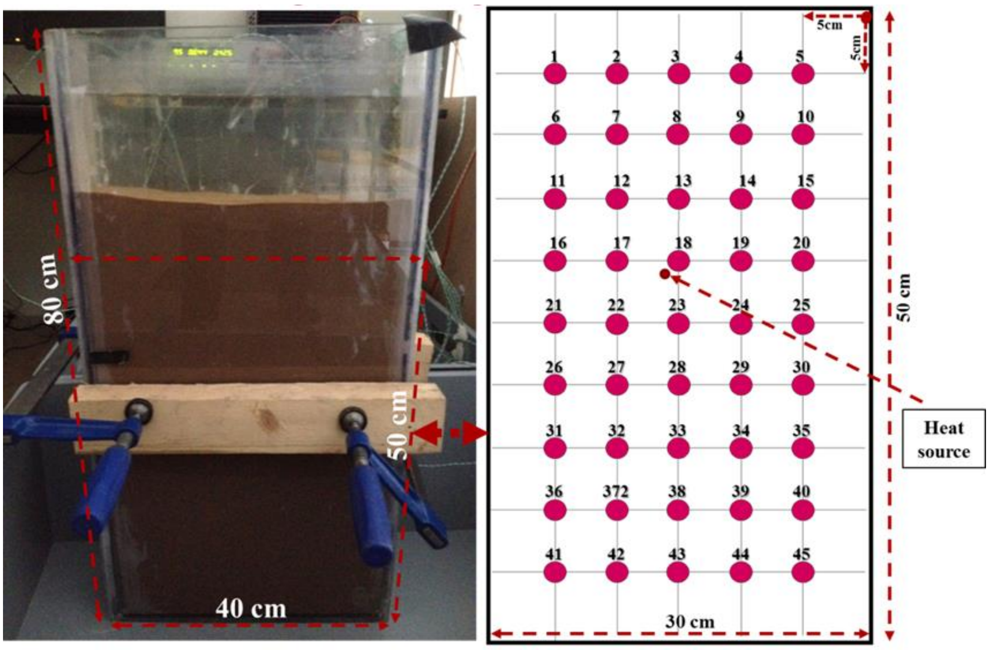

Figure 4.5: Photograph of the 2D experimental small tank (left) containing the fine sand natural sediments before the entire sides were insulated and a schematic diagram of the 45 TC locations (right).

The small tank was fitted with an internal cartridge heat source (generating a typical 12 Watts output power from a 50 Volts input and 0.24 amps current) powered from a connected electrical mains that is controlled and stabilised by a variable autotransformer (variac) and voltage stabilizer respectively. The inserted TCs were used to measure the sediment temperature change over time at 60 second intervals as the applied heat flows through the surrounding sediments (Figure 4.6a). The temperature time series measurements were also recorded using the same Campbell Scientific CR1000 measurement control system described in Chapter 3 and filtered with a 5 minute moving average filter to remove remnant temperature fluctuations while preserving the acquired data profile (Figure 4.6b). TC45 (i.e. bottom right hand corner of the tank) recorded the most stable ambient sediment temperature not affected by the fluctuating day and night room temperature. Thus, for reproducibility of each experimental run, all observed steady state time step temperature measurements were corrected using the temperature recorded at TC45, to give the above ambient sediment temperature measurements (see Chapter 3 subsection 3.2.3 for more details).

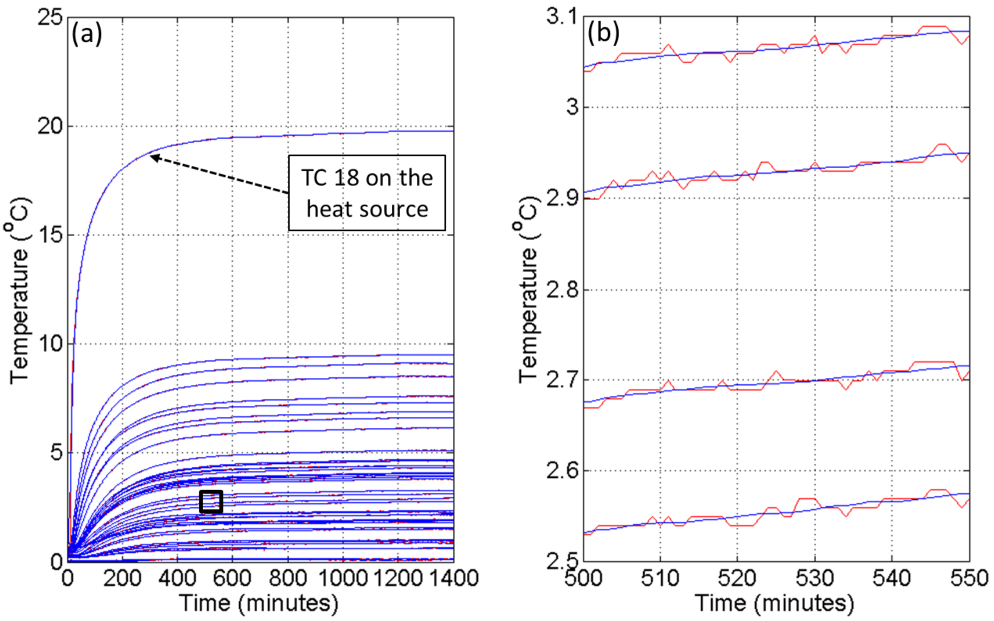

Figure 4.6: (a) Logged temperature time series measurements for 20°C above ambient temperature experiment and (b) zoomed in section (inserted black box) from (a) showing a clearer temperature time profile before (red line) and after (blue line) filtering.

4.3.3 Steady State Heat Flow Assessment

For the large tank ballotini experiment, the assessment method for attainment of steady state heat transfer and measurement reproducibility were presented in chapter 3 (subsections 3.2.2 and 3.2.3 respectively). Accordingly, for the small and large tank experiments using natural sediments, each run was allowed to continue until a steady state heat transfer was attained, as shown in Figure 4.7 with 20 °C and 43 °C above ambient heat source temperature for the pilot and large tank experiments respectively. Figure 4.7 shows the observed rate of change of temperature with time for TC18 and TC116 that are attached on the heat source and the subsequent TCs buried within the sediments that are vertically located above the small tank heat source (TC13, TC8 and TC3) and large tank heat source (TC56, TC69, TC81 and TC94). It further shows that steady state conditions are reached after 1300 minutes (~ 1 day) for the small tank experiments and after 8000 minutes (~6 days) for the large tank experiments.

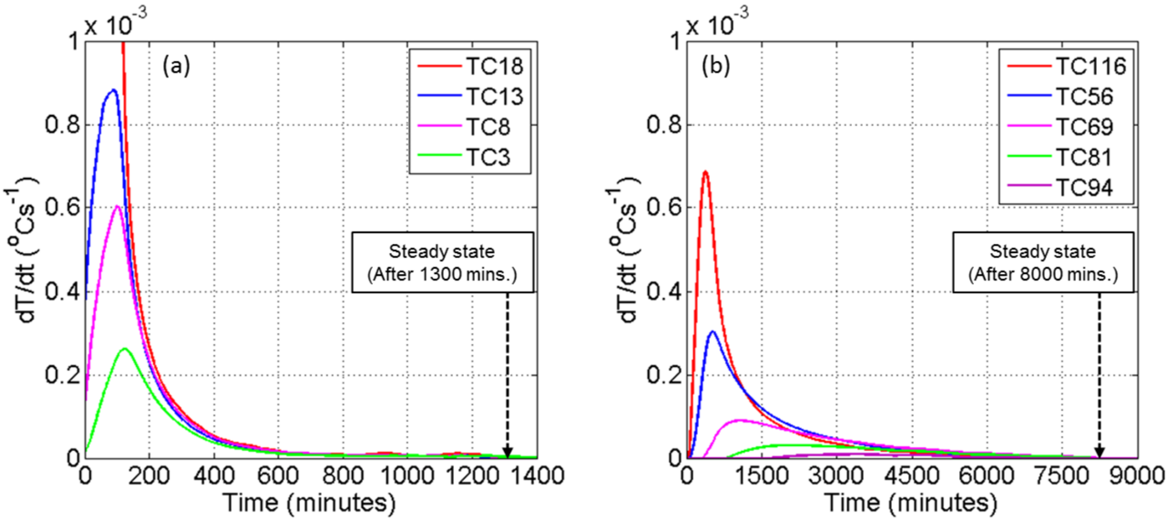

Figure 4.7: The rate of change in temperature (dT/dt) plot, showing attainment of steady state at zero dT/dt for the (a) pilot small tank with 20 ^{o}C heat source and (b) large tank with 43 ^{o}C heat source using the natural sediments.

4.4 Results

This section presents the results and analysis from the pilot small tank experiments carried out using a cartridge heat source with varying above ambient temperatures of 8^{o}C, 13^{o}C and 20^{o}C recorded from TC18 closest to the heat source (Figure 4.5). Also presented are the results from four experiments from the large tank using a uniquely designed heat source (see section 3.2.1) with above ambient surface temperatures of 10 ^{o}C, 20 ^{o}C, 43 ^{o}C and 55 ^{o}C recorded from TC116 on the heat source (Figure 3.1). The observed steady state temperature distribution were analysed using normalised heat flow surfaces and radial temperature plots to determine the heat transfer mode (conduction or convection) generated within the natural sediments with medium permeability used for both small and large tank experiments. Thus the steady state thermal regimes within the ballotini, natural sediments and FEM numerical models with varying heat source skin temperature are compared to assess the applicability of the results to real world environments.

4.4.1 Thermal Regime With Medium Permeability

The steady state thermal regimes were generated based on linear interpolation of the neighbouring temperature distributions measured at each TC location (Figure 3.1 and 4.5). For the small tank experiments, the generated steady state heat flow pattern shows radially symmetrical temperature distributions centred on the heat source, with surface temperatures of 8ºC (Figure 4.8a), 13ºC (Figure 4.8b) and 20ºC (Figure 4.8c) above ambient measured at TC18. Heating of the surrounding sediments of greater than 10ºC are centered on and extends up to 5 cm around the heat source (Figure 4.8c).

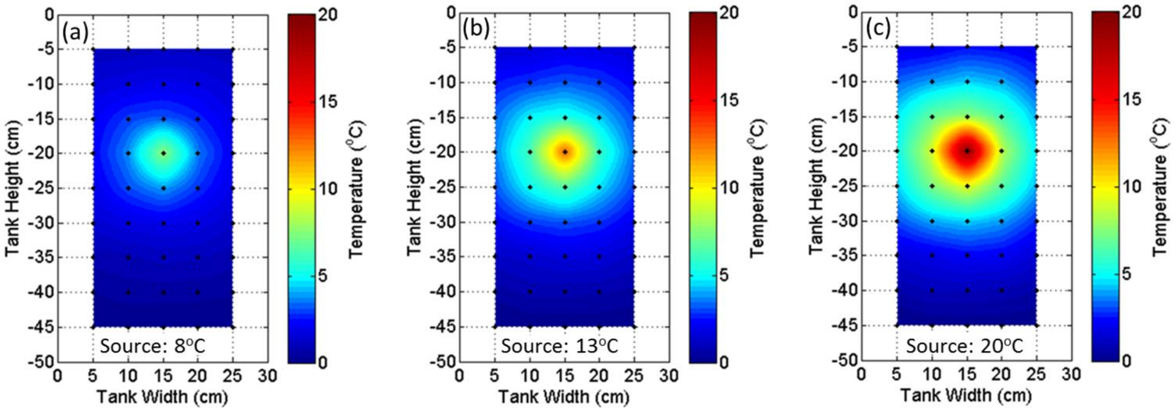

Figure 4.8: Observed steady state thermal regimes from the pilot (small-scale) experiments with medium permeability fine sand natural sediments and for varying heat source skin temperatures of (a) 8 ºC, (b) 13 ºC and (c) 20 ºC above ambient.

The generated steady state heat flow pattern from the large tank experiments are also radially symmetrical around the heat source when heat source surface temperatures are 10ºC above ambient (Figure 4.9a), but as the surface temperature increases beyond 20°C (Figure 4.9b-d); an asymmetric heat flow pattern begins to develop and grows with increasing source temperature. With a 20°C heat source, sediment heating of 10°C is limited to within 40 cm but as the heat source skin temperature increases beyond 20°C, this temperature field increases and generally rises vertically up to 100 cm from a 55°C above ambient heat source (Figure 4.9d).

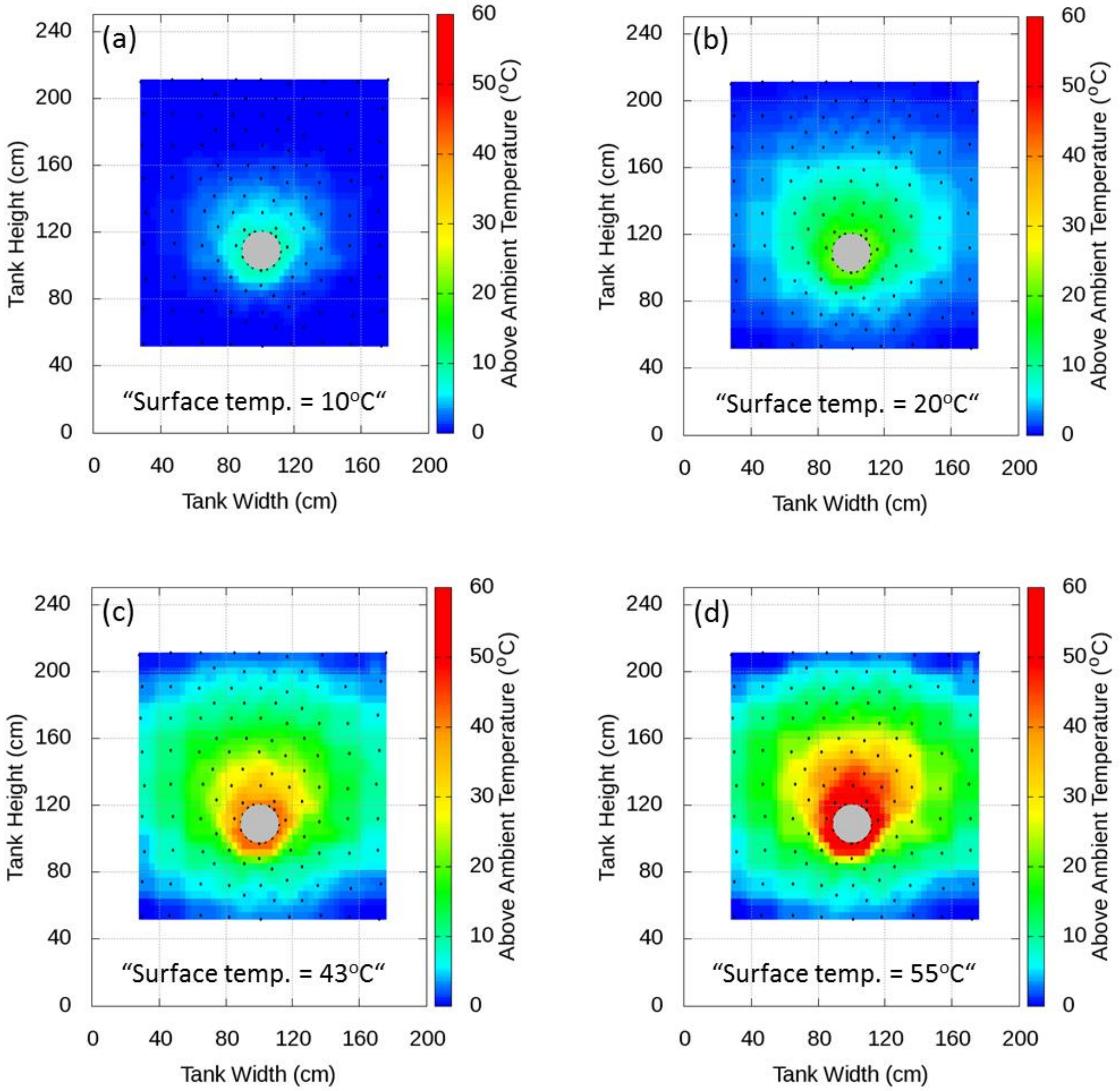

Figure 4.9: Observed steady state thermal regimes from the large tank experiments with medium permeability natural sediments (predominantly fine sands) and for varying heat source skin temperatures of (a) 10 °C, (b) 20 °C, (c) 43 °C and (d) 55 °C above ambient.

4.5 Discussion

4.5.1 Heat Transfer Mechanisms

As described in Chapter 2.2, for a line heat source buried within homogeneous sediments, the temperature distribution from the heat source through the surrounding sediments are typically radial, if the heat transfer mechanism is conduction (Carslaw and Jaeger, 1959, Turcotte and Schubert, 2002). Thus, for steady state conductive thermal regimes, a temperature radial distance scatter plot follows a radial curve and the deviation of the points away from the radial curve signifies the onset of a convective thermal regime.

For the small tank experiments, the temperatures at every 1cm x 1cm were extracted from the steady state thermal regimes (Figure 4.8a-c) and plotted against the radial distance of each point away from the centre of the internal heat source. Figures 4.10a-c are the corresponding temperature radial distance plots and show a clear radial symmetrical temperature distribution with 8, 13, and 20 ^{o}C above ambient heat source and less than 2 ^{o}C average temperature variation at any radial distance from the source. The observed scatter points of each radial plot follows a typical cooling pattern with high temperatures at the source (smaller radial distances) and ambient conditions at the furthest distances away from the source, towards the top and base of the tank. The computed average standard deviation of 2 cm binned radial scatter points with varying skin temperatures of 8, 13 and 20 ^{o}C is 0.03 with overlapped histogram plots for all skin temperatures (Figure 4.12a). This further confirms the radial temperature distribution pattern (Figure 4.8 and 4.10).

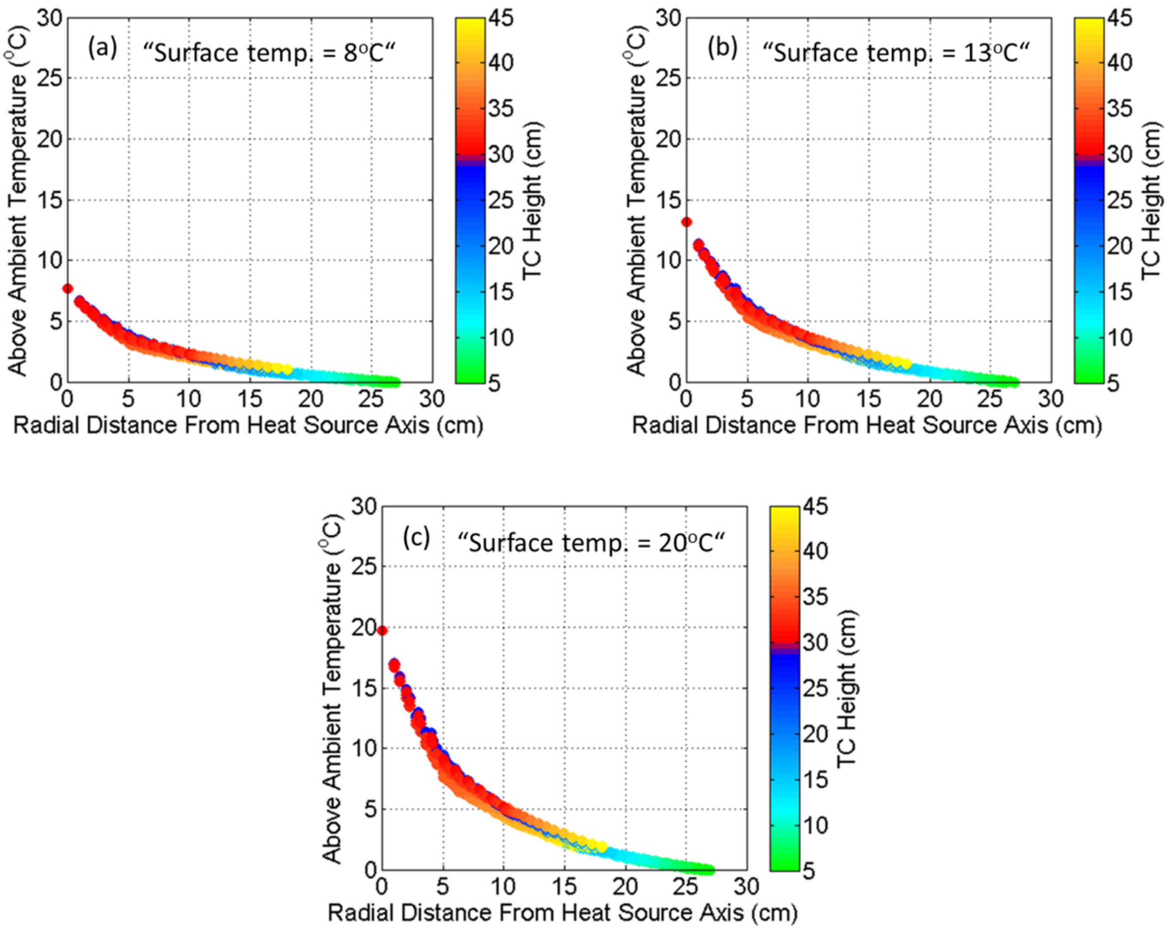

Figure 4.10: Radial steady state temperature distributions from the pilot small tank experiments for medium permeability natural sediments (predominantly fine sand) with varying heat source skin temperatures of: (a) 8 ^{o}C, (b) 13 ^{o}C; and (c) 20 ^{o}C above ambient.

Figure 4.11 shows the observed TC temperature against the radial distance of each TC from the heat source centre, using the steady state thermal regimes from the large tank experiments with natural sediments (Figure 4.9). This demonstrates that for 10^{o}C above ambient skin temperature, the temperature distribution follows a radial curve with less than 3^{o}C temperature variation at any radial distance (Figure 4.11a). However, as the heat source skin temperature exceeds 20^{o}C, the corresponding radial distance temperature plot starts to spread (Figure 4.11b) and expands with further increases in the skin temperature (Figure 4.11c-d). Thus, the average temperature variation at any radial distance from the source, reaches about 40°C for the highest (55°C) skin temperature used (Figure 4.11d). The computed average standard deviation of 10 cm binned radial scatter points with varying skin temperatures of 10, 20, 43 and 55°C are 0.046, 0.063, 0.121, and 0.139 respectively (Figure 4.12b). Thus, 0.063 represents the critical average standard deviation of the radial points for the onset of the radially asymmetric pattern.

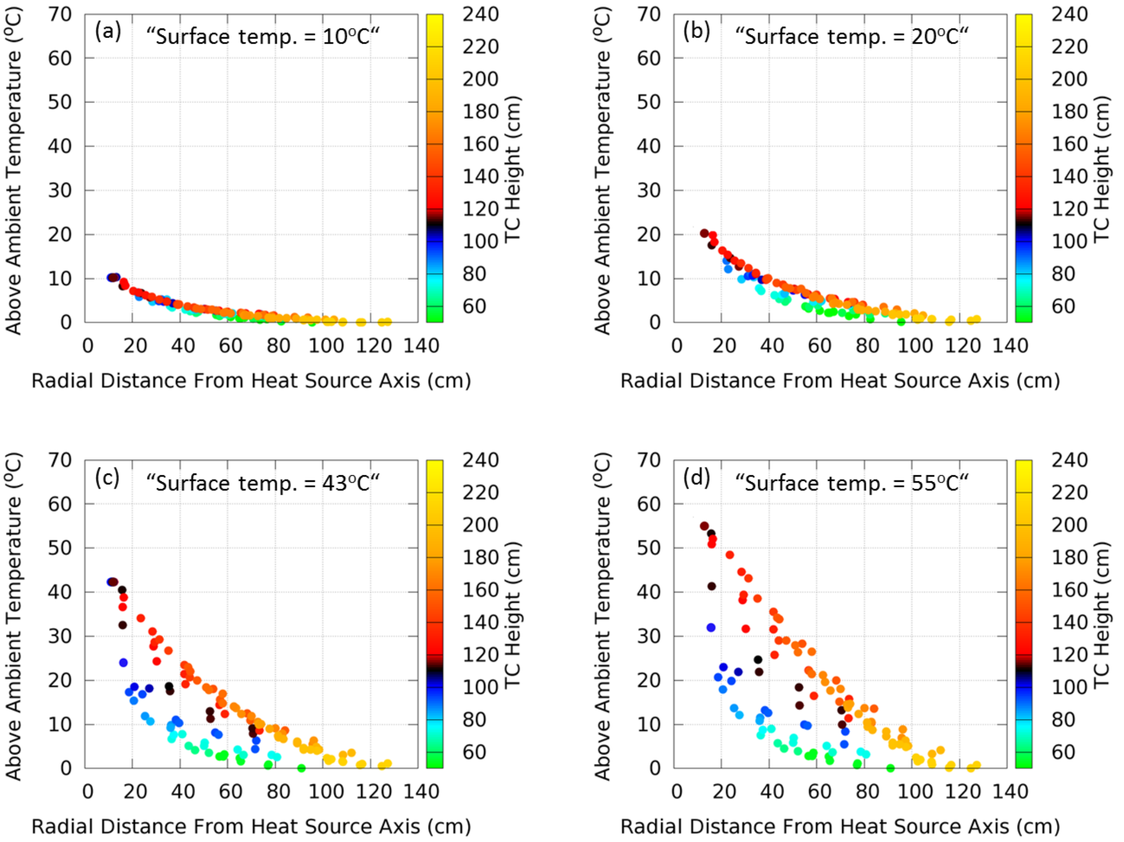

Figure 4.11: Radial steady state temperature distributions from the large tank experiments for medium permeability natural sediments with varying heat source skin temperatures of: (a) 10 °C, (b) 20 °C, (c) 43 °C and (c) 55 °C above ambient.

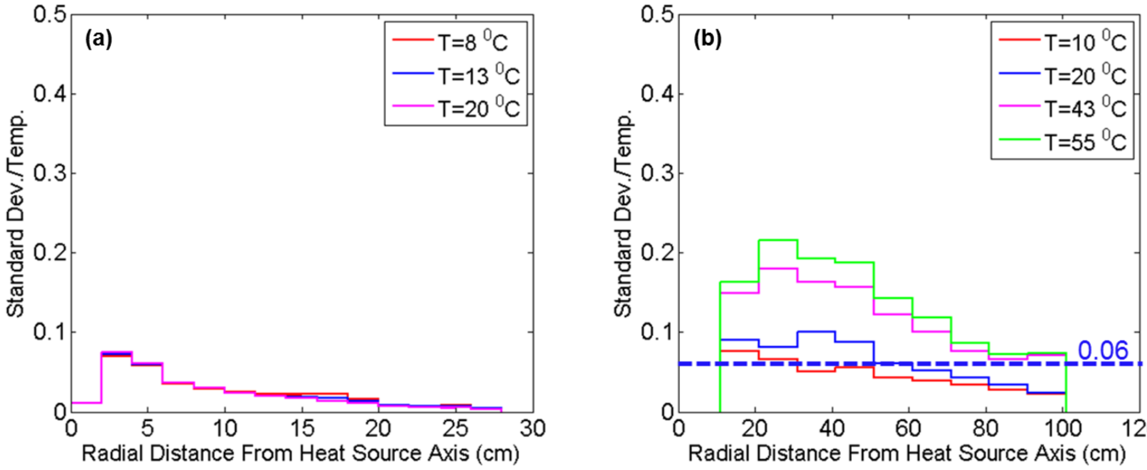

Figure 4.12: Standard deviation histograms of binned radial scatter points with varying surface temperatures for the small and large tank experiments with natural sediments. The horizontal dashed blue line represents the onset of radial asymmetric heat flow pattern and thus transition to convection heat flow.

With the medium permeability natural sediments, the symmetrical temperature distributions shown in Figures 4.8 and 4.10 further suggests that, for the pilot small tank experiments, irrespective of the heat source skin temperature (i.e. 8 to 20 ^{o}C), the dominant heat flow mechanism is conduction. For the large tank experiments with 10 ^{o}C, the symmetrical temperature distribution (Figure 4.9a and 4.11a) also suggests dominantly conductive heat transfer. However, as the skin temperature exceeds 20^{o}C, an asymmetric temperature distribution pattern starts to develop and thus suggests the onset of convection (Figure 4.9b and 4.11b). Figure 4.12 shows the standard deviation histograms plot used to quantitatively evaluate the degree of scatter of the radial points for each experiment and shows that 0.063 average standard deviation represents the threshold for the transition from conduction to convection heat transfer mechanism. This is also in agreement with results presented in chapter 3 (Figure 3.11).

4.5.2 Comparison of The Numerical, Ballotini and Natural Sediments Modelling Results

Figure 4.13 shows the comparison of the steady state thermal regimes of the FEM numerical modelling, ballotini, and natural sediments large tank experiments for medium permeability and varying above ambient heat source skin temperatures. In all three cases, the thermal regimes are symmetrical at low (10^{o}C) skin temperature with a transition to asymmetrical heat flow pattern at ~20^{o}C and growth of this asymmetric pattern as the skin temperature increases, signifying the onset of convection. As the skin temperature increases up to 55^{o}C and convective heat flow becomes dominant, the vertical thermal plume of at least 30^{o}C becomes more pronounced for the numerical modelling and artificial ballotini results, reaching a height of 60 cm above the heat source. However, the convective heat flow through the natural sediment with 55^{o}C skin temperature are less pronounced with a thermal plume of at least 30^{o}C above the heat soure of 40 cm high and 80 cm wide. This could be due to the comparatively wider grain size distribution (Figure 4.2), angular and variable shape (Figure 4.1) and sorting of the grains (Table 4.1) as well as the matrix content within the pores of the natural sediments. This [matrix content?] causes a relative obstruction to the flow of heated pore fluid during the convection heat transfer as compared to the ‘clean’ and spherical grains of the ballotini sediments with relatively little or no matrix content.

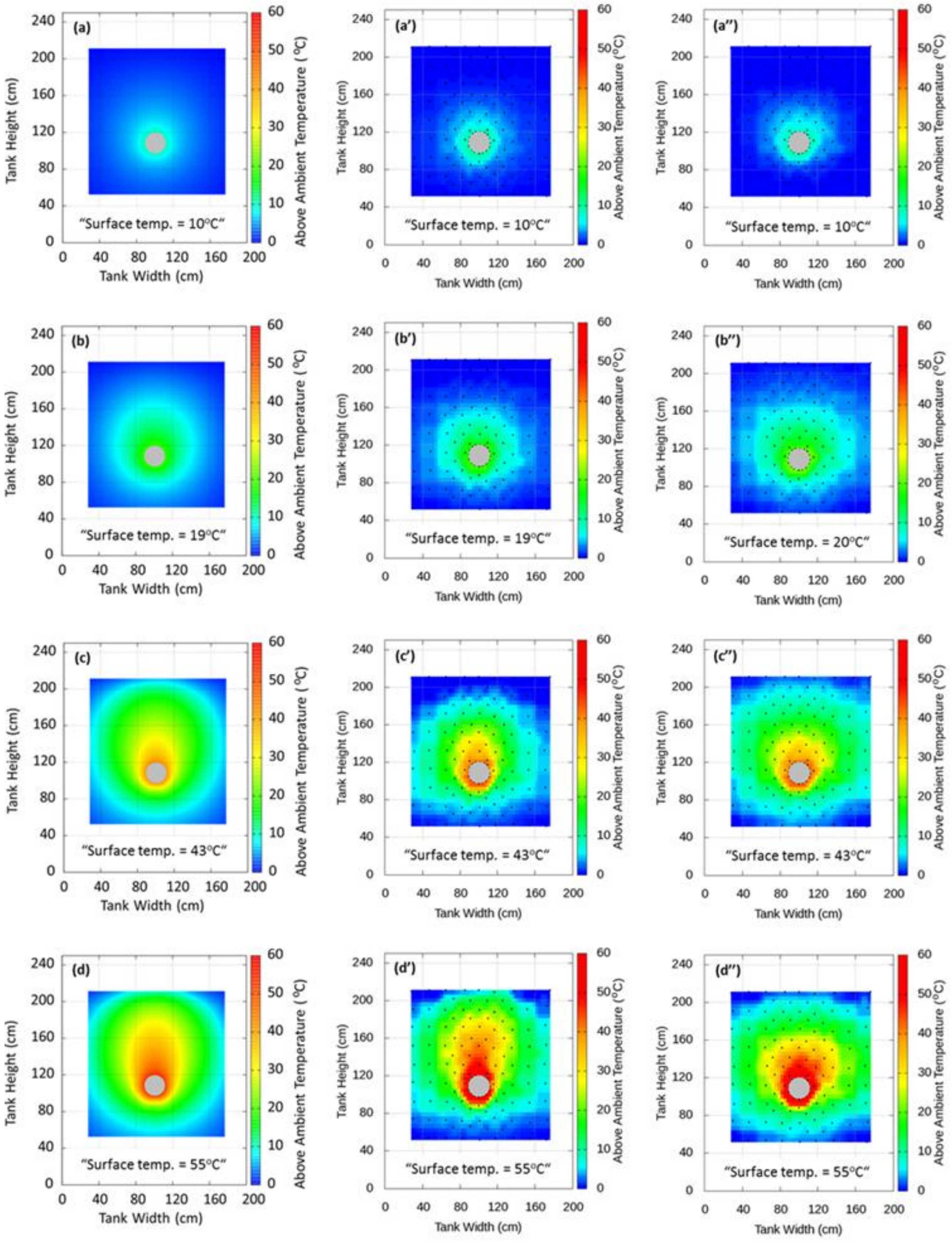

Figure 4.13: Comparison of the steady state thermal regimes from the FEM numerical modelling (a-d), ballotini (a'-d'), and natural sediments (a''- d'') large tank experiments with medium permeability (10^{-11} m^2) and varying above ambient heat source skin temperatures.

Furthermore, Figure 4.14 uses the radial steady state temperature distribution plots to compare the steady state thermal regimes for FEM numerical modelling, ballotini, and natural sediments with medium permeability and varying above ambient heat source skin temperatures. Again, in the three cases, the temperature distribution are radial with 10^{o}C skin temperature with a transition to non-radial temperature distribution at ~20^{o}C. This non-radial temperature distribution pattern spreads with increasing skin temperature. Furthermore, comparison of the standard deviation histograms plots (Figure 4.15), quantitatively shows the varying degree of scatter of the radial points for each experiment as the skin temperature increases, with 0.06 average standard deviation per temperature representing the threshold from a conductive to convective heat transfer mechanism.

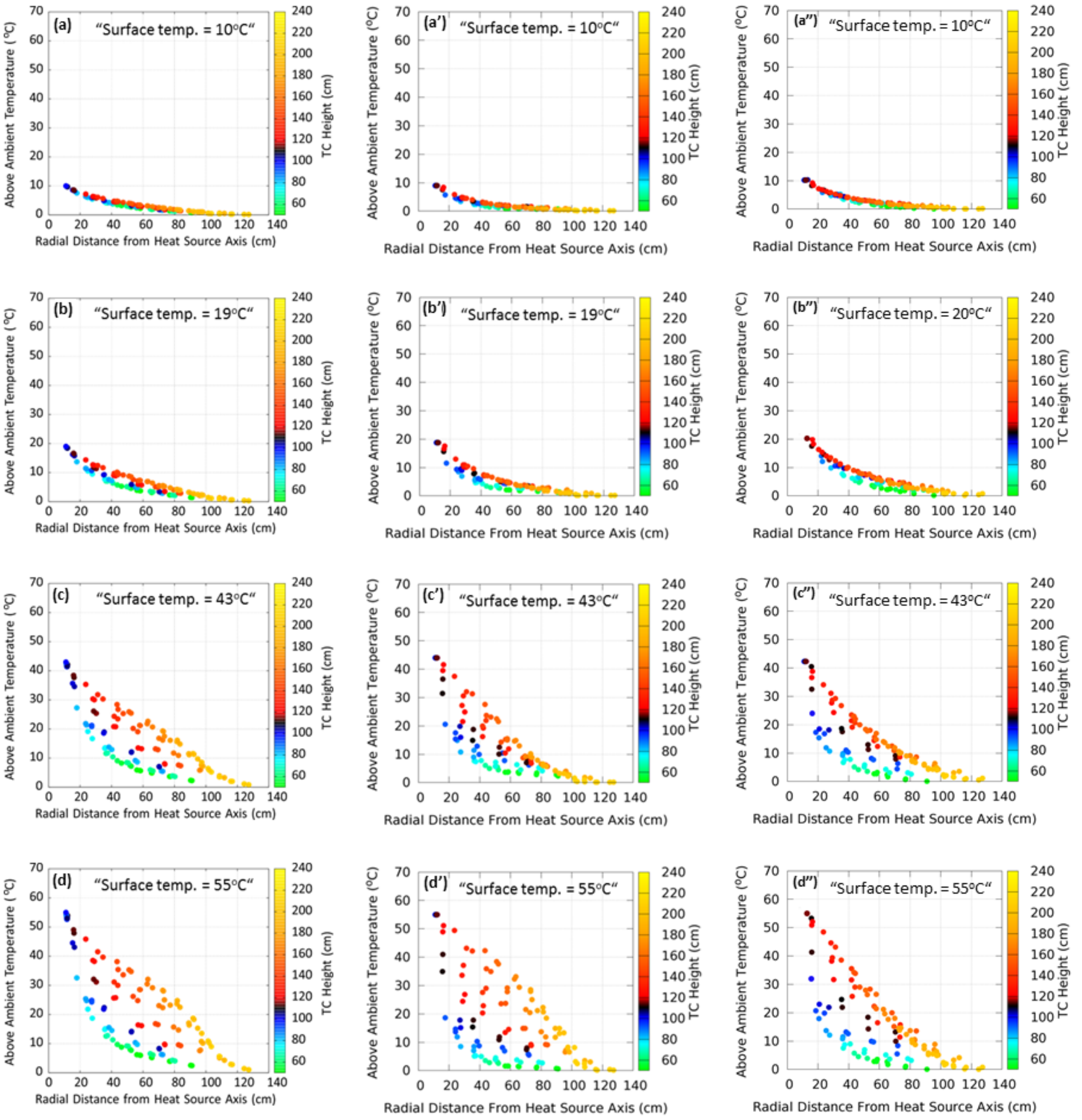

Figure 4.14: Comparison of the radial steady state temperature distributions from the FEM numerical modelling (a-d), ballotini (a'-d'), and natural sediments (a''- d'') large tank experiments with medium permeability (10^{-11} m^2) and varying above ambient heat source skin temperature.

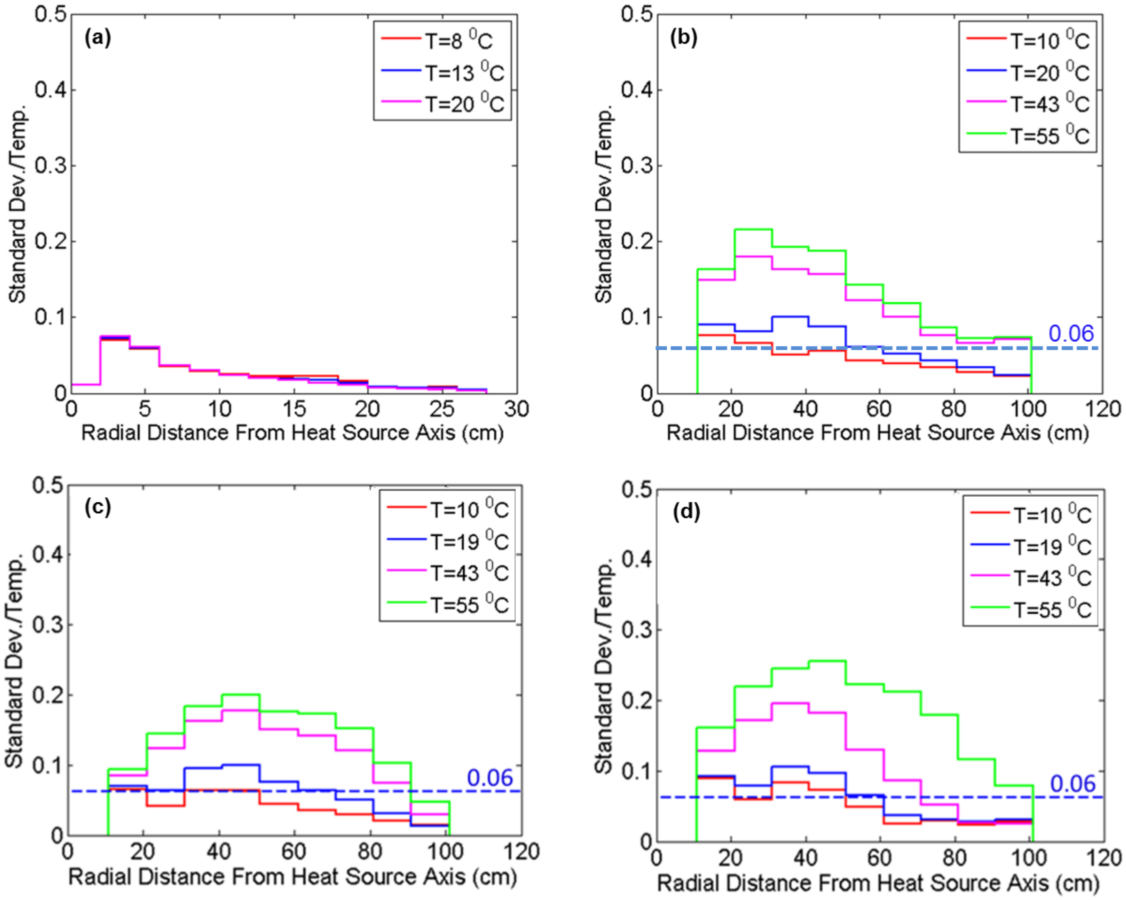

Figure 4.15: The standard deviation histograms of binned radial scatter points of the small and big tank natural sediments experiments, FEM numerical and ballotini experiments with medium permeability and varying surface temperatures. The 0.06 critical (average) standard deviation value represents the onset of radial asymmetric pattern and transition from conduction to convection heat transfer.

For the experiments using the medium permeability ballotini and natural sediments carried out in the large tank, the observed different steady state thermal regimes (Figure 4.13) with varying cable surface temperature were normalised. Subsequently the corresponding difference surfaces were generated and compared (Figure 4.16) using the method and equation described in Chapter 3, section 3.4.1. As a normalised difference of zero infers that the thermal regime shape is the same as the reference surface, thus the difference surface (Figure 4.16a and 4.16a’) for

10 ^{o}C skin temperature, shows zero normalised temperature throughout the entire surface. However, as the skin temperature exceeds ~20 ^{o}C, an area of small positive normalised temperature difference develops above the heat source (Figure 4.16b and 4.16b') and as the skin temperature of the steady state thermal regimes increases further, the positive normalised temperature difference develops even larger in size (Figure 4.16c-d and 4.16c'-d'). Thus, above the heat source with 55 ^{o}C skin temperature, it vertically extends up to 80cm height and 70 cm width for the ballotini sediments while for the natural sediments experiments, the positive normalised temperature difference extends up to 40 cm height and 90 cm width (Figure 4.16d and 4.16d').

The various comparison assessments using the steady state thermal regime maps, radial temperature plots, standard deviation histograms and normalised difference surfaces, provides a good representation of the surrounding thermal regimes of submarine HV cables buried within typical continental shelf sediments. The results from the FEM numerical models as well as the experiments with both ballotini and natural sediments are comparable – for sediment permeability of an order of magnitude ~ 10^{-11} m^{2}; conduction is the dominant heat transfer mechanism at low heat source temperatures with an onset of the convection heat flow mechanism at ~20 ^{o}C above ambient cable surface temperature. Furthermore the impact of the variability in the spherical ballotini grain shapes and more angular natural sediments are relatively small compared to the strong permeability control on the thermal regimes around the submarine HV cable, as fully investigated and presented in chapter 3 using low, medium and high permeability sediments. This is important because with a remote knowledge of the surrounding sediment permeability measurements, even to an order of magnitude level, we can more easily (even in real-time) predict and understand the current prevailing conditions of buried submarine HV cables. Consequently, the comination of modelling and analogue experimental results provide us with a very useful approach of simulating a wide range of thermal environments along various HV cable burial routes.

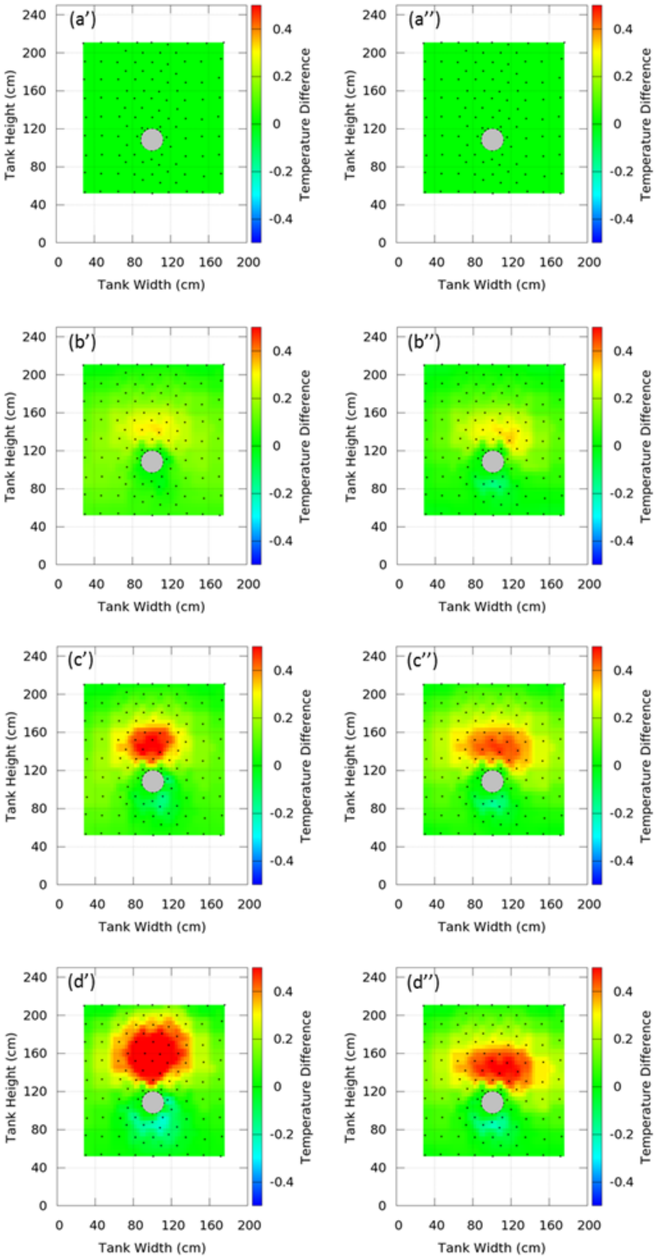

Figure 4.16: Comparison of the normalised difference plots of the varying steady state thermal regimes for medium permeability ballotini (a-d) and natural sediments (a’- d’) with varying above ambient heat source skin temperatures of (a,a’) 10 ^{o}C, (b) 19 ^{o}C, (b’) 20 ^{o}C, (c,c’) 43 ^{o}C and (d,d’) 55 ^{o}C.

4.5.3 Implication For Cable Current Rating, Ampacity and Life Span

The main source of warming on the power cable is the electrical power loss generated by flowing current through its conductor having resistance. The current carrying capacity (ampacity) of submarine HV cables is defined as the maximum current value that the cable conductor can transmit continuously without exceeding the limit temperature values of the cable components, in particular not exceeding that of the insulating material (Anders, 1997, Karahan and Kalenderli, 2011). During operation, the cable ampacity is further controlled by a balance between resistive heating within the cable and how efficiently the generated heat is lost to the surrounding environment; in order to allow the cable temperature to remain below its design temperature (Anders, 1997, Kovac *et al.*, 2006, de-Leon and Anders, 2008, Swaffield *et al.*, 2008, Karahan and Kalenderli, 2011). Therefore, it is important to determine the temperature distribution and heat flow mechanism, particularly within the adjacent sedimentary environment.

Figure 4.13, show the typical thermal regime around buried submarine HV cables and demonstrates the onset of convection heat transfer for cable buried within sediments with permeability ~10^{-11} m^2 and skin temperature greater than ~20 ^{o}C. Also chapter 3 (Emeana *et al.*, 2016) and Hughes et al. (2015), further demonstrate that for coarser sediments with medium to high permeabilities, significant convective heat transport develops even at lower cable skin temperature and generates constants pore fluid recharge below the cable (Figures 3.7 and 4.16). This colder pore fluid recharge cools the cable (Hughes *et al.*, 2015). These results are important because during convection heat flow, the high sediment permeability and buoyancy movement of the heated pore fluids due to the decreased fluid density, supports easier and more efficient transfer of the heat generated by the cable to the surrounding sediments. Thus, if the heat produced remains the same during steady state conditions and according to the principle of conservation of energy, increase in dispersed heat will result in decrease in the heat retained by the cable; therefore the cable temperature drops and the cable can transmit more current (Karahan and Kalenderli, 2011). However during conductive heat flow through the surrounding sediment with similar thermal conductivity, the generated heat is concentrated around the cable as there is no heated fluid movement and it will be difficult to disperse the heat generated by the cable. Thus, this results in an increase in the heat amount retained by the cable, the cable temperature increases and the cable current carrying capacity will drop, in order to remain below its design temperature (Tedas, 2005, Karahan and Kalenderli, 2011).

The accuracy of emergency current rating calculations are enhanced by knowledge of conductor temperature at every point at the start of emergency rating period and convective heat transfer coefficients (Anders, 1997, Anders *et al.*, 1998), which are currently overlooked in the analytical cable rating method of the IEC 60287 standard (BS-IEC-60287-1-1:2014, 2014). This limits the accuracy of the current ratings of submarine HV cable installations. Also the analytical approach of IEC 60287 standard assumes homogeneous burial environments and ambient conditions and thus is inappropriate for rating submarine HV cables buried within the continental shelf with wide variability in the surrounding sediments type, associated physical properties and as a function of depth at a specific point on the cable route.

Futhermore, submarine HV cables are exposed to thermal, electrical, and mechanical stresses simultaneously depending on applied voltage and current passing through as well as chemical changes occur in the dielectric material structure. In addition, the accelerated aging test used to define the dielectric material life span of submarine HV cables depends on the applied temperature and voltage. Thus, the cable temperature and associated thermal stresses has implications on the ageing and life span of the cables (Malik *et al.*, 1998). Thermal degradation of organic and inorganic materials used as insulation in cables occurs due to the increase in temperature above the nominal value and thus impacts on the cable life span as described by the Arrhenius equation (Pacheco *et al.*, 2000). Thus, from the results shown in Figures 3.7 and 4.16, the occurrence of convective heat flow will lead to decrease in temperature of the cables and consequently increase in their current carrying capacities. Pacheco et al. (2000) carried out several tests to verify that HV cables will last for 40 years (or other agreed material design life) if operated at 90 ^{o}C maximum temperature and concludes that HV cable life span are closely linked with their operation conditions with temperature as one of the dominant factors affecting their life (Pacheco *et al.*, 2000). The results (Figures 3.7 and 4.16) with convection heat transfer recharge will also increases the life span of submarine HV cable. Thus, it is vital to lay submarine HV cables in appropriate environmental and layout settings, and operating them in suitable working conditions, in order to increase the cable life span, efficient operation and make positive contribution to the safety and economy of the connected power systems; given their high capital cost and long asset lifetime expectancy.

4.5.4 Implication For Environments Around Submarine HV Cables

The large tank experiment results demonstrate that with skin temperature exceeding 20 ^{o}C, the heat impact of 10 ^{o}C within the surrounding medium permeability natural sand sediments reaches as far as 40 cm from the heat source (Figure 4.9 and Figure

4.13). With further skin temperature increases and as the driving heat transfer mechanism changes from conduction to convection, the heat impact of 10 ^{o}C extends vertically up to 100 cm with a heat source skin temperature of 55 ^{o}C. Figure 4.17 also demonstrates that within the top 80 cm of the conductive steady state thermal regimes, the 2^{o}C temperature contour line remains below the 20 cm depth line. However, for all the convective steady state thermal regimes, the 2^{o}C temperature contour line rises above the 20 cm depth line. Thus, the results have strong implications for the surrounding environments around submarine HV cables. Specifically, the German Federal Maritime and Hydrographic Agency (BSH), stipulates an environmental regulations of acceptable temperature limits of less than 2 K (2 ^{o}C) above ambient temperature rise at 20 cm beneath the seafloor (BSH, 2014).

Marine and benthic organisms are sensitive to even minor variations in the ambient seabed temperature (Peck, 2002, Peck, 2004) as it has serious implications for the physiological, biogeographical and evolutionary history of the benthic fauna (Barnes and Peck, 2008). For instance, the growth stage and larval development of Anomuran lithodid crabs are particularly sensitive to temperature (Anger, 2003) and the absence of brachyuran crabs in the Southern Ocean are attributed to their temperature sensitivity and inability to maintain ionic balance (Frederich, 2001). Also microbial organic matter decomposition and remineralisation processes within seabed sediments are sensitive to the ambient temperature (Pomeroy and Deibel, 1986). Furthermore, temperature is a vital abiotic factor determining the distribution of benthic organisms (Gaston, 2003) as well as benthic fauna assemblage composition, nature and diversity. Thus, this influences bioregionalisation and biogeographic range shifts (Parmesan and Yohe, 2003, Parmesan, 2006). This is because the ambient seabed temperature may affect crustacean moulting rate (Quetin, 1994), embryonic development rate (Pearse, 1991, Peck, 2006) and various locomotor activity ranges (Peck, 2002, Peck, 2004).

With dominant convective heat transport, the heated fluid movement could also impact on the physical form and nature of the sediment grains, thereby initiating granular movements, which could eventually lead to seabed erosion and exposure of the buried HV cable. In the long term, these increased sediment temperatures within the near surface, could lead to geochemical changes and diagenetic reactions between the sediments and pore fluids, leading to mineral recrystallization, compaction, and partial induration.

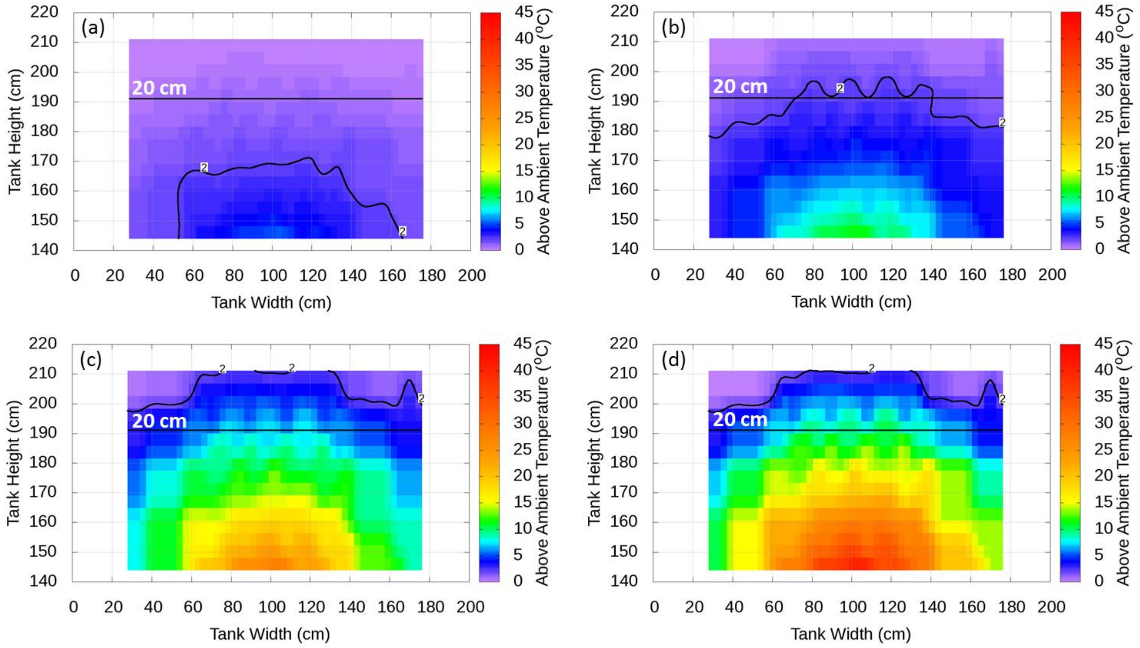

Figure 4.17: Top 80 cm steady state thermal regimes from the big tank experiments with medium permeability natural fine sand sediments. It shows the 20 cm depth mark and 2 ^{o}C contour line for the thermal regimes with varying skin temperature (a) 10 ^{o}C, (b) 20 ^{o}C, (c) 43 ^{o}C and (d) 55 ^{o}C above ambient.

4.6 Conclusion

The observed temperature measurements with medium permeability (~10^{-11} m^2) natural fine sand sediments, demonstrates that the driving heat flow mechanism around submarine HV cables buried within such environment, is conduction at 10°C above ambient skin temperature. However, convective heat flow begins as the skin temperature exceeds ~20°C for medium permeability sediments with the same thermal conductivity as convection heat flow is driven more by the existence of the increased temperature gradient and the availability of a free path for fluid movement. Also during conductive heat transfer, the heat impact of 10°C are ~40 cm from the heat source for a 20°C heat source skin temperature. However, as the skin temperature increase up to 55°C, the 10°C heat impact rises vertically up to about 100 cm. The results of the thermal regimes and associated heat flow mechanisms are comparable as demonstrated by the FEM numerical models and physical models with artificial ballotini and natural sediments. Thus, the impact of the variability in the spherical ballotini grain shapes and more angular natural sediments are small compared to the strong permeability control on the thermal regimes around submarine HV cable.

The results have several implications as the occurrence of convection heat flow will lead to decrease in cable temperature and consequently increase in the cable current carrying capacities and life span. The IEC 60287 standard currently assumes only conduction heat flow and thus the results will have implications on cable rating accuracy. Furthermore, the surrounding physical, geochemical and biological environments around submarine HV cables will be impacted by the increased temperature within the sediments.

5

Subsea HV Cable Thermal Regime: Controlling Thermal Properties

5.1 Introduction

Thermal conductivity of the surrounding sediments is a vital parameter in the use of the IEC 60287 (BS-IEC-60287-1-1:2014, 2014) standard for analytically evaluating the current rating of buried submarine HV cable. However, there is poor understanding of the relationship between the thermal properties of marine sediments and the current that may be reliably carried by submarine HV cables. The current IEC 60287 standard assumes amongst others; homogeneous burial sediments and a simple model for the thermal resistance (conductivity) of the surrounding sediments. Also understanding the sediment thermal properties around buried HV cable gives further insights of the cable heat impacts on surrounding near surface benthic organisms and sedimentary environments.

This chapter is aimed at evaluating the thermal properties controlling the observed conductive thermal regimes (presented in chapter 3) using the acquired temperature time series data from seven lab experiments with coarse silt and fine sand ballotini sediments as well as two experiments with fine sand natural sediments (presented in chapter 4).

5.2 Methods

5.2.1 Nodal Network

The nodal points are designated by a numbering scheme that, for a two-dimensional system, may take the form shown in Figure 5.1b. The x and y locations are designated by the m and n indices, respectively (for more details, see chapter 2). For the analysis and results presented in section 5.3, a nodal network developed for each dataset from the big tank ballotini experiments involves a total of 289 nodes of 5cm x 5cm spacing covering up to 50cm radial distance away from the centre (node 145) of the heat source. Similarly, for the pilot natural experiments, the nodal network involves 361 nodes of 1cm x 1cm spacing covering upto 14cm radial distance from the centre (node 181) of the heat source (Figure 5.2)

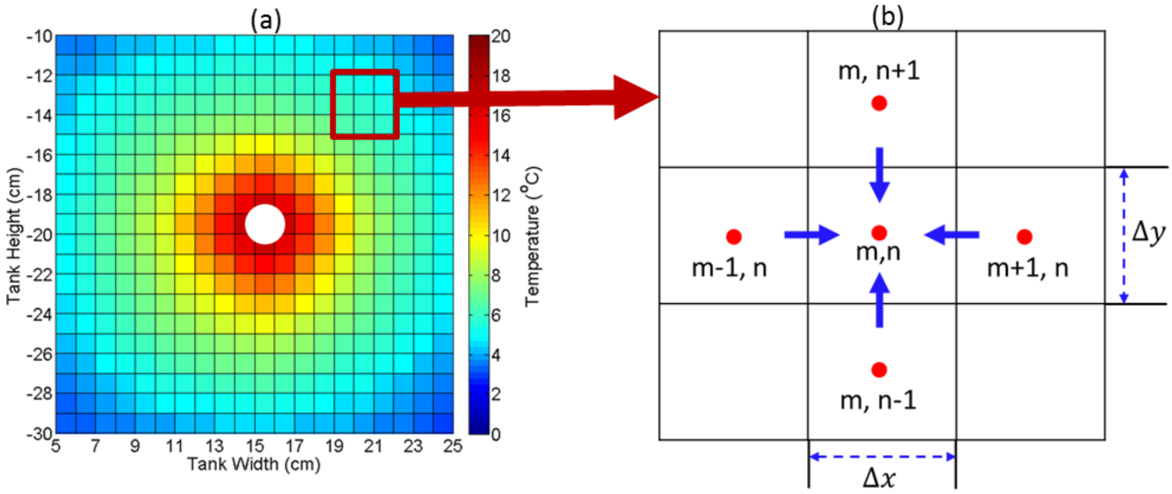

Figure 5.1: Two-dimensional heat conduction nodal network through the pilot natural fine sand sediments with 20 °C above ambient heat source and (b) conduction to an interior node from its neighbouring nodes used for explicit finite difference heat equation discretization.

19	38	57	76	95	114	133	152	171	190	209	228	247	266	285	304	323	342	361
18	37	56	75	94	113	132	151	170	189	208	227	246	265	284	303	322	341	360
17	36	55	74	93	112	131	150	169	188	207	226	245	264	283	302	321	340	359
16	35	54	73	92	111	130	149	168	187	206	225	244	263	282	301	320	339	358
15	34	53	72	91	110	129	148	167	186	205	224	243	262	281	300	319	338	357
14	33	52	71	90	109	128	147	166	185	204	223	242	261	280	299	318	337	356
13	32	51	70	89	108	127	146	165	184	203	222	241	260	279	298	317	336	355
12	31	50	69	88	107	126	145	164	183	202	221	240	259	278	297	316	335	354
11	30	49	68	87	106	125	144	163	182	201	220	239	258	277	296	315	334	353
10	29	48	67	86	105	124	143	162	181	200	219	238	257	276	295	314	333	352
9	28	47	66	85	104	123	142	161	180	199	218	237	256	275	294	313	332	351
8	27	46	65	84	103	122	141	160	179	198	217	236	255	274	293	312	331	350
7	26	45	64	83	102	121	140	159	178	197	216	235	254	273	292	311	330	349
6	25	44	63	82	101	120	139	158	177	196	215	234	253	272	291	310	329	348
5	24	43	62	81	100	119	138	157	176	195	214	233	252	271	290	309	328	347
4	23	42	61	80	99	118	137	156	175	194	213	232	251	270	289	308	327	346
3	22	41	60	79	98	117	136	155	174	193	212	231	250	269	288	307	326	345
2	21	40	59	78	97	116	135	154	173	192	211	230	249	268	287	306	325	344
1	20	39	58	77	96	115	134	153	172	191	210	229	248	267	286	305	324	343

Figure 5.2: Nodal network showing the 361 grid locations number with 1cm x 1cm spacing used for the pilot natural sediments data analysis. The radial distance of all grid locations are computed from grid location 181 (centre of the heat source).

5.2.2 Heat Diffusion Equation

In a homogeneous medium with constant thermal conductivity and temperature gradients, equation (5.2) is the explicit form of the finite-difference expression of the heat diffusion equation (5.1) and provides the variation of temperature with both time and spatial coordinates. Thus, the thermal diffusivity (α) were estimated taking into account the temperature distribution from the neighbouring x and y nodes (for more details, see chapter 2).

$$\frac{1}{\alpha}\frac{\partial T}{\partial t} = \frac{\partial^2 T}{\partial x^2} + \frac{\partial^2 T}{\partial y^2} \tag{5.1}$$

$$\frac{1}{\alpha}\frac{T_{m,n}^{p+1} - T_{m,n}^{P-1}}{\Delta t} = \frac{T_{m+1,n}^{p} + T_{m-1,n}^{P} - 2T_{m,n}^{p}}{(\Delta x)^2} + \frac{T_{m,n+1}^{p} + T_{m,n-1}^{P} - 2T_{m,n}^{p}}{(\Delta y)^2} \tag{5.2}$$

Where m and n subscripts are used to designate the x and y locations of discrete nodal points. The superscript p were used to denote the time dependence of T, and the time derivative are expressed in terms of the difference in temperatures associated with the new $(p+1)$ and previous (p) times. Calculations were performed at successive times separated by the interval Δt, as well as at discrete points in both spatial directions $(\Delta x, \Delta y)$. Hence, the developed explicit finite difference approach (equation 5.2) was applied to the acquired temperature time series data to estimate the sediment thermal diffusivity. Also thermal conductivity (λ), were estimated using equation 5.3, which is a function of the volumetric heat capacity (product of density (ρ) and specific heat capacity (C_p)) and thermal diffusivity (α).

$$\alpha = \frac{\lambda}{\rho C_p} \qquad (5.3)$$

5.3 Results

The various thermal properties governing equations described in section 5.2 are adapted to seven temperature time series datasets acquired with varied heat source surface temperatures buried within the coarse silt and fine sand ballotini sediments as well as two pilot experiments with fine sand natural sediments. The results presented in this section are the subsequent estimates of the sediments thermal diffusivity, volumetric heat capacity and thermal conductivity as the heat flows through these sediments.

5.3.1 Thermal Diffusivity Calculation

Quantitatively, the speed at which the temperature front propagates though the sediments (thermal diffusivity, α), calculated using 3D heat flow cubes from the start to the steady state time stamp of each observed temperature time series data. For the pilot natural sediment temperature time series analysis with nodal network spacing of 1cm x 1cm; 0.01m spacing interval $(\Delta x, \Delta y)$ were applied and 0.05m for the big tank ballotini data analysis because its nodal network spacing is 5 cm x 5 cm. A time interval (Δt) of 120 seconds were used throughout the analysis of both observed datasets from the pilot natural and ballotini sediments experiments. Then at each node the temperature change with time $(\frac{\partial T}{\partial t})$ and distance profile $(\frac{\partial^2 T}{\partial x^2} + \frac{\partial^2 T}{\partial y^2})$ in the x and y direction were computed based on equation 5.2. Thus the $\boldsymbol{\alpha}$ estimates are computed from the slope of the best fit line through the plot of the temperature change with time $(\frac{\partial T}{\partial t})$ against the spatial temperature change $(\frac{\partial^2 T}{\partial x^2} + \frac{\partial^2 T}{\partial y^2})$ (Figure 5.3).

Subsequently, the same procedure was applied to two pilot fine sand natural experiments with above ambient heat source temperature of 13 °C and 20 °C. Similarly, for the seven conductive heat flow experiments using coarse silt ballotini sediments with varying cable surface temperature of 10 °C, 18 °C, 45 °C and 60 °C above ambient and fine sand ballotini with 10 °C, 19 °C (initial) and 19 °C (replica) above ambient. The respective thermal diffusivities are computed at various nodes as described in figure 5.4 and 5.5.

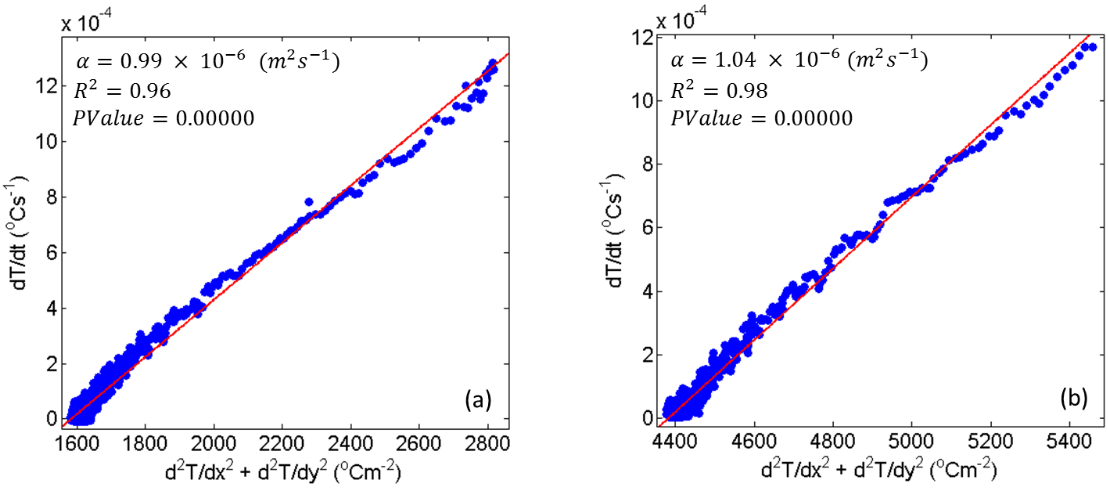

Figure 5.3: Thermal diffusivity calculation scatter plot for the pilot natural sediments at (a) node 5 and (b) node 100 with 20 °C above ambient cable surface temperature.

Figures 5.3 shows the typical plots used to estimate α for all observed datasets using the heat diffusion equation (equation 5.1, 5.5). The slope of the fitted red line to the observations gives the $\boldsymbol{\alpha}$ estimate at the various nodes. The correlation coefficient (R^2) of 0.96 (Figure 5.3a) and 0.98 (Figure 5.3b) as well as a zero p-value, shows that the estimates are statistically significant at the 95% confidence level. The same approach and analysis were carried out to calculate the thermal diffusivity for the fine sand pilot natural sediments (Figure 5.4a,b), coarse silt ballotini

(Figure 5.5a) and fine sand ballotini (Figure 5.5b) sediments experiments with varying input heat. Similarly, all the respective α estimates are significant at the 95% confidence level.

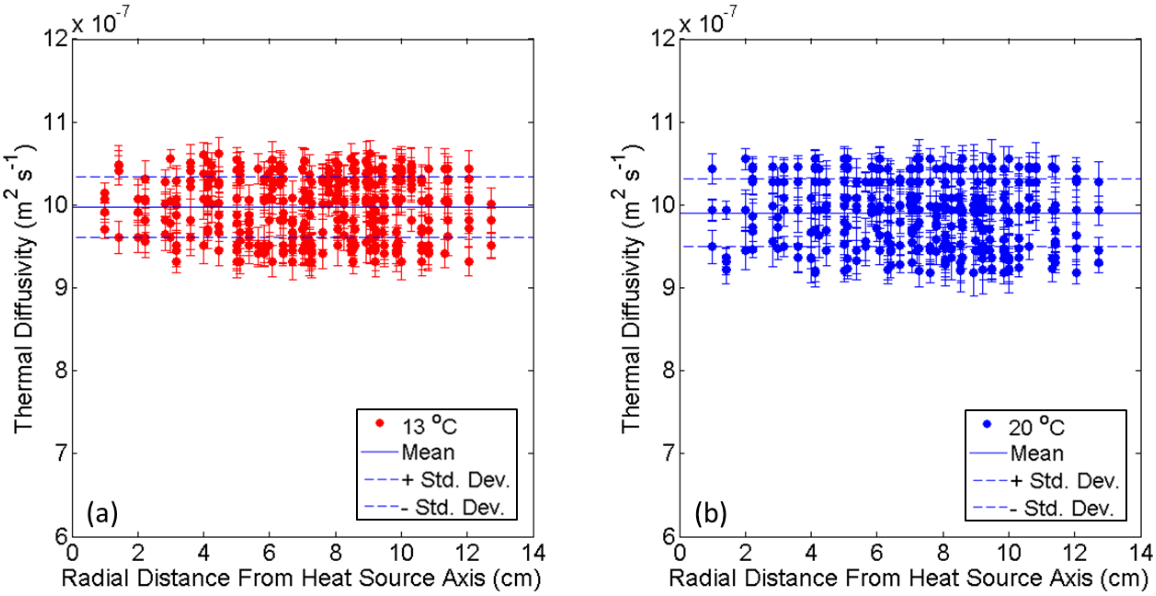

Figure 5.4: Thermal diffusivity estimates for fine sand natural sediments with (a) 13 °C and (b) 20 °C cable surface temperature.

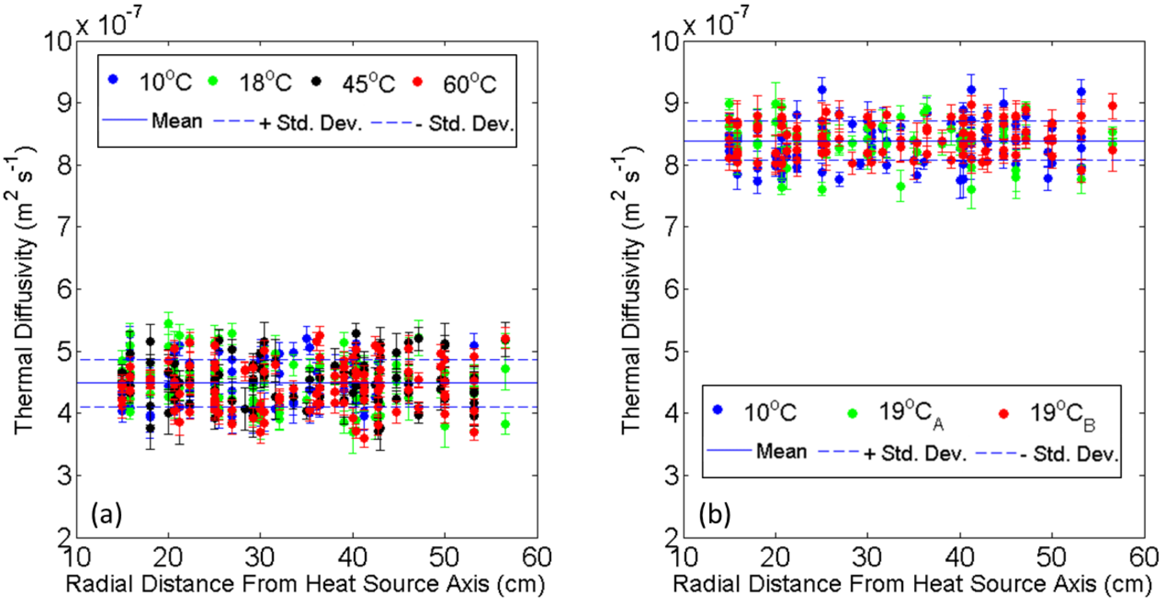

Figure 5.5: Combined thermal diffusivity estimates for (a) coarse silt and (b) fine sand ballotini sediments with varying cable surface temperature.

Figure 5.4a and 5.4b demonstrates that for the fine sand natural sediments, the thermal diffusivity estimates are similar irrespective of the changing cable surface input heat and nodal locations; and gives a mean thermal diffusivity estimate of 0.99 ± 0.04 x 10^{-6} m^2s^{-1}. This is also similar for the fine sand ballotini sediments (Figure 5.5b) with a mean thermal diffusivity estimate of 0.84 ± 0.03 x 10^{-6} m^2s^{-1}. For the coarse silt ballotini sediments (Figure 5.5a) the mean thermal diffusivity estimate is 0.45 ± 0.04 x 10^{-6} m^2s^{-1}. The uncertainty in all thermal diffusivity estimates from the standard error of the slopes of the fitted curves (Figure 5.4 and 5.5) are shown by thin vertical lines. These results are in agreement with previously published estimates for muddy and sandy sediments (Harrison, 1985, Harrison and Phizacklea, 1985, Vugts and Zimmerman, 1985, Piccolo *et al.*, 1993, Wheatcroft *et al.*, 2007, Kim *et al.*, 2007, Thomson, 2010).

5.3.2 Volumetric Heat Capacity Calculation

In order to estimate C_v of the fine sand natural sediments, coarse silt and fine sand ballotini samples, equation (5.4) was used. The C_v estimate is expressed as the weighted sum of the heat capacities of the ballotini constituents (Campbell, 1985, Campbell and Norman, 1998).

$$C_v = \rho_s C_s V_s + \rho_f C_f V_f \tag{5.4}$$

Where ρ_s and ρ_f are density of solid and fluid respectively; C_s and C_f are specific heat capacity of solid and fluid respectively while V_s and V_f are volume fractions of solid and fluid respectively.

The fluid volume fraction was estimated using the measured sediment porosity. The ballotini particle densities and specific heat capacity are 2.50 gcm^{-3} and 1.172 Jg^{-1}K^{-1} 2.66 gcm^{-3} (Potters-Ballotini, 2011) while the corresponding natural sediments values are 2.66 gcm^{-3} and 1.096 Jg^{-1}K^{-1} (Cornish-Lime, 2011) used to compute their respective volumetric heat capacities (Table 5.1). With variability of the measured porosity estimates for the fine sand natural sediments, coarse silt and fine sand ballotini, their corresponding estimated average C_v are: 3.39 $\pm$ 0.08 x 10^6 Jm^{-3} K^{-1}, 3.18 $\pm$ 0.06 x 10^6 Jm^{-3} K^{-1} and 3.33 $\pm$ 0.08 x 10^6 Jm^{-3} K^{-1} respectively.

Table 5.1: Volumetric heat capacity estimation for ballotini and natural sediments

Sediments	**Sediment Density (gcm^{-3})**	**Sediment Specific Heat Capacity, ($Jg^{-1}\ K^{-1}$)**	**Sediment Volume Fraction**	**Water Density (gcm^{-3})**	**Water Specific Heat Capacity, ($Jg^{-1}\ K^{-1}$)**	**Water Volume Fraction**	**Volumetric Heat Capacity, ($10^6\ Jm^{-3}\ K^{-1}$)**
Ballotini Coarse Silt	2.50	1.172	0.85	0.998	4.20	0.15	3.119
	2.50	1.172	0.80	0.998	4.20	0.20	3.182
	2.50	1.172	0.75	0.998	4.20	0.25	3.245
Ballotini Fine Sand	2.50	1.172	0.74	0.998	4.20	0.26	3.258
	2.50	1.172	0.68	0.998	4.20	0.32	3.334
	2.50	1.172	0.62	0.998	4.20	0.38	3.409
Natural Fine Sand	2.66	1.096	0.69	0.998	4.20	0.31	3.311
	2.66	1.096	0.63	0.998	4.20	0.37	3.388
	2.66	1.096	0.57	0.998	4.20	0.43	3.464

5.3.3 Thermal Conductivity Calculation

The thermal conductivity of the natural fine sand sediments, coarse silt and fine sand ballotini sediment was calculated using equation (5.3) with the estimated average results of C_v and α described in section 5.3.1 and 5.3.2 respectively. Figure 5.6a and 5.6b demonstrates that for the fine sand natural sediments, the thermal conductivity estimates are similar irrespective of the changing cable surface input heat and nodal location; giving a mean thermal conductivity estimate of 3.29 ± 0.15 Wm^{-1}K^{-1}. Similarly, for the fine sand ballotini (Figure 5.7b), it gives a mean thermal conductivity estimate of 2.79 ± 0.11 Wm^{-1}K^{-1} and 1.43 ± 0.12 Wm^{-1}K^{-1} for the coarse silt ballotini sediments (Figure 5.7a). Uncertainty in the thermal conductivity estimates (E), shown by thin vertical lines, are due to the associated errors from the thermal diffusivity estimates (E_1) shown in Figure 5.5 and volumetric heat capacity estimates (E_2) resulting from the standard deviation of sediment porosity measurements (Figure 5.6 and 5.7). Thus equation 5.5, was used to estimate the propagated combined errors (E), where E_1 and E_2 are the fractional error in the component terms.

$$E^2 = E_1^2 + E_2^2 \tag{5.5}$$

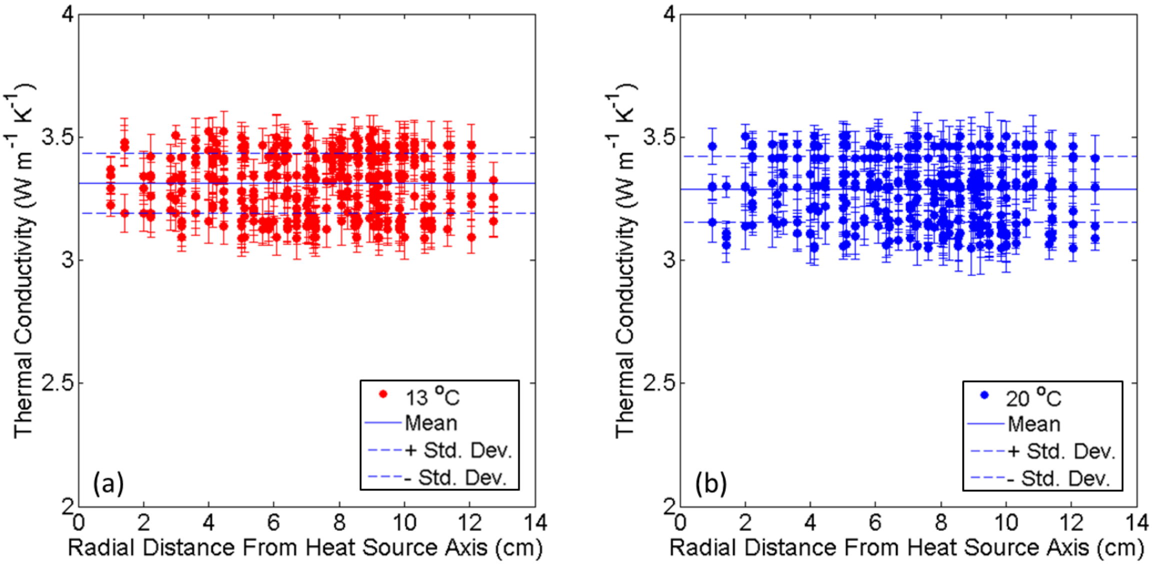

Figure 5.6: Thermal conductivity estimates for fine sand natural sediments with (a) 13 °C and (b) 20 °C cable surface temperature.

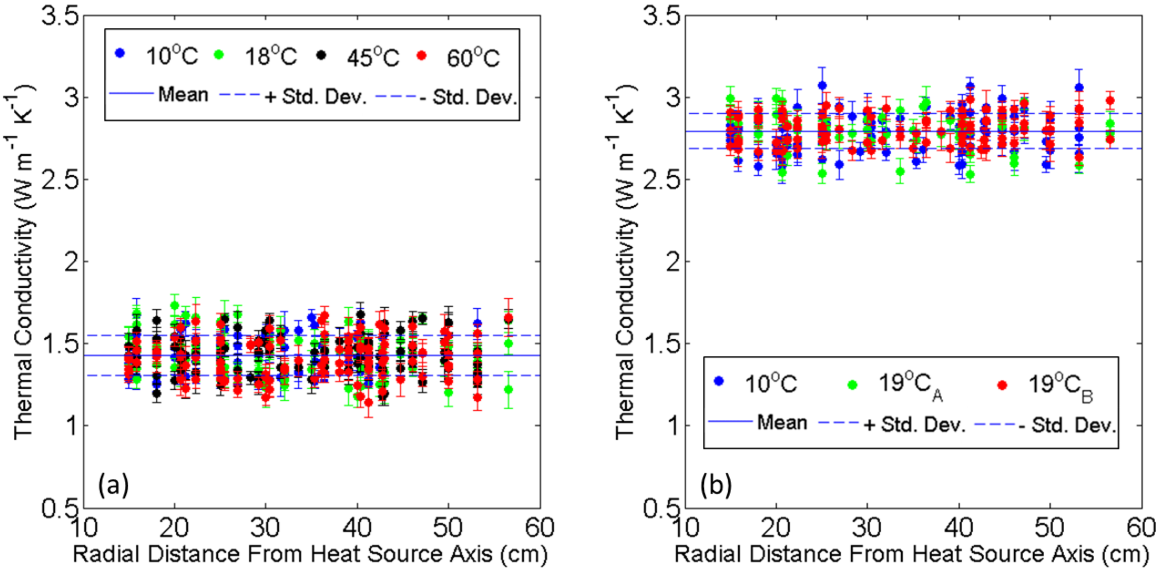

Figure 5.7: Combined thermal conductivity estimates for (a) coarse silt and (b) fine sand ballotini sediments with varying cable surface temperature.

5.4 Discussion

The estimated average sediment thermal properties from the temperature time series measurements acquired during the transient heat transfer phase for the different sediments (coarse silt ballotini, fine sand ballotini and fine sand natural sediments) are summarised in Table 5.2. These estimates are also comparable to previous published values for both mud (coarse silt) and sand sediments as demonstrated in Figure 5.8, which synthesises the published estimates (See Chapter 2, Section 2.4.5) of thermal properties of near surface marine sediments, particularly within the shallow (0 to 1m) sub-seabed.

Table 5.2: Summary of the average thermal properties estimates for ballotini (coarse silt and fine sand) and natural sediments (fine sand).

Sediment thermal Properties	**Coarse Silt (Ballotini)**	**Fine Sand (Ballotini)**	**Fine Sand (Natural Sediments)**
Thermal Conductivity ($Wm^{-1} K^{-1}$)	1.43 ± 0.12	2.79 ± 0.11	3.29 ± 0.15
Thermal Diffusivity 10^{-6} ($m^2 s^{-1}$)	0.45 ± 0.04	0.84 ± 0.03	0.99 ± 0.04
Volumetric Heat Capacity 10^6 ($Jm^{-3} K^{-1}$)	3.18 ± 0.06	3.33 ± 0.08	3.39 ± 0.08

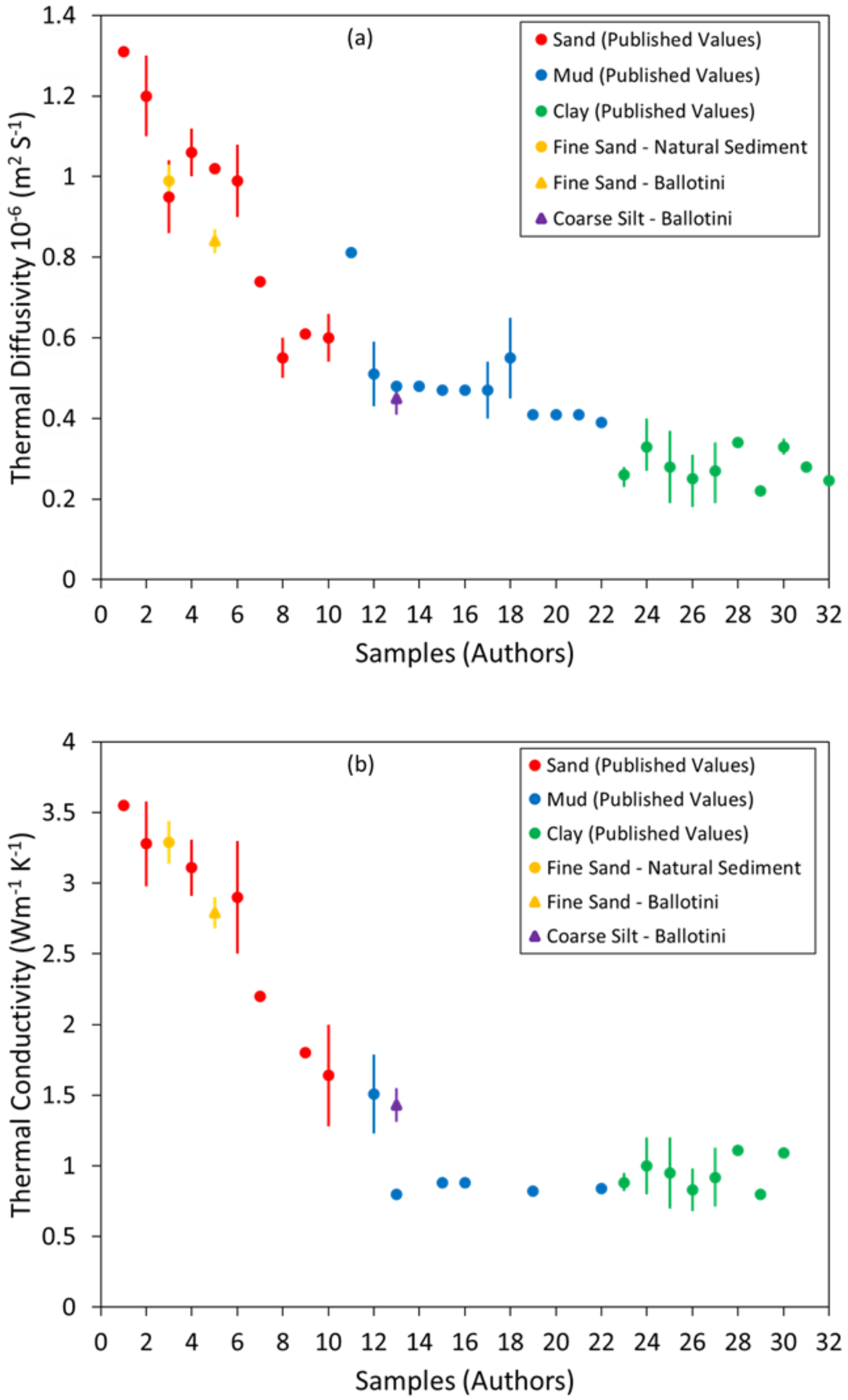

Figure 5.8: Ballotini and natural sediments thermal diffusivity (a) and conductivity (b) estimates compared with published estimates of thermal properties of near surface (0 to 1m) marine sediments. It shows variability of sediment thermal properties with changing lithology/grain size. More details of each research (32 authors) are presented in Chapter 2, Tables 2.1 to 2.3. The thin vertical lines show the uncertainties in thermal diffusivity and conductivity estimates.

The results (Table 5.2 and Figure 5.8) shows that there is a clear variation in thermal diffusivity and conductivity within different sediment types; sandy (fine sands) sediments are approximately twice more effective at diffusing heat than muddy (coarse silts) sediments. The heating effects away from the heat source (HV cables) buried around sandy sediments will uptake heat more rapidly than when buried around muddy sediments.

The maximum cable current carrying capacity (cable ampacity) are closely linked with the thermal conductivity of the surrounding burial environment. Thus, the heat generated from submarine HV cables buried in sandy sediments (with higher thermal conductivity) will be rapidly transmitted to the surrounding environments, results in reduced cable temperature and subsequently allows more current to be transmitted through the cable. However for cables buried in muddy sediments with relatively lower thermal conductivity, the transfer will be relatively slower, leading to increased cable temperature and subsequently, causes reduction in the cable current ampacity.

Furthermore, the determination of actual value of the current ratings of buried HV cables are dependent on many different factors, which includes a very key factor - the thermal properties of the surrounding sediments. Thus, the marked variability in the thermal properties associated with different marine sediment types (Table 5.2 and Figure 5.8) will have huge implications on the current rating of submarine HV cables, particularly with regards to the analytical current ratings approach of the IEC 60287 standard that assumes homogeneous burial environments.

Page intentionally left blank.

6

Conclusions

6.1 Overview

The overriding purpose of this research was to determine the thermal regimes and heat transport mechanisms around submarine HV cables buried within the wide range of sediments found on the continental shelf. To accomplish this goal it became necessary to reach some prerequisite objectives. Understand the various sediment heat transfer mechanisms – conduction and convection, their governing equations and conditions of occurrence; and associated control of temperature and sediment properties; through a review of existing literature conducted for this dissertation (Chapter 2).

Following this, it was necessary to construct and operate uniquely designed laboratory experiments for further detailed investigation of this goal. To do this, a custom made heat source and experimental tank was designed and constructed. Figure A1 and A2 (Appendix), shows the design and photographs of this significant piece of laboratory equipment which was also a significant part of the PhD research.

Once these fundamental objectives and first steps were achieved, the research was then able to proceed. This conclusion Chapter presents the summaries and recommendations that resulted from the subsequent research studies (Chapter 3, 4 and 5) carried out. The research studies involved analysing both the steady and transient heat transfer phases of the surrounding temperature time series measurements acquired from 2D laboratory experiments specifically designed as an analogue to a buried submarine HV cable using both artificial (Ballotini) and natural sediments. The results provided clear understanding of how the surrounding thermal regimes, heat transport mechanisms and sediment thermal properties around buried submarine HV cable may vary with a range of typical shelf sediments of different permeability classes.

(a) Low permeability (~ 10^{-13} m^2) burial thermal environments

The results of a series of steady state heat flow experiments and numerical modelling suggest that, for submarine HV cables with surface temperatures up to 60°C above ambient and buried within clays to coarse silts with low permeability up to ~ 10^{-13} m^2, the surrounding thermal regime and mode of heat transfer will be dominantly conductive. The radial temperature distribution of 10 – 60 °C in the surrounding sediments are only within a 40 cm radius of the cable, with an exponential decrease in the thermal gradient. The estimated average thermal diffusivity and conductivity are $0.45 \pm 0.04 \times 10^{-6}$ m^2s^{-1} and 1.43 ± 0.12 $Wm^{-1}K^{-1}$ respectively.

(b) Medium permeability (~10^{-11} m^2) burial thermal environment

Steady state heat flow experimental and numerical modelling results shows that fine sands with medium permeability ~10^{-11} m^2 are a transitional environment. The heat flow mechanism are conductive at low cable surface temperatures (c. < 20^{o}C) and changes to convective mode, as the cable surface temperatures increase above ~20°C relative to ambient. The radial temperature distribution of 10 – 20 °C in the surrounding sediments for cables with surface temperature of up to ~20°C are also only within a 40 cm radius of the cable. However, high asymmetric temperatures (10 - 55 °C) are observed up to 1 m above the cable for cables with surface temperatures of 55^{o}C, with an exponential decrease in the thermal gradient. The analysed conductive transient heat flow measurements shows that the average thermal diffusivity and conductivity are $0.84 \pm 0.03 \times 10^{-6}$ m^{2}s^{-1} and 2.79 ± 0.11 Wm^{-1}K^{-1} respectively.

(c) High permeability (~10^{-9} m^{2}) burial thermal environment

In very coarse sands with high permeability ~10^{-9} m^{2}, the steady state heat flow results from both experimental and numerical modelling, shows that convective heat transfer occurs even at skin temperatures as low as 7°C above ambient. Significantly high asymmetric temperature distribution of 10 - 18 ^{o}C in the surrounding sediments are heated over distances exceeding the typical 1 m cable burial depth with 18 ^{o}C surface temperature.

(d) Natural sediment burial thermal environment with medium permeability (~10^{-11} m^{2})

Presented in Chapter 4 are additional steady state heat flow experiments using natural sediments with medium permeability ~10^{-11} m^{2}, in order to assess the applicability of the results of Chapter 3 to natural settings. Comparison assessments of corresponding numerical and physical modelling with both ballotini (Emeana *et al.*, 2016) and natural sediments, shows that with varying cable surface temperatures, the heat flow mechanism are also transitional, with the conduction to convection change still occurring at ~20°C above ambient. Also the analysed conductive transient heat flow measurements shows that the average thermal diffusivity and conductivity are $0.99 \pm 0.04 \times 10^{-6}$ m^2s^{-1} and 3.29 ± 0.15 $Wm^{-1}K^{-1}$ respectively. Thus, for both homogeneous Ballotini and Natural surrounding burial sediments with similar permeability ~10^{-11} m^2, the impact of their varying grain shapes (spherical ballotini and angular natural sediments) are small compared to the strong permeability control on the thermal regimes around submarine HV cable (Emeana *et al.*, 2016), as clearly demonstrated in Chapter 3.

6.2 Research contributions

A major contribution of the research presented in this thesis, is that both conduction and convection mechanism operate around submarine HV cables, buried in varying continental shelf sediments, to dissipate the generated heat. The dominant mode depends on the cable surface temperature and permeability of the surrounding sediments, as summarized above. This insight is contrary to the assumptions and predictions of the existing IEC 60287 standard and possesses several implications for the current rating and ampacity, cable insulation and life-span, manufacturing costs, burial approaches and route plans of submarine HV cables. In addition, there are several implications for the surrounding sedimentary environments.

(a) Cable current rating and ampacity

The occurrence of convective heat transfer within high permeability sediments would allow more efficient heat transfer to the surrounding sediments. Coupled with the artificial cooling effect of convection recharge, results to decreased cable temperatures (Table 6.1). This would allow raising the cable current ratings and ampacity limit for increased current transmission capacity whilst remaining below its design temperature. The predicted surface temperature (Table 6.1) was calculated based on the assumption that the maximum operating conductor temperature of submarine AC HV cables with XLPE insulation is 90^{o}C and translates to cable surface temperatures of 70^{o}C (Swaffield *et al.*, 2008, Hughes *et al.*, 2015).

Table 6.1: Predicted conductor and surface cable temperatures for different solid thermal conductivities and burial depths from the IEC standard and FEM modelled results using sediments permeabilities of 10^{-12} m^{2} $(\mathbf{k_1})$ and 10^{-10} m^{2} $(\mathbf{k_2})$, (Modified from Hughes et al. 2015).

Solid Thermal Conductivity, λ_s (Wm^{-1}K^{-1})	Burial Depth (m)	Predicted Conductor Temperatures (^{o}C)			Predicted Surface Temperatures (^{o}C)		
		IEC, k_1	FEM k_1	FEM k_2	IEC, k_1	FEM k_1	FEM k_2
1	0.5	69.2	71.3	55.1	53.8	55.5	42.9
2	0.5	51.5	53.5	49.3	40.1	41.6	38.3
3	0.5	44.2	46.1	44.7	34.4	35.9	34.8
1	1	82.5	84.2	54.5	64.2	65.5	42.4
2	1	59.2	61.1	50.6	46.0	47.5	39.4
3	1	49.7	51.5	47.3	38.7	40.1	36.8
1	2	95.7	97.1	53.9	74.4	75.5	41.9
2	2	66.9	68.7	50.4	52.0	53.4	39.2
3	2	55.1	56.9	47.9	42.9	44.3	37.3
1	5	113.0	113.6	53.2	87.9	88.4	41.4
2	5	77.0	79.3	49.8	59.9	61.7	38.7
3	5	62.2	64.4	47.7	48.4	50.1	37.1

(b) Cable insulation and life-span

The reduced cable temperature resulting from significant convection heat transfer and the operation of cables below their design temperature limits will decrease the thermal degradation rate of HV cable insulation. This would also increase the cable life span (Pacheco *et al.,* 2000) because the accelerated aging and life span of dielectric insulation material of cables depends on cable temperature.

(c) Cable manufacturing costs

The temperature within HV cables and its conductor(s) cross-sectional area are inversely related. Thus HV cables buried in convective sediments with higher heat dissipation rate and resultant cooler cable temperature would require a reduced conductor cross-sectional area to transmit a given amount of current. This will lead to reduced manufacturing cost of sections or entire cable link. Thus, it’s important to take into account the above stated implications of convection heat transfer during the design and manufacturing stage of submarine cables.

(d) Cable burial approaches and route plan

Continental shelf sediments are widely variable and dynamic along a typical cable route (van Landeghem *et al.,* 2014) and submarine cable burial depth can change by up to approximately 5 m within less than a year (Mole et. al., 1997). However, submarine cables are currently buried with little knowledge/consideration of the surrounding burial sediments and their impacts. Results from Hughes *et al.,* 2015 shows that burial depth of submarine cables can also influence their thermal state. Also as outline earlier, there are massive contributions and benefits for cables buried along convective sediments. Thus, it’s important to consider the surrounding seabed dynamic nature and sediment types/properties during the cable route planning phase. Though it may be relatively costly initially, but could later prove cost effective, if during cable burial operations, high permeable convective sediments are artificially introduced and buried together with HV cable along the entire cable route. Alternatively and where possible, alter the planned cable route to follow seabed sections with higher permeable sediments.

(e) Varying surrounding thermal conductivity

Each HV cable has an estimated current rating that stipulates the maximum amount of current that can be safely transmitted to allow HV cable remain below its temperature limit and avoid damaging its insulating components. The IEC 60287 standard approach for calculating this current rating involves estimating the thermal conductivity of the surrounding sediments and assumes homogenous burial sediments along cable routes. However, continental shelf sediments are variable with corresponding marked variability in their sediment thermal properties, as shown in Chapter 5. Sediment thermal conductivities are about twice as high for sand than for mud. Thus, the IEC 60287 standard may not be appropriate for rating cables buried within marine sediments and could be significantly underrating submarine HV cables. This will also have further allied implications on the ampacity and insulating materials degradation rates of HV cables.

(f) Surrounding biological and geological changes

Over 1 m above the heat source, the surrounding sediments temperature for convective sediments are up to ~10 °C above ambient. This clearly exceeds the 2 °C threshold at 20 cm burial depth stipulated by the environmental regulations of the German Federal Maritime and Hydrographic Agency (BSH). Also this anomalous high temperatures means sediments will endure temperature conditions typically reached at ~ 2.8 km burial under normal geothermal gradients. Thus, benthic organisms which are sensitive to even minor variations in the ambient seabed temperature may be impacted. Also the heated pore fluids and their associated movements during convection, could lead to physical, geochemical and diagenetic reactions and changes within the surrounding sediments.

6.3 Future Research

6.3.1 2D Mixed Sediments Investigations

The presented 2D experiments only considered homogenous burial sediments for each set of experiment runs with varying cable surface temperatures. Thus, investigation are restricted to the thermal regimes around cables buried within homogeneous coarse silt sediments with low permeability, homogeneous fine sand sediments with medium permeability and homogeneous very coarse sand sediments with high permeability. It will be interesting to expand this research to investigate the surrounding burial thermal regime of mixed sediments and with particular interest of mixed natural sediments – mixed coarse silt, fine sand and very coarse sand.

Results from the current completed experiments and numerical models would permit a confident prediction, that the bulk permeability of the resultant sediment mixture will have strong influence on the heat flow mechanism depending on the space of cable temperature and permeability (see Figure 3.16). However, the resultant mixed natural sediment will have a wider grain size distribution (silt to very coarse sand) and very irregular grain shapes that will cause “dead end” and “bypassed” flow channels, which will eventually act as buffers to heated pore fluids movements, particularly during convection. This could affect the heat flow mechanism regardless of the mixed sediment bulk permeability and cable surface temperature.

6.3.2 3D Experiments and Simulations

The presented experiments and numerical models are based on 2D setups due to time, practicality and mainly financial constraints. Thus with industrial collaboration and partners, an ideal future research route of expanding on the already completed researches is to carry out detailed 3D experiments and 3D numerical modelling of the surrounding submarine HV cables environments.

However, the 3D experiments will require using an actual short section of submarine cable for better replication of cable *in situ* conditions rather than using analogue heat source. This will be a very big challenge to develop and instrument the experimental set-up with power source and data loggers. As it will require constructing a massive internal laboratory tank or alternatively an external open trench with dimension of about 100 m long, 5 m wide and 10 m deep as well as capable of holding large quantity of water above the buried cable section for simulating the power of the sea. A more sophisticated approach will also be required to instrument more than 2000 thermocouples for measuring the full 3D and out of plane heat generated along and around the actual cable length. It will take a longer time for each 3D experiment run to reach equilibrium heat flow state compared to the ~ 6 days that was required for the 2D experiments. There will also be the vital challenge of insulating the massive 3D experiment tank.

If the above-described challenges are resolved, this approach will be capable of providing detailed understanding of the complete 3D heat flow pattern around buried submarine HV cables. The 3D experiments will allow altering the setup to investigate different burial scenarios such as incorporating trench sections with varying sediment permeability, varying depth of cable burial and detailed mixed sediments experiments. The 3D experiment set-up will also permit investigation of the various thermal implications of buried submarine HV cables, such as: the convection cooling effect on internal cable conductors, current ratings, ampacity and cable insulation degradation rates. Investigate the impact on sediments grain movements (macroscopic or microscopic), biological and geochemical changes of the surrounding burial sediments.

Page intentionally left blank.

Appendix

Figure A1: 2D experimental tank (height: 2.5 m, width: 2.0 m and thickness: 0.11 m) with an inserted heat source (Figure A2), designed as a proxy to a buried sub-seafloor HV cable. The tank is constructed from 2 cm thick Perspex, reinforced with steel bars. The vicat softening temperature, coefficient of thermal expansion and thermal conductivity of the Perspex are 110 ^oC, $7x10^{-5}$ K^{-1}, and 0.2 Wm^{-1} K^{-1}, respectively. The tank is open at the top and has integrated outlets at the base to allow in-fill and removal of sediments and water. Three layers of 10 cm thick Celotex™ TA4000 insulation sheets with thermal conductivity of 0.022 Wm^{-1} K^{-1} each and low emissivity aluminium foil facings on both sides, providing high performance insulation and are directly attached to the external sides of the tank to limit heat loss through the Perspex sides.

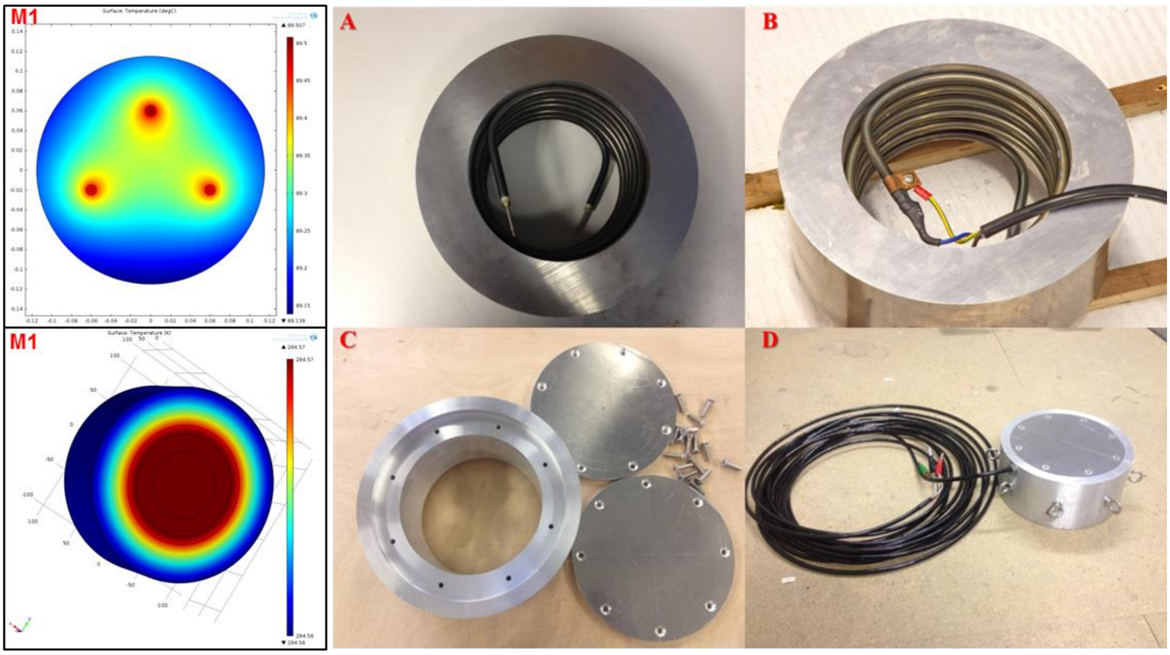

Figure A2: Uniquely built big tank heat source construction phases and modelling. A to D shows the stages involved in the actual heat source construction. This involved coiling a heating rod inside a drilled out cavity at the middle of the aluminium heating block (A), initial testing (B), heat source side covering construction to prevent water ingress and final testing after assembling all the heat source components together. Initial modelling results using three small cartriges approach (M1) and the constructed heat source (M2). The heat source was constructed using an INC800 heating element (Length: 2.44m and Loading Watt: 2000) that is tightly coiled inside a drilled cavity in the middle of a cylindrical aluminium block (radius: 0.11 m and thickness: 0.10 m), providing a good thermal contact.

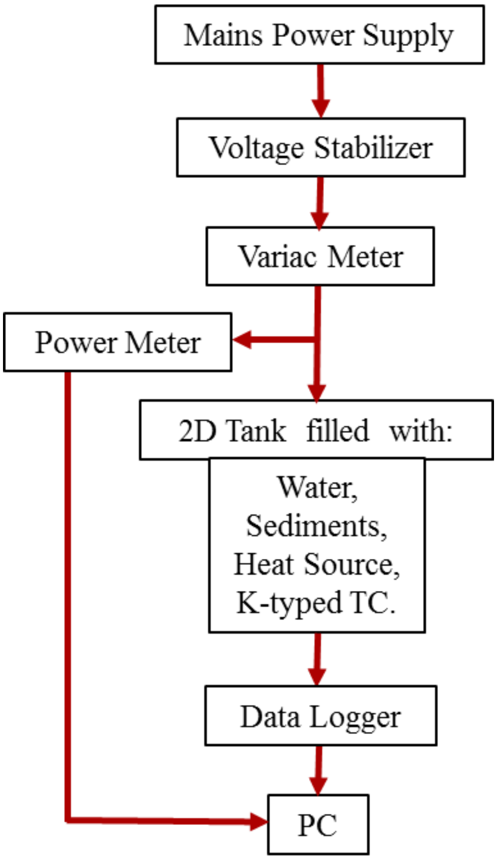

Figure A3: Flow chart of the developed 2D lab experiment procedure and equipment set-up.

Table A1: Statistical formulae used in the calculation of grain size parameters, and suggested descriptive terminology. f is the frequency in percent; m is the mid-point of each class interval in metric (m_m) or phi $(m_\emptyset)$ units; P_x and $\emptyset_x$ are grain diameters, in metric or phi units respectively, at the cumulative percentile value of x.

(a) Arithmetic Method of Moments

Mean	Standard Deviation	Skewness	Kurtosis
$\bar{x}_a = \frac{\Sigma f m_m}{100}$	$\sigma_a = \sqrt{\frac{\Sigma f(m_m - \bar{x}_a)^2}{100}}$	$Sk_a = \frac{\Sigma f(m_m - \bar{x}_a)^3}{100\sigma_a{}^3}$	$K_a = \frac{\Sigma f(m_m - \bar{x}_a)^4}{100\sigma_a{}^4}$

(b) Geometric Method of Moments

Mean	Standard Deviation	Skewness	Kurtosis
$\bar{x}_g = \exp\frac{\Sigma f \ln m_m}{100}$	$\sigma_g = \exp\sqrt{\frac{\Sigma f(\ln m_m - \ln \bar{x}_g)^2}{100}}$	$Sk_g = \frac{\Sigma f(\ln m_m - \ln \bar{x}_g)^3}{100 \ln \sigma_g{}^3}$	$K_g = \frac{\Sigma f(\ln m_m - \ln \bar{x}_g)^4}{100 \ln \sigma_g{}^4}$

Sorting (σ_g)		Skewness (Sk_g)		Kurtosis (K_g)	
Very well sorted	< 1.27	Very fine skewed	< $^-$1.30	Very platykurtic	< 1.70
Well sorted	1.27 – 1.41	Fine skewed	$^-$1.30 – $^-$0.43	Platykurtic	1.70 – 2.55
Moderately well sorted	1.41 – 1.62	Symmetrical	$^-$0.43 – $^+$0.43	Mesokurtic	2.55 – 3.70
Moderately sorted	1.62 – 2.00	Coarse skewed	$^+$0.43 – $^+$1.30	Leptokurtic	3.70 – 7.40
Poorly sorted	2.00 – 4.00	Very coarse skewed	> $^+$1.30	Very leptokurtic	> 7.40
Very poorly sorted	4.00 – 16.00				
Extremely poorly sorted	> 16.00				

(c) Logarithmic Method of Moments

Mean	Standard Deviation	Skewness	Kurtosis
$\bar{x}_\phi = \frac{\Sigma f m_\phi}{100}$	$\sigma_\phi = \sqrt{\frac{\Sigma f(m_\phi - \bar{x}_\phi)^2}{100}}$	$Sk_\phi = \frac{\Sigma f(m_\phi - \bar{x}_\phi)^3}{100\sigma_\phi{}^3}$	$K_\phi = \frac{\Sigma f(m_\phi - \bar{x}_\phi)^4}{100\sigma_\phi{}^4}$

Sorting (σ_ϕ)		Skewness (Sk_ϕ)		Kurtosis (K_ϕ)	
Very well sorted	< 0.35	Very fine skewed	> $^+$1.30	Very platykurtic	< 1.70
Well sorted	0.35 – 0.50	Fine skewed	$^+$0.43 – $^+$1.30	Platykurtic	1.70 – 2.55
Moderately well sorted	0.50 – 0.70	Symmetrical	$^-$0.43 – $^+$0.43	Mesokurtic	2.55 – 3.70
Moderately sorted	0.70 – 1.00	Coarse skewed	$^-$0.43 – $^-$1.30	Leptokurtic	3.70 – 7.40
Poorly sorted	1.00 – 2.00	Very coarse skewed	< $^-$1.30	Very leptokurtic	> 7.40
Very poorly sorted	2.00 – 4.00				
Extremely poorly sorted	> 4.00				

Table A2: Size scale adopted in the GRADISTAT program, modified from Udden (1914) and Wentworth (1922).

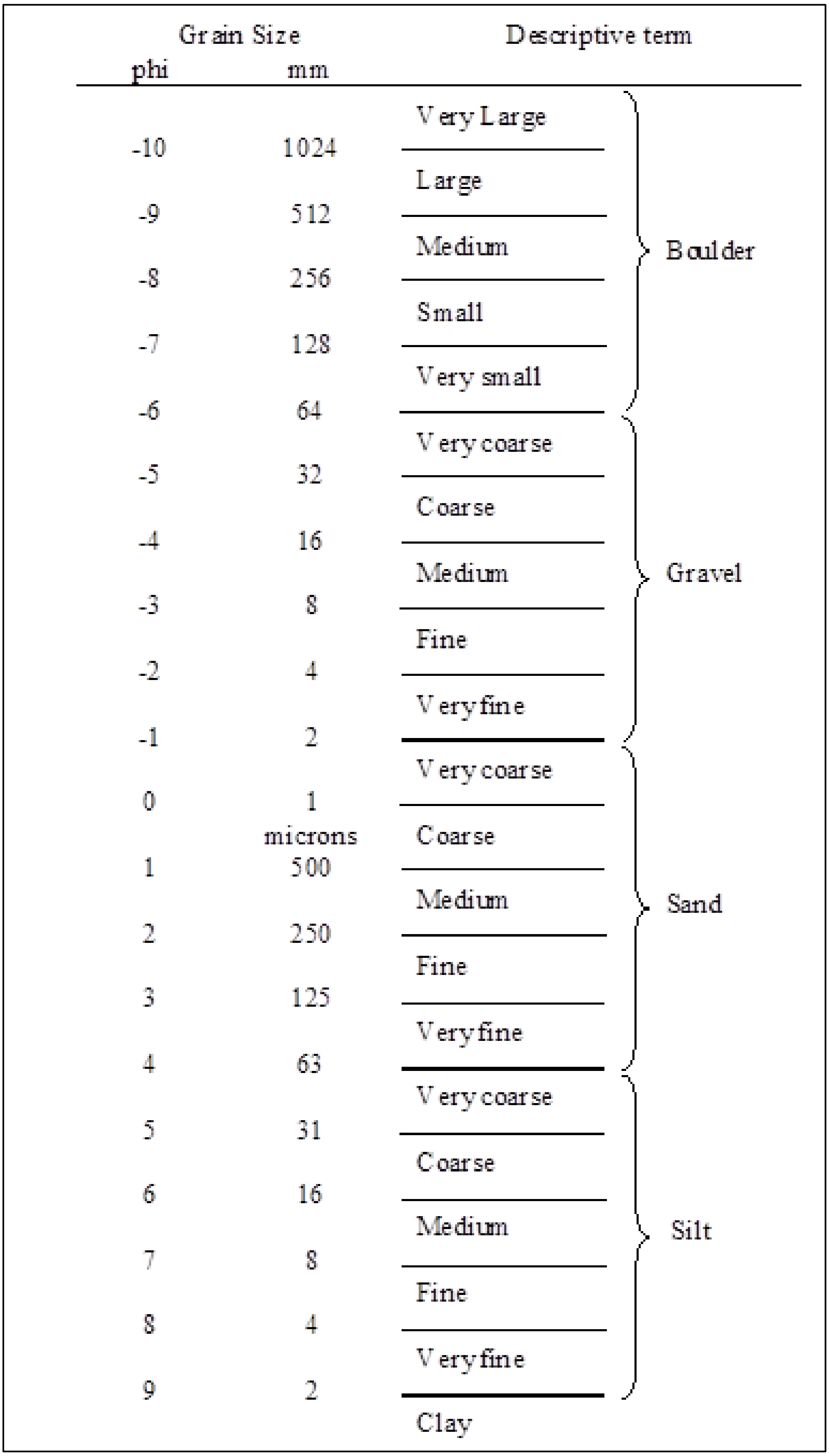

Grain Size		Descriptive term	
phi	mm		
		Very Large	Boulder
-10	1024		
		Large	
-9	512		
		Medium	
-8	256		
		Small	
-7	128		
		Very small	
-6	64		
		Very coarse	Gravel
-5	32		
		Coarse	
-4	16		
		Medium	
-3	8		
		Fine	
-2	4		
		Very fine	
-1	2		
		Very coarse	Sand
0	1		
		Coarse	
1	microns 500		
		Medium	
2	250		
		Fine	
3	125		
		Very fine	
4	63		
		Very coarse	Silt
5	31		
		Coarse	
6	16		
		Medium	
7	8		
		Fine	
8	4		
		Very fine	
9	2		
		Clay	

Page intentionally left blank.

List of References

Aberg, B., 1992. Hydraulic conductivity of noncohesive soils, *J. Geotech. Eng.,* 118**,** 1335-1347.

Abu-Hamdeh, N.H., 2003. Thermal properties of soils as affected by density and water content, *Biosyst Eng,* 86**,** 97-102.

Adams, J.A. & Rogers, D.F., 1973. Computer-Aided Heat Transfer Analysis, *McGraw-Hill, New York*.

Amyx, J.W., Bass, D.M. & Whiting, R.L., 1960. Petroleum Reservoir Engineering: Physical properties, *McGraw-Hill, New York***,** 610.

Anders, G.J., 1997. Rating of Electric Power Cables – Ampacity Calculations for Transmission, Distribution and Industrial Applications, *IEEE Press, New York*.

Anders, G.J., Napieralski, A.K.T. & Zamojski, W., 1998. Calculation of the internal thermal resistance and ampacity of 3-core unscreened cables with fillers, *IEEE Trans. Power Del.,* 13**,** 699-705.

Anger, K., et al., 2003. Larval and early juvenile development of Paralomis granulosa reared at different temperatures: Tolerance of cold and food limitation in a lithodid crab from high latitudes, *Mar. Ecol. Prog. Ser.,* 253**,** 243-251.

Arpaci, V.S., 1966. Conduction Heat Transfer, *Addison-Wesley, Reading, M A.*

Barnes, D.K.A. & Peck, L.S., 2008. Vulnerability of Antarctic shelf biodiversity to predicted regional warming, *Clim. Res.,* 37**,** 149-163.

Bear, J., 1972. Dynamics of Fluids in Porous Media, *Elsevier, New York***,** 166.

Bear, J., 1988. Dynamics of fluids in porous media., *Dover publications*.

Beck, A., 1957. A steady state method for the rapid measurement of the thermal conductivity of rocks, *Journal of scientific instruments,* 34**,** 186-189.

Beck, A.E., 1976. An improved method of computing the thermal conductivity of fluid-filled sedimentary rocks, *Geophysics,* 41**,** 133-144.

Becker, K., VonHerzen, R., Kirklin, J., Evans, R., Kadko, D., Kinoshita, M., Matsubayashi, O., Mills, R., Schultz, A. & Rona, P., 1996. Conductive heat flow at the TAG active hydrothermal mound: Results from 1993-1995 submersible surveys, *Geophys Res Lett,* 23**,** 3463-3466.

Berg, C.F., 2014. Permeability Description by Characteristic Length, Tortuosity, Constriction and Porosity, *Transport in Porous Media,* 103.

Blair, S.C., Berge, P.A. & Berryman, J.G., 1996. Using two-point correlation functions to characterize microgeometry and estimate permeabilities of sandstones and porous glass, *J. Geophys. Res.,* 101**,** 20,359-320,375.

Blott, S.J. & Pye, K., 2001. GRADISTAT: A grain size distribution and statistics package for the analysis of unconsolidated sediments, *Earth Surf Proc Land,* 26**,** 1237-1248.

Boehler, R., 1996. Melting temperature of the Earth's mantle and core: Earth's thermal structure, *Annual Review of Earth and Planetary Sciences,* 24(1)**,** 15-40.

Bristow, K.L., 1998. Measurement of thermal properties and water content of unsaturated sandy soil using dual-probe heat-pulse probes, *Agr Forest Meteorol,* 89**,** 75-84.

BS-IEC-60287-1-1:2014, 2014. Electric Cables - Calculation of the Current Rating - Amendment 1, *Electrotechnical Comittee: British Standards Board*.

BSH, 2014. Standard Ground Investigation for Offshore Wind Energy, *Federal Maritime and Hydrographic Agency (BSH), Hamburg and Rostock*.

Campbell, G.S., 1985. *Soil Physics With BASIC-Transport Models for Soil-Plant Systems,* edn, Vol., pp. Pages, Elsevier, New York.

Campbell, G.S. & Norman, J.M., 1998. *An Introduction to Environmental Biophysics,* edn, Vol., pp. Pages, Springer, New York.

Carman, P.C., 1937. Fluid flow through granular beds, *Transactions-Institution of Chemical Engineers,* 15**,** 150-166.

Carman, P.C., 1938. The determination of the specific surface of powders, *J. Soc. Chem. Ind. Trans.,* 57**,** 225.

Carman, P.C., 1956. Flow of gases through porous media., *Butterworth's Publications, London.*

Carrier, W., III, 2003. Goodbye, Hazen; Hello, Kozeny-Carman, *Journal of Geotechnical and Geoenvironmental Engineering* 129**,** 1054-1056.

Carrier, W.D. & Beckman, J.F., 1984. Correlations between index tests and the properties of remolded clays, *Geotechnique,* 34**,** 211-228.

Carrier, W.D., Olhoeft, G.R. & Mendell, W., 1991. Physical properties of the lunar surface. *in Lunar sourcebook*, pp. 475-594, eds. Heiken, G., Vaniman, D. & French, B. M. Cambridge University Press, Cambridge, England.

Carslaw, H.S. & Jaeger, J.C., 1959. Conduction of Heat in Solids, *Oxford University Press, London*.

Carson, J.E., 1963. Analysis of soil and air temperature by Fourier techniques, *Journal of Geophysical Research,* 68**,** 2217-2232.

Celotex, 2013. Celotex TA4000, Celotex Limited, Available from: http://www.celotex.co.uk/products/ta4000 (Accessed 30 September 2015).

Chekhonin, E., Parshin, A., Pissarenko, D., Popov, Y., Romushkevich, R., Safonov, S., Spasennykh, M., Chertenkov, M.V. & Stenin, V.P., 2012. When rocks get hot: Thermal properties of reservoir rocks, *Oilfield review,* 24**,** 20-37.

Cho, Y.K., Kim, T.W., You, K.W., Park, L.H., Moon, H.T., Lee, S.H. & Youn, Y.H., 2005. Temporal and spatial variabilities in the sediment temperature on the Baeksu tidal flat, Korea, *Estuarine Coastal and Shelf Science,* 65**,** 302-308.

Christie, C.H. & Nagihara, S., 2016. Geothermal gradients of the northern continental shelf of the Gulf of Mexico, *Geosphere,* 12**,** 26-34.

Cornish-Lime, 2011. CLS33 Superfine High Silica SandCornish Lime Company Limited, Available from: http://cornishlime.co.uk/cls33-superfine-pale-pink-high-silica-sand (Accessed 30 September 2015)

Darcy, H., 1856. D`etermination des lois d'`ecoulement de l'eau `a travers le sable.

de-Leon, F. & Anders, G.J., 2008. Effects of Backfilling on Cable Ampacity Analyzed With the Finite Element Method, *IEEE Transmission Power Deliver,* 23**,** 537-543.

de Leon, F. & Anders, G.J., 2008. Effects of backfilling on cable ampacity analyzed with the finite element method, *IEEE Trans. Power Del.,* 23**,** 537-543.

Dullien, F.A.L., 1992. Porous Media: Fluid Transport and Pore Structure (2nd ed), *Academic Press, San Diego***,** 574.

Emeana, C.J., Hughes, T.J., Dix, J.K., Gernon, T.M., Henstock, T.J., Thompson, C.E.L. & Pilgrim, J.A., 2016. The thermal regime around buried submarine high voltage cables, *Geophysical Journal International,* 206**,** 1051 - 1064.

EWEA, 2013. Deep Water: The next step for offshore wind energy, *The European Wind Energy Association (EWEA), Brussels*.

Fair, G.M. & Hatch, L.P., 1933. Fundamental factors governing the stream-line flow of water through sand, *J. Am. Water Works Assoc.,* 25**,** 1551-1565.

Folk, R.L. & Ward, W.C., 1957. Brazos River Bar: A study in the significance of grain size parameters, *J Sediment Petrol,* 27**,** 3-26.

Frederich, M., et al., 2001. Distribution patterns of decapod crustaceans in polar areas: A result of magnesium regulation, *Polar Biol.,* 24**,** 719-723.

Gaston, K.J., 2003. The Structure and Dynamics of Geographic Ranges, *Oxford Univ. Press, Oxford, U. K***,** 266.

Gebhart, B., 1979. Buoyancy-Induced Fluid Motions Characteristic of Applications in Technology, *J. Fluids Eng.,* 101.

Geohil, A.G., 2013. Geothermal energy, *Available from: http://www.mpoweruk.com/geothermal_energy.htm (Accessed 30 September 2015).*

Gernon, T.M., Gilbertson, M.A., Sparks, R.S.J. & Field, M., 2008. Gas fluidisation in an experimental tapered bed: Insights into processes in diverging volcanic conduits., *Journal of Volcanology and Geothermal Research,* 174(1-3)**,** 49-56.

Goto, S. & Matsubayashi, O., 2008. Inversion of needle-probe data for sediment thermal properties of the eastern flank of the Juan de Fuca Ridge, *Journal of Geophysical Research-Solid Earth,* 113.

Goto, S. & Matsubayashi, O., 2009. Relations between the thermal properties and porosity of sediments in the eastern flank of the Juan de Fuca Ridge, *Earth Planets Space,* 61**,** 863-870.

Goto, S., Mizoguchi, T., Kimura, R., Kinoshita, M., Yamano, M. & Hamamoto, H., 2012. Variations in the thermal conductivities of surface sediments in the Nankai subduction zone off Tokai, central Japan, *Marine Geophysical Research,* 33**,** 269-283.

Greenland, D.E., 1969. Soil heat flow investigations at Cass, South Island high country, *New Zeal J Agr Res,* 12**,** 353-366.

Harris, R.N., Grevemeyer, I., Ranero, C.R., Villinger, H., Barckhausen, U., Henke, T., Mueller, C. & Neben, S., 2010. Thermal regime of the Costa Rican convergent margin: 1. Along-strike variations in heat flow from probe measurements and estimated from bottom-simulating reflectors, *Geochemistry Geophysics Geosystems,* 11.

Harrison, S.J., 1985. Heat exchanges in muddy intertidal sediments - Chichester Harbor, West Sussex, England, *Estuarine Coastal and Shelf Science,* 20.

Harrison, S.J. & Morrison, P., 1993. Temperatures in a Sandy Beach under Strong Solar Heating - Patara Beach, Turkey, *Estuarine Coastal and Shelf Science,* 37**,** 89-97.

Harrison, S.J. & Phizacklea, A.P., 1985. Seasonal-Changes in Heat-Flux and Heat-Storage in the Intertidal Mudflats of the Forth Estuary, Scotland, *J Climatol,* 5**,** 473-485.

Harrison, S.J. & Phizacklea, A.P., 1987a. Temperature-fluctuation in muddy intertidal sediments, Forth Estuary, Scotland, *Estuarine Coastal and Shelf Science,* 24.

Harrison, S.J. & Phizacklea, A.P., 1987b. Vertical temperature-gradients in muddy intertidal sediments in the Forth Estuary, Scotland, *Limnology and Oceanography,* 32.

Hartmann, A. & Villinger, H., 2002. Inversion of marine heat flow measurements by expansion of the temperature decay function, *Geophysical Journal International,* 148**,** 628-636.

Hazen, A., 1892. Some Physical Properties of Sands and Gravels, with Special Reference to their Use in Filtration, *24th Annual Report, Massachusetts State Board of Health, Boston.,* Pub.Doc. No.34, 539-556.

Hiscock, K., Southward, A., Tittley, I. & Hawkins, S., 2004. Effect of changing temperature on benthic marine life in Britain and Ireland, *Aquatic Conservation: Marine and Freshwater Ecosystems,* 14**,** 333-362.

Holt, R.D., 1990. The microevolutionary consequences of climate change, *Trends Ecol. Evol. ,* 5**,** 311-315.

Horton, R., Wierenga, P.J. & Nielsen, D.R., 1983. Evaluation of Methods for Determining the Apparent Thermal-Diffusivity of Soil near the Surface, *Soil Science Society of America Journal,* 47**,** 25-32.

Hosier, I.L., Reaud, S., Vaughan, A.S. & Swingler, S.G., 2008. Morphology, thermal, mechanical and electrical properties of propylene-based materials for cable applications, *In Proceedings of the 2008 IEEE International Symposium on Electrical Insulation, Vancouver, BC, June 2008***,** 502-505.

Hughes, T.J., Henstock, T.J., Pilgrim, J.A., Dix, J.K., Gernon, T.M. & Thompson, C.E.L., 2015. Effect of sediment properties on the thermal performance of submarine HV cables, *IEEE Transactions on Power Delivery,* 30**,** 2443-2450.

Hyndman, R.D., Davis, E.E. & Wright, J.A., 1979. Measurement of Marine Geothermal Heat-Flow by a Multi-Penetration Probe with Digital Acoustic Telemetry and Insitu Thermal-Conductivity, *Mar Geophys Res,* 4**,** 181-205.

Incropera, F.P. & Dewitt, D.P., 1985. Introduction to Heat Transfer, *John Wiley and Sons, New York*.

Jackson, D.R. & Richardson, M.D., 2001. Seasonal temperature gradients within a sandy seafloor: Implications for acoustic propagation and scattering, *Proc. Inst. Acoust. Acoust. Oceanogr.,* 23**,** 361-368.

Jackson, D.R. & Richardson, M.D., 2002. Seasonal temperature gradients within a sandy seafloor: Implications for acoustic propagation and scattering, *IEEE J. Oceanic Eng.,* 27**,** 546-560.

Jackson, D.R. & Richardson, M.D., 2007. High-Frequency Seafloor Acoustics, Underwater Acoustics Series Monograph, *Springer, New York, USA*.

Jaeger, J.C., 1958. The measurement of thermal conductivity with cylindrical probes, *EOS Transactions American Geophysical Union,* 39**,** 708-710.

Jaluria, Y., 1980. Natural Convection Heat and Mass Transfer, *Pergamon Press, New York*.

Karahan, M. & Kalenderli, O., 2011. Coupled Electrical and Thermal Analysis of Power Cables Using Finite Element Method. *in Heat Transfer - Engineering Applications*, ed. Prof Vyacheslav Vikhrenko, I. InTech, Available from: http://www.intechopen.com/books/heat-transferengineeringapplications/coupled-electrical-and-thermal-analysis-of-power-cables-using-finite-element-method.

Kim, T.W., Cho, Y.K. & Dever, E.P., 2007. An evaluation of the thermal properties and albedo of a macrotidal flat, *Journal of Geophysical Research-Oceans,* 112.

Kovac, N., Sarajcev, I. & Poljak, D., 2006. Nonlinear-Coupled Electric-Thermal Modeling of Underground Cable Systems, *IEEE Transactions on Power Delivery,* 21**,** 4-14.

Kozeny, J., 1927. Uber Kapillare Leitung Des Wassers in Boden., *Sitzungsber Akad. Wiss.Wien Math.Naturwiss.Kl.,* 136 (2a)**,** 271-306.

Kuffel, E. & Zaengl, W.S., 2004. High Voltage Engineering, *Pergamon Press, Oxford*.

Lambe, T.W., 1965. Soil testing for engineers, *Wiley, New York.*

Lister, C.R.B., 1979. Pulse-Probe Method of Conductivity Measurement, *Geophys J Roy Astr S,* 57**,** 451-461.

Loudon, A.G., 1952. The computation of permeability from simple soil tests., *Geotechnique,* 3**,** 165-183.

Lovell, M.A., 1985a. Thermal-conductivities of marine-sediments, *Quarterly Journal of Engineering Geology, London,* 18**,** 437-441.

Lovell, M.A., 1985b. Thermal conductivity and permeability assessment by electrical resistivity measurements in marine-sediments, *Marine Geotechnology,* 6**,** 205-240.

Malik, N.H., Al-Arainy, A.A. & Qureshi, M.I., 1998. Electrical Insulation in Power Systems, *Marcel Dekker Inc., New York*.

Meissner, K., Bockhold, J. & Sordyl, H., 2007. Problem of cables heat **-** Presentation of results from Field measurements of the seabed temperature in the range of the electric cables in Danish Offshore wind farm, Nysted Wind Farm (Denmark). *in Marine Environment Symposium*, pp. 153-161, Hamburg.

Mole, P., Featherstone, J. & Winter, S., 1997. Cable Protection – Solutions Through New Installation and Burial Approaches, *Proceedings SubOptic 1997, San Francisco,* Available from: Submarine Cable Improvement Group. http://www.scig.net/ (Accessed 30 September 2015)**,** 750-757.

Motori, A., Sandrolini, F. & Montanari, G.C., 1991. A contribution to the study of ageing of XLPE insulated cables, *IEEE Trans. Power Del.,* 6**,** 34-42.

Myers, G.E., 1971. Analytical Methods in Conduction Heat Transfer, *McGraw-Hill, New York*.

Nagihara, S. & Smith, M.A., 2005. Geothermal gradient and temperature of hydrogen sulfide-bearing reservoirs, Alabama continental shelf, *Aapg Bull,* 89**,** 1451-1458.

Nexans, 2004. 60-500kV High Voltage Underground Power Cables: XLPE Insulated Cables, *Paris*.

Ochsner, T.E., Horton, R. & Ren, T.H., 2001. A new perspective on soil thermal properties, *Soil Science Society of America Journal,* 65**,** 1641-1647.

OSPAR, 2009b. Assessment of the Environmental Impacts of Cables, *Biodiversity Series***,** 19.

Ozisik, M.N., 1980. Heat Conduction, *Wiley, New York.*

Pacheco, C.R., Oliveira, J.C. & Vilaca, A.L.A., 2000. Power quality impact on thermal behaviour and life expectancy of insulated cables, *IEEE Ninth International Conference on Harmonics and Quality of Power, Proceedings, Orlando, FL,* 3**,** 893-898.

Parmesan, C., 2006. Ecological and evolutionary responses to recent climate change, *Annu. Rev. Ecol. Syst.,* 37**,** 637-669.

Parmesan, C. & Yohe, G., 2003. A globally coherent fingerprint of climate change impacts across natural systems, *Nature,* 421**,** 37-42.

Pearse, J.S., et al., 1991. Reproduction of Antarctic benthic marine invertebrates: Tempos, modes and timing, *Am. Zool.,* 31**,** 65-80.

Peck, L.S., 2002. Ecophysiology of Antarctic marine ectotherms: Limits to life, *Polar Biol,* 25**,** 31-40.

Peck, L.S., et al., 2004. Extreme sensitivity of biological function to temperature in Antarctic marine species, *Funct. Ecol.,* 18**,** 625-630.

Peck, L.S., et al., 2006. Metabolism and development in pelagic larvae of Antarctic gastropods with mixed reproductive strategies, *Mar. Ecol. Prog. Ser,* 318**,** 213-220.

Piccolo, M.C., Perillo, G.M.E. & Daborn, G.R., 1993. Soil-temperature variations on a tidal flat in Minas Basin, Bay of Fundy, Canada, *Estuarine Coastal and Shelf Science,* 36.

Pilgrim, J.A., 2011. Circuit Rating Methods for High Temperature Cables, PhD, University of Southampton.

Pomeroy, L.R. & Deibel, D., 1986. Temperature regulation of bacterial activity during the spring bloom in Newfoundland coastal waters, *Science,* 233**,** 359-361.

Potters-Ballotini, 2011. Features of Glass Beads, Potters-Ballotini Limited, Available from: http://www.pqj.co.jp/en/product/01.html (Accessed 30 September 2015)

Powers, M.C., 1953. A new roundness scale for sedimentary particles, *J Sediment Petrol,* 23**,** 117-119.

Pribnow, D.F.C. & Sass, J.H., 1995. Determination of Thermal-Conductivity for Deep Boreholes, *Journal of Geophysical Research-Solid Earth,* 100**,** 9981-9994.

Price, J.H., Tittley, I. & Richardson, W.D., 1979. The distribution of Padina pavonica. (L.) Lamour. (Phaeophyta: Dictyotales) on British and adjacent European shores., *Bulletin of the British Museum Natural History Botany,* 7**,** 1-67.

Quetin, L.B., et al., 1994. Krill energetics: Seasonal and environmental aspects of the physiology of Euphausia superba. *in Southern Ocean Ecology: The BIOMASS Perspective*, pp. 165-184, ed. El-Sayed, S. Z. Cambridge Univ. Press, Cambridge, U. K.

Quiblier, J.A., 1984. A new three-dimensional modeling technique for studying porous media, *J. Colloid Interface Sci.,* 98**,** 84-102.

Railing, B.D., Miller, J.J., Steckley, P., Moreau, G., Bard, P., Ronström, L. & Lindberg, J., 2004. Cross sound cable project—second generation VSC technology for HVDC. *in Cigré conference*, Paris, France.

Rajan, S.D. & Frisk, G.V., 1992. Seasonal-variations of the sediment compressional wave-speed profile in the Gulf of Mexico, *Journal of the Acoustical Society of America,* 91**,** 127-135.

Ratcliffe, E.H., 1960. The thermal conductivity of ocean sediments, *J. Geophys. Res.,* 65**,** 1535-1541.

Robinson, G., 1990. Ageing characteristics of paper-insulated power cables, *Power Engineering Journal,* 4**,** 95-100.

Rodriguez, J.M., Edeskär, T. & Knutsson, S., 2013. Particle shape quantities and measurement Techniques–A review, *Electronic Journal of Geotechnical Engineering* 18**,** 169-198.

Scheidegger, A.E., 1974. The physics of flow through porous media, *University of Toronto Press, Toronto*.

Simmons, M., 2001. High Voltage Cables, *in High Voltage Engineering and Testing, edited by Ryan, H. M., IET, London, 2nd Ed.,* .

Sivanagaraju, S. & Satyanarayana, S., 2009. Electrical Power Transmission and Distribution, *Dorling Kindersley, Delhi*.

Southward, A.J. & Southward, E.C., 1988. Disappearance of the warm-water hermit crab Clibanarius erythropus from south-west Britain, *Journal of the Marine Biological Association of the United Kingdom,* 69**,** 409-412.

SP-Transmission & NationalGrid, 2011. Western HVDC Link: Preparing our energy network for the future, *Environmental Report: Marine Cable Route*.

Swaffield, D.J., Lewin, P.L. & Sutton, S.J., 2008. Methods for rating directly buried high voltage cable circuits, *IET Gener. Transm. Distrib.,* 2**,** 393-401.

Tedas, 2005. Assembly (application) principles and guidelines for power cables in the electrical power distribution networks, *Turkish Electrical Power Distribution Inc.*

Terzaghi, K. & Peck, R.B., 1964. Soil Mechanics in Engineering Practice, *Wiley, New York.*

Terzaghi, K., Peck, R.B. & Mesri, G., 1996. Soil mechanics in engineering practice, *Wiley, New York.*

Thomson, J., 2010. Observations of thermal diffusivity and a relation to the porosity of tidal flat sediments, *Journal of Geophysical Research-Oceans,* 115.

Thue, W.A., 1999. Electrical Power Cable Engineering, *CRC Press, New York*.

Todd, D.K., 1959. Ground water hydrology, *Wiley, New York.*

Turcotte, D.L. & Schubert, G., 2002. Geodynamics, *Cambridge University Press, Cambridge UK*.

UK House of Commons: Energy and Climate Change Committee, 2011. A European Supergrid, *The stationery office limited, London,* 1.

Van Brakel, J., 1975. Pore space models for transport phenomena in porous media review and evaluation with special emphasis on capillary liquid transport, *Powder Technology,* 11**,** 205-236.

van Landeghem, K.J.J., Baas, J.H., Mitchell, N.C., Wilcockson, D. & Wheeler, A.J., 2014. Reversed sediment wave migration in the irish sea, nw europe: A reappraisal of the validaty of geometry-based predictive modelling and assumptions, *Mar Geol,* 295-298**,** 95-112.

Von Herzen, R.P. & Maxwell, A.E., 1959. The measurement of thermal conductivity of deep sea sediments by a needle probe method, *J. Geophys. Res.,* 64**,** 1557-1563.

Vugts, H.F. & Zimmerman, J.T.F., 1985. The Heat-Balance of a Tidal Flat Area, *Netherlands Journal of Sea Research,* 19**,** 1-14.

Waite, W.F., Gilbert, L.Y., Winters, W.J. & Mason, D.H., 2006. Estimating thermal diffusivity and specific heat from needle probe thermal conductivity data, *Rev Sci Instrum,* 77**,** 1-5.

Wentworth, C.K., 1922. A scale of grade and class terms for clastic sediments., *Journal of Geology,* 30**,** 377-392.

Wheatcroft, R.A., Johnson, R.V. & Stevens, A.W., 2007. In situ time-series measurements of sub-seafloor sediment properties, *IEEE J. Oceanic Eng.,* 32**,** 862-871.

Woodside, W. & Messmer, J.H., 1961a. Thermal conductivity of porous media. I. Unconsolidated sands, *J Appl Phys,* 32**,** 1688-1699.

Woodside, W. & Messmer, J.H., 1961b. Thermal conductivity of porous media. II. Consolidated rocks, *J Appl Phys,* 32**,** 1699-1706.

Woodside, W. & Messmer, J.H., 1961c. Thermal conductivity of porous media: I. unconsolidated sands, II. Consolidated rocks, *J. Appl. Phys.,* 32**,** 1688-1706.

Worzyk, T., 2009. Submarine Power Cables: Design, Installation, Repair, Environmental Aspects, *Springer, Verlag Berlin*

Zimmerman, R.W., 1989. Thermal Conductivity of Fluid-Saturated Rocks, *J Petrol Sci Eng,* 3**,** 219-227.